FLUID FLOW, PARTICLE MOTION AND MIXING IN LADLE METALLURGY OPERATIONS

by

Dipak Mazumdar

A thesis submitted to the Faculty of Graduate Studies and Research in partial fulfillment of the requirements for the Degree of Doctor of Philosophy

Department of Mining and Metallurgical Engineering
McGill University
Montreal, Canada

ABSTRACT

Extensive computer predictions have been carried out by the author to study flow, addition dispersion and particle motion during central gas injection into cylindrical vessels. In conjunction with numerical computations, experiments were conducted in a 0.30 scale water model of a 150 ton steel processing ladle, using a Froude number scaling criterion. Two typical gas injection configurations (i.e., conventional central injection and C.A.S. alloy addition procedure) were investigated.

Flow visualization studies were carried out using a suspended network of silken threads, mean velocity vectors and overall flow patterns were determined by video recording techniques, while mean velocity vectors and associated turbulence level were also measured with laser doppler velocimetry. These measurements show very reasonable agreement with equivalent numerical predictions.

To simulate the subsurface motion of additions, spherical wooden balls of various densities were dropped from typical heights, and their subsurface trajectories, immersion times, etc., recorded by means of a video recorder. Frame by frame analysis of the video tapes showed trends which are in good accord with computed trajectories.

Mixing times of simulated molten additions were measured by the conductivity measurement technique. These were compared

with predictions from an equivalent tracer dispersion model and excellent agreement achieved.

For industrial application, flow, particle motion, and mixing times in a 150 ton steel processing ladle have been predicted and their technological significance discussed.

RÉSUMÉ

Les prédictions numériques ont été faites par l'auteur afin d'étudier l'écoulement, la dispersion des additions et le mouvement des particules pendant l'injection centrale d'un gaz dans des récipients cylindriques. Parallèlement aux calculs numériques, des essais expérimentaux ont été entrepris sur un modèle à l'échelle 0.30 pour une poche qui peut traiter 150 tonnes d'acier, tout en utilisant un numéro de Froude comme critère d'échelle. Deux configurations typiques pour l'injection de gaz (l'injection centrale conventionnelle et la procédure d'addition d'alliages C.A.S.) ont été examinées.

Les études pour visualiser l'écoulement ont été conduites en utilisant un réseau de fils de soie. Les vecteurs de vélocités moyennes et les lignes d'écoulement ont été déterminés tout en utilisant les techniques d'enregistrement par vidéo. Les vecteurs de vélocités moyennes et les niveaux de turbulence associés ont été mesurés aussi à l'aide d'un laser (vélocimétrie doppler). Ces mesures sont en bon accord avec les prédictions numériques.

Pour simuler le mouvement des additions sous la surface, des boules de bois sphériques avec des densités variables ont été lachées à des hauteurs typiques, pendant que leurs trajectoires, temps d'immersion, etc. étaient enregistrés avec le système vidéo. Les analyses des enregistrements ont montré

des résultats qui sont encore en bon accord avec les prédictions numériques.

Les temps requis pour obtenir le mélange complet de certaines additions liquides (fondus) ont été déterminés par une mesure de conductibilité. Un accord excellent a été obtenu lorsque ces résultats étaient comparés aux prédictions numériques d'un modèle de dispersion équivalent.

Pour les applications industrielles, l'écoulement, le mouvement des particules et les temps requis pour obtenir un mélange homogène dans une poche qui peut traiter 150 tonnes d'acier ont été prédits et leurs significations technologiques ont été discutées.

ACKNOWLEDGEMENT

It is a pleasure to express a deep sense of gratitude and appreciation to Professor R.I.L. Guthrie for his supervision and assistance throughout the course of this investigation. Discussions with Professor B. Ravi Baliga, Dept. of Mechanical Engineering, McGill University, during the initial period of this investigation are also gratefully acknowledged.

I am extremely grateful to Mr. Frank Sebo, for the help rendered by him during the water-model experiments. A number of other colleagues and friends have also provided constant inspiration through their special interest in my work. In particular, I wish to thank Mr. David Holford and Mr. Ramanand Rao for their help during the preparation of this thesis.

I must take this opportunity to record my sincere thanks to Professor A. Ghosh of Indian Institute of Technology, Kanpur, for his active interest in my work and for his personal interest in me. Finally, my sincerest thanks are also due to Jeanne and Laura, who typed the manuscript very carefully.

In this undertaking, I owe the greatest debt to my parents. I wish to acknowledge the moral support and the untiring inspiration of my parents by dedicating this piece of work to them.

I cannot hope that this piece of work is now entirely free of errors and obscurities, but I am certain that it is a good

deal clearer and more accurate, than it could have been without all the generous assistance, I have been fortunate enough to receive.

McGill University
Montreal, Aug. 1985

DIPAK MAZUMDAR

....To my parents with love

TABLE OF CONTENTS

INTRODUCTION TO THESIS

In recent years there has been a growing interest in ladle metallurgy as a final finishing step in the steelmaking operation. There have been two major reasons for the development of ladle metallurgy. One of these is associated with the high cost of electric furnace operation, which made it attractive to use the latter solely as a melting unit and to carry out refining operations such as deoxidation, alloy addition, desulphurization and trim chemical adjustments to composition, in a vessel beyond the electric furnace.

The other impetus for ladle metallurgy has been produced by the more stringent requirements for the composition of steel, which could be attained most economically by a separate processing step following the melting or refining operation that has taken place in the primary steelmaking vessel.

As is well known, ferroalloys and/or aluminium additions are still generally added prior to or during furnace tapping operations into teeming ladles. Variable amounts of slag carryover etc., can play havoc with alloy recoveries and in turn induce unacceptable variability into the final product chemistry.

To disperse such additions homogeneously in the steel bath, to remove particulates, to control temperature and to eliminate temperature stratification, inert gas blowing, vacuum treatment and magnetic stirring,etc. have been conventionally

practised. Ladle refining by gas blowing has advantages in that its capital cost is low and it gives good working efficiency and thus has been more widely used as compared with other methods. However, such inert gas stirring techniques in ladles have certain drawbacks:

(i) by mixing in an upper slag phase with an upwelling plume of deoxidized steel, reoxidation of solutes can take place,

(ii) air oxidation of exposed liquid steel in the eye of the plume is possible, and

(iii) entrapment of alloying elements into the slag, particularly light metal additions is possible, if any attempts are made to adjust steel chemistry during such gas blowing operation.

Furthermore as mentioned previously, light metal additions introduced during furnace tapping often lead to irreproducible and erratic recovery rates. In order to achieve higher and more reproducible alloy recoveries, a superior method of alloy addition, known as the C.A.S. Process (composition adjustment by sealed argon bubbling), was introduced by Nippon Steel Corporation in 1976(1). (see Fig. 1).

The C.A.S. Process utilizes argon gas that is bubbled into the molten steel through a porous plug or a submerged lance. The rising gas liquid plume creates an opening in the slag cover through which a refractory lined cylinder is lowered into steel. After obtaining an inert, sealed from the slag atmosphere within the cylinder/receptacle, additions are made inside this slag free region. This technology was purchased by

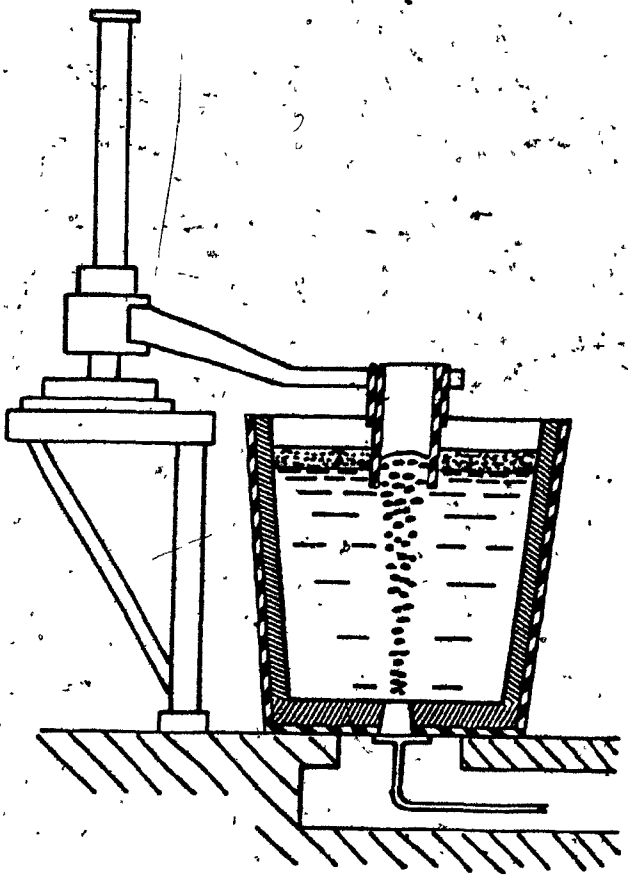

(a)

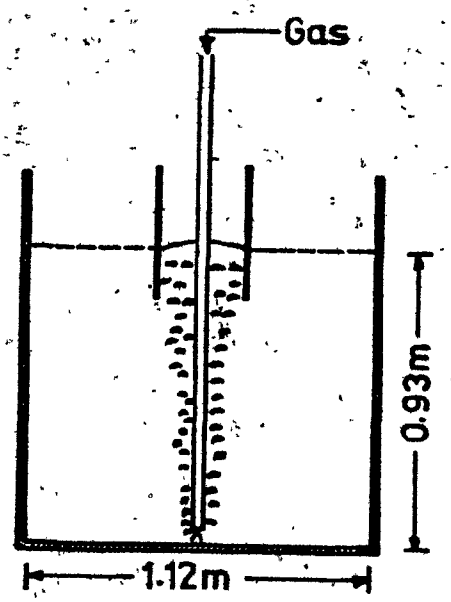

(b)

Figure 1(a) Schematic of C.A.S. operation as illustrated in ref. 1.

Figure 1(b) The present set-up for the simulation of C.A.S. method of alloy addition, showing the injection lance and the principal dimensions of the model.

U.S. Steel and is currently in use at the Gary Works (2).

In an attempt (2) to empirically optimize the C.A.S. process, extensive experimental trials on industrial sized steel processing ladles have been carried out at the Gary Works. Some of the observations made at Gary Works have been shown in Table 1. They reflect the following trends:

(i) aluminium variability in mold was decreased and aluminium usage per ton of steel decreased, when conventional procedures were replaced by the C.A.S. process and

(ii) processing time and argon consumption is higher for C.A.S. with regard to aluminium wire feeding operations.

Nevertheless, it is not clear why the seemingly small additional feature of a concentric cylinder, can exert such a profound influence on the dynamic nature of the addition making operation.

In order to develop a proper understanding about the dynamic nature of the C.A.S. process, and to evaluate its performance against conventional gas injection procedures, a fundamental investigation has been carried out by the author and is reported in the subsequent sections of this thesis.

The flow generated in cylindrical vessels during central injection was first analyzed. The role of grid spacing, turbulence model, and depth of lance submergence were all assessed. Following this, the effect of a surface baffle positioned above the eye of the plume was considered both theoretically and experimentally. These investigations have

Table 1

A. Aluminium recovery and aluminium usage (kg of Al/kg of steel) during conventional tapping addition and C.A.S. procedure (2)

	Conventional Tapping Addition	C.A.S. Procedure
Aluminium Recovery	16%	25%
Aluminium Usage (kg of Al/kg of steel)	2.318×10^{-3}	1.561×10^{-3}

B. Steel processing time and total argon usage (m^3) during aluminium wire feeding and C.A.S. procedure (2)

	C.A.S. (Total Deoxidation)	Al Feeder (Total Deoxidation)
Process Time (sec)	600	360
Argon usage (m^3)	1.472	0.3398

already been published(3-5). They appear in their entirety, along with some unpublished interpretations/calculations as part I of the thesis. The results obtained in part I formed the basis of the investigations reported in subsequent chapters.

Part II of the thesis deals with the subsurface motion of spherical additions in gas stirred systems. Part of this work has also been published(6). The presentation in chapter II is thus based on this publication as well as on some unpublished computations and interpretations.

In part III of the thesis, the mixing of molten additions in gas stirred systems has been investigated. Mathematical models of mixing have been developed and predictions from such models have been compared against measurements. The entire presentation in part III has already appeared in a publication(7).

Furthermore, each individual part of the thesis has been split into a number of subheadings namely, introduction, theory, experimental work, results and discussion, industrial applications and conclusions. The present format is intended to improve the readability of the thesis and conforms with the McGill University Guidelines Concerning Thesis Preparation, Section 7, which states that:

> " The Candidate has the option, subject to the approval of the Department, of including as part of the thesis the text of an original paper, or papers, suitable for submission to learned journals for publication. In this case the thesis must still conform to all other requirements explained in this document, and additional material (e.g. experimental data, details of equipment and experimental design)

may need to be provided. In any case abstract, full introduction and conclusion must be included, and where more than one manuscript appears, connecting texts and common abstract, introduction and conclusions are required. A mere collection of manuscripts is not acceptable; nor can reprints of published papers be accepted."

REFERENCES

1. K. Takashima, K. Arima, T. Shozi and H. Mori: "Method for Treatment of Molten Steel in a Ladle." U.S. Patent, No. 3971655, 1976.

2. C.L. Trout, D.L. Paterson and S.M. Hughes: AISE Conference Proceeding, Pittsburg, Pennsylvania, 1983.

3. D. Mazumdar and R.I.L. Guthrie: Metall. Trans., Vol. 16B, pp. 83-90, 1985.

4. D. Mazumdar and R.I.L. Guthrie: Ironmaking and Steelmaking, in press.

5. D. Mazumdar and R.I.L. Guthrie: Applied Mathematical Modelling, in press.

6. D. Mazumdar and R.I.L. Guthrie: Chemical Engineering Science, in press.

7. D. Mazumdar and R.I.L. Guthrie: Metall. Trans. B, in press.

PART I

HYDRODYNAMICS OF LADLE METALLURGY OPERATIONS

ABSTRACT

Experimental studies of flows generated in a 0.30 scale water model of a 150 ton ladle are reported. These were used to test the adequacy of a generalised two dimensional computational scheme for predicting flows generated by fully submerged and partially submerged gas injection lances. The roles of turbulence models and grid configurations were assessed. Furthermore, the presence of a surface baffle over the rising plume (i.e., the C.A.S. process) were considered and it was found that the placement of a baffle over rising plumes for slag free addition making, causes a strong, narrow, recirculatory vortex, with a complementary contrarotating vortex in the main bulk of the liquid.

Predictions for flows generated in a 150 ton steelworks ladle, with and without tapered sidewalls, and with and without surface baffles around the rising plume were also considered and their technological significance discussed.

INTRODUCTION

The chemical efficiencies of typical processing operations carried out in steelmaking ladles are intrinsically related to their hydrodynamic performance. Practically all ladle techniques presently used have one thing in common: most in one way or another employ gas, injected through a submerged lance, plug or nozzle, to stir the contents of the ladles. The gas rising as a plume to the free surface induces recirculatory flows of fluid within the vessel and thereby effects mixing, promotes chemical reactions, minimises temperature and composition inhomogeneities, and through the generation of turbulence, may aid inclusion agglomeration and float out.

In such ladle metallurgy operations, turbulent rather than laminar flows are more usual, since the size of the vessel employed, often precludes low Reynolds number flows. However, high temperature (1600^{o}C) and visual opacity of liquid metals make such processing units less than convenient case studies. A reasonable alternative for studying the characteristics of associated processing operations has been to use low temperature models in conjunction with mathematical models.

As the recirculatory flows typical of such processing operations are largely dominated by inertial rather than turbulent viscous forces, the turbulent quantities are often of secondary importance in determining general flow fields (1-3). Nevertheless, the prediction of correct velocity fields and

turbulent quantities become of real importance, if the ultimate objective of computational efforts are to predict associated heat and mass transfer phenomena, such as the times for alloy additions to melt and disperse and become well mixed within the vessel.

In recent years, a variety of recirculatory flows encountered in metallurgical processing operations have been modelled mathematically (1-21). The general approach adopted (1-19) has been to predict single phase flow fields through solution of the partial differential equations of continuity, motion and turbulence over the flow domain of interest, using relevant sets of boundary conditions. Predicted recirculatory flow fields for ladle flows have been found to be in reasonable agreement with those measured.

To quantify the motion, melting/dissolution and dispersion of alloy additives during such industrial operations, it is self evident that flow fields generated in such gas stirred systems must first be established. Although much information concerning conventional argon injection into cylindrical vessels is available in literature, no hydrodynamic information on the C.A.S. has been publicly documented to date. However, to suppose similar flow conditions to those pertaining to gas stirred reactors (e.g., conventional argon stirred ladles) holds, could be quite erroneous as will be shown in the subsequent sections.

PREVIOUS WORK

Submerged gas injection into melts contained in ladles and similar transfer vessels has long been practised in the metal processing industries. Over the past decade or so, and owing to the importance of continuously cast steel, one has witnessed a rapid increase in the application of inert gas injection to steel processing vessels. This is particularly true for the chemical and thermal homogenisation of liquid steel in the teeming ladles. In order to control the process and to reach the desired metallurgical results, it is necessary to know the principal characteristics of the fluid's motion within the ladle during gas agitation.

Hydrodynamic analysis of such gas injection procedures have often made use of physical models in conjunction with mathematical models. Since the actual physical processes of gas bubbling are complex in the discrete sense, the mathematical formulation of such physical phenomena is plausible only by invoking a number of simplifying assumptions. Although, there still remains some areas for further development, 'The mathematical models for gas stirred ladles' have undergone considerable refinements, over the past decade.

In the following pages, these advances in the application of fluid dynamics to gas stirred metallurgical ladles have been summarised. Because of the breadth of the subject area, the

developments made in the mathematical modelling of these processes are only considered in this review.

Szekely, Wang and Kiser (4) were the first to attempt hydrodynamic modelling of an argon stirred ladle (i.e., axisymmetric gas injection in a cylindrical tank). In their analysis, they considered the upward movement of gas and liquid to be equivalent to the motion of a centrally placed solid core of material. At the interface between the core and the liquid, the hypothesis required the radial components of velocity to be zero. Consequently, only axial components of velocity were taken to be responsible for generating recirculation within the liquid. In the numerical solution scheme, the interface between the core and the bulk liquid was treated as one of the boundaries, at which the velocities were assumed known (these velocities at the interface were obtained by hot wire annemometry measurements in the water model). The bulk single phase flow field was predicted through solution of the Navier-Stokes equation (stream-function-vorticity based method (22)) together with the k-W (23) two equation model of turbulence. However for k and W equations rather unrealistic boundary conditions were applied (shear stress correlation for solid surface) at the interface between the bulk one phase, and the two phase gas-liquid, regions. Numerically predicted velocity and turbulence kinetic energy fields were found to be within an order of magnitude of those measured in the water model. In explaining these

discrepancies the authors acknowledged that the 'interface' between the rising core containing gas bubbles and the bulk of the liquid was not very satisfactorily defined and hence could be the source of a major error.

Since the above study, using a water model for testing the mathematical representation, was not conclusive because of the uncertainties in the representation of the gas-liquid region and the corresponding boundary conditions, Szekely, Dilawari and Metz (5) then studied the recirculatory flow pattern generated in a cylindrical vessel by a continuously moving cylindrical belt placed axisymmetrically and running at a velocity of 5 m/s. The numerical procedure was exactly identical to those reported in the previous publication (4). Nevertheless, for correct prediction of velocity and turbulence energy in the immediate vicinity of the solid walls, standard wall functions were used and recommended. It was found that predicted velocity and turbulence kinetic energy fields were in more satisfactory agreement with those measured.

Although, the mathematical models describing turbulent recirculatory flow systems have been found to yield quantitative results, yet, there remained the question of tackling the two phase nature of the flow in argon stirred ladles (i.e., the precise representation of the gas injection phenomena, so that hydrodynamic variables can be computed over the entire domain, without invoking any unrealistic constrains on the computational

scheme). In this respect, Debroy, Majumdar and Spalding (6) were the first to recognise the importance of buoyancy (i.e., free convection) in such systems and to propose computational schemes wherein the gas-liquid mixtures contained within the two phase jet region was represented by a fluid of variable density. The buoyancy force due to this density deficit in the two phase region was added to the axial momentum equation as a body force term. Symmetry boundary conditions (i.e., zero normal derivative) were applied to the flow variables. In order to estimate the density deficit in the gas liquid region, two distinct situations were considered i.e., 'no-slip', wherein the gas and liquid move together and, 'slip', wherein the velocity of the gas bubbles exceed that of liquid phase by a constant U_{slip}. In this calculation scheme, the superficial inlet velocity of gas was taken as a boundary condition for the deduction of voidages and so forth in the gas liquid region. Using an ad hoc eddy viscosity formula proposed by Pun and Spalding (24), these authors predicted the velocity field in a water model for the same conditions as those reported by Szekely and coworkers (4). Furthermore, it was concluded that satisfactory agreement between their predictions and Szekely et al's measurements could be achieved by assuming zero slip between the gas and the liquid phase. These authors used a numerical scheme based on primitive variables (u, v and p) in

which the pressure-velocity coupling was tackled by the SIMPLE (25) algorithm of Patankar and Spalding.

Parallel to the work of Debroy, Majumdar and Spalding, Szekely, Lehner and Chang (7) tackled the problem of axi-symmetric gas injection in argon stirred ladles from a slightly different viewpoint. These authors employed the same shear stress conditions (i.e., those used at the interface between the bulk liquid and the moving cylindrical belt (5)) to predict flow fields and eddy diffusivity values in 7 ton argon stirred ladle with an argon flow rate of 0.05 Nm^3/min and in a 60 ton ladle with an argon flow rate of 0.055 Nm^3/min. Again, a stream function-vorticity based numerical procedure was used together with the k-W (23) two equation turbulence model. However, boundary velocity values adjacent to the cylindrical core of gas were estimated from the 'plume curtain' rise velocity relationship given by Bulson (26). Mixing times based on predicted eddy diffusivities were calculated and claimed to be in good agreement with mixing times measured experimentally. Nevertheless, these authors again acknowledged that the greatest weakness of their model is that the representation of the plume (i.e., the bubble rich region of the vessel) was only approximate. They proposed further work for a more precise definition of the bubbling zone and the proper boundary conditions for its precise representation.

Some experimental studies on flows generated in a 60 ton steel melt stirred by argon were then reported by Hsiao Tse-Chiang, Lehner and Kjellberg (8). Central plume velocities were measured in a 60 ton ladle and in a water model ladle using a drag form - strain gauge system. Measured plume velocities were found to be closely represented by a Gaussian distribution curve. Furthermore, the average plume velocity was found to be proportional to (gas flow rate)$^{0.24}$, while the near surface velocity was found to be proportional to (gas flow rate)$^{0.33}$.

Szekely, El-Kaddah and Grevet (9) next adopted the computational procedures of Debroy et al. (6) described previously, to predict flow field and tracer dispersion in a water model of an argon stirred ladle. Slippage was assumed between the gas and the liquid phases and the gas voidage within the plume was calculated from the so called 'drift flux' (27) model. A primitive variable formulation was adopted by these authors for the first time. Turbulence within the system was modelled using the Pun-Spalding (24) formula. Measurements and predictions were claimed to be in fairly good agreement, except in the vicinity of the walls, where the discrepancy was attributed to an overestimation of effective viscosity by the Pun-Spalding (24) formula. Nevertheless, these authors concluded that use of Pun-Spalding effective viscosity formula could provide a satisfactory mean for performing engineering calculations.

This simplified effective viscosity model was also used to predict tracer dispersion in a pilot scale 6 ton vessel and very reasonable agreement achieved.

In a subsequent paper, El-Kaddah and Szekely (10) presented a mathematical model for desulphurisation kinetics in argon stirred ladle. The model involved prediction of turbulent flow fields through the solution of the Navier-Stokes equation in conjunction with the k-ε (28) two equation turbulence model. Sulphur transfer rates and equilibrium thermodynamic relationships were then combined with the turbulent flow field to predict rates of desulphurisation in 6 ton and 40 ton ladles respectively. Predicted rates were found to be in excellent agreement with experimental measurements. It was found that the rate of desulphurisation depended both on the rate at which sulphur is transferred through the melt to the reaction zone and on the equilibrium condition prevailing in this reaction zone. Consequently, fluid flow phenomena and turbulence were shown to be key parameters in determining desulphurisation kinetics.

Based on similar calculation procedures (6), Debroy and Majumdar (11) predicted liquid flow in gas stirred systems and highlighted the influence of bubble size, gas hold up, and the degree of slippage between the gas and the liquid phase on the bulk circulation of liquid within the vessel. The performance of the k-ε (28) turbulence model was assessed against the simple

algebraic viscosity model of Pun and Spalding (24). The effect of plume dimensions on numerical predictions was also analysed and it was demonstrated that significant variations of flow (only magnitude) occur near the axis of symmetry, while in the bulk of the liquid, the plume dimensions seem to have an insignificant effect. Also the wall shear stresses on the ladle side walls were computed and their possible influence on refractory design discussed. It was recognised by these authors that depending on bubble size and extent of gas hold up in the system, physically two different situations i.e., zero slip and no slip might exist in such systems.

As mentioned previously, Debroy, Majumdar and Spalding (6), and Szekely, El-Kaddah and Grevet (9), adopted the bulk effective viscosity formula of Pun and Spalding (24) for predicting flow in gas stirred liquid metal systems. In reviewing the applicability of the Pun-Spalding (24) formula to typical ladle metallurgy situations (i.e., argon stirred ladles), Sahai and Guthrie (12) recognised that certain ambiguities are associated with its use. Through dimensional arguments, energy considerations and numerical solution of the governing differential equations (i.e., turbulent Navier-Stokes equation) they proposed: $\mu_T = 5.5 \times 10^{-3} \rho_L L\{(1-\alpha)gQ/D\}^{1/3}$. Sahai and Guthrie further noted that their effective viscosity model is conceptually different from the Pun-Spalding formula for combustion flow system: $\mu_e = 0.012 D^{2/3} L^{-1/3} \rho_L^{1/3} \{\dot{m} U_o^2\}^{1/3}$. It is to be

noted here that the formula proposed by Sahai and Guthrie (12) emphasizes the potential energy of the incoming gas, whereas the Pun-Spalding formulation emphasizes the kinetic energy of the incoming gas.

Following direct measurements of central plume velocities at various gas flow rates by Hsiao Tse-chiang, Lehner and Kjellberg (8), Sahai and Guthrie (13) considered the question of gas stirred systems from a new stand point. Appreciating the relevance of hydrodynamic coupling between widely dispersed, large rising bubbles and entrained liquid within the ascending plume, they proposed, how plume rise velocities in such vessels could be calculated from first principles. In estimating plume velocities, any slippage between gas and liquid phases were ignored. This new information has allowed flow fields generated by submerged gas injection in any system to be predicted. Their analysis however was restricted to a bubble column or plume, rising axisymmetrically in a cylindrical vessel. Based on information available on submerged gas jets, Sahai and Guthrie argued that any submerged gas envelope, penetrating the liquid will become hydrodynamically unstable and break down within a relatively short distance of the nozzle or orifice to form an array of spherical cap bubbles. Each of these bubbles will entrain a volume of liquid in its wake which, in turn, is exchanged with the bulk liquid as the bubble rises. By this means, the rising bubble imparts energy to the liquid recircu-

lating within the bath. Under steady state conditions, it was argued that the mean velocity at any location within the vessel must become constant, at which time the total energy supplied by the bubbles to the bulk of the liquid would equal the total turbulent energy dissipation losses within the bath. This dissipation loss was calculated using the two equation k-ε (28) turbulence model. From this mathematical treatment it was shown that the average rise velocity of the bubble plume, $U_p \alpha (Q^{1/3} L^{1/4})/R^{1/3}$ where Q is the gas flow rate adjusted to mean height and temperature of the bath, L is the depth of liquid and R is the radius of the vessel.

Sahai and Guthrie (14) also developed a mathematical model for gas stirred ladles through the solution of turbulent Navier-Stokes equation. Their numerical procedure was based on the SIMPLE (25) algorithm of Patankar and Spalding. The gas/liquid region was treated by the GALA (29) method of Spalding. However, instead of using a zero gradient boundary condition at the axis of symmetry for the axial component of velocity, they used a fixed centre line boundary condition at the axis of symmetry, deduced from their plume model described earlier. Predicted results in a 0.17 scale water model of a 150 ton ladle were found to be in excellent agreement with those measured experimentally. Predictions of velocity fields in a one ton water model were also made for comparison with experimental velocity profiles in the gas-liquid plume region, as

measured by Hsiao Tse-chiang, Lehner and Kjellberg (8) in their pilot scale water model.

Grevet, Szekely and El-Kaddah (3) reported an extensive theoretical and experimental study in a water model of an argon stirred ladle. The computational procedure adopted by these authors were identical to those reported in a previous publication (9), although, Pun-Spalding (24) effective viscosity formula was replaced by the more advanced k-ε (28) differential model of turbulence. These authors observed that predicted and experimental velocity fields were in excellent agreement while predicted and experimental turbulence kinetic energy fields were in reasonable agreement. Nonetheless, there were some serious discrepancies between measured and predicted Reynolds stress components. These discrepancies were attributed to the incorrect selection of constants and with inherent shortcomings of the k-ε (28) model for representing systems of this type. On the basis of measurements, they concluded that except in the vicinity of solid wall, turbulence was found to be largely isotropic. Furthermore, they considered that the principal mechanism of momentum transfer in these systems is associated with fluid convection, rather than with the diffusive transport mechanism and thus the predictions regarding the velocity fields are not expected to be very sensitive to the particular turbulence model chosen.

McKelliget, Cross and Gibson (15) proposed a fluid flow model of these gas agitated reactors, which in essence is different from those discussed so far. A retrieved variable (stream function and vorticity) based numerical method was used and the gas liquid mixture was represented as a continuous fluid (i.e., no slip) of variable density. However, the density deficit in the plume and the plume dimension were not specified a priori. Instead, the gas dispersion was described by a turbulent diffusion equation. The gas fraction at any control volume was estimated from the turbulent diffusion equation and then the corresponding nodal value of density was estimated. From these the buoyancy force owing to reduced density was estimated and added to the vorticity transport equation. Turbulence within the system was described via the Pun-Spalding (24) viscosity formula. The model was applied to analyse three injection configurations i.e., injection vertically upwards, vertically downwards through a submerged lance and horizontally through a bank of tuyers. In the latter case only a two dimensional slice of a three dimensional domain was considered. The numerical predictions were compared against the experimental measurements of Szekely et al. (4) and semi quantitative agreement was found. For injection vertically downwards, the model predictions were also found to be in semi-quantitative agreement with the available experimental evidence. However, the model's application to horizontal injection failed to give

adequate predictions. In this regard, the requirement for a model which is more comprehensive in its scope (i.e., 3D, transient etc.) was highlighted.

A single phase 3 dimensional model for predicting flow fields and associated phenomena with asymmetric gas driven flows in systems of cylindrical geometry was first proposed by Salcudean, Low, Hurda and Guthrie (16). The model used a finite difference technique based on the MAC (30,31) (Marker and Cell) method of the Los Alamos group. Both slip and non slip conditions were assessed. Turbulence within the system was modelled using the ad hoc eddy viscosity formula of Pun and Spalding (24). The three dimensional code was validated by performing some two dimensional axisymmetrical calculations and comparing the solution with an equivalent calculation of Debroy et al.(6) and with the experimental results of Szekely et al. (4). Satisfactory agreement was found by assuming zero slip between the gas and the liquid phase. Flow fields were predicted by considering the rising plume to be conical as well as cylindrical. Fluid flow is some asymmetric gas injection configurations were also assessed by these authors. Finally, the temperature fields in an initially stagnant and thermally stratified liquid resulting from the local introduction of the gas on the bottom surface was also considered.

More recently, Salcudean, Lai and Guthrie (17) reported further computations and compared those with experimental

results of Oeters, Dromer and Kepura (32). Using their three dimensional code, the velocity field for a typical axisymmetric gas injection situation was predicted. To model turbulence within the system, bulk effective viscosity formulae (12,24) together with the $k-\varepsilon$ (28) two equation turbulence model were tested. These flow and turbulence parameter fields were used to solve the energy and concentration equations. It was found that the algebraic models for turbulence diffusivities in heat, mass and momentum equations were able to reproduce experimental observations closely. However, for the physical situation considered, the void fraction in the bubble plume was deduced by assuming slip between the gas and the liquid phases.

The mathematical models reviewed so far are essentially single phase models, where, the gas-liquid region has been considered to be a fluid of variable density, restricted to a region, whose dimension is known. On the other hand, theoretical formulations for a mathematical model capable of taking into consideration the two phase nature of the flow in gas stirred systems have been recently proposed by Markatos and coworkers (20,21). Such a two phase model uses the continuous mixture approach and formulates the governing equations on the basis that mass, momentum and energy fluxes are balanced over control volumes occupied by space sharing interspersed and mutually slipping phases. The governing equations (i.e., vol. continuity, u, v, w, k and ε) were written for the gas and the liquid

phases respectively and were solved numerically retaining the primitive variables, using the IPSA (29) algorithm, which is a development of the SIMPLE (25) algorithm. Standard boundary conditions were used at the symmetry axis and at the walls. However, at the free surface, a fixed pressure boundary condition was applied on the pressure equation, rather than applying any boundary condition on u, v and w at the free surface. Furthermore, at the orifice, the velocity of gas was set equal to the superficial velocity of the gas phase (i.e., a given quantity). It was acknowledged that application of $k-\varepsilon$ (28) and other two equation turbulence models are questionable particularly for two phase flow systems. However, these authors used the $k-\varepsilon$ (28) model in view of the lack of other information. Furthermore in order to estimate the interphase friction force appearing in the coupled momentum equations, the drag coefficient - Reynolds number relationship for spherical bubbles, based on slip velocities were used. Finally, the predictions (velocity and turbulence kinetic energy) were compared against the experimental measurements reported by Grevet et al.(3), and satisfactory agreement achieved.

THEORY

A. Modelling Criteria

Assumptions in modelling

Inert gas injection into liquid metal holding vessels is a complex process. The presence of slag, probable thermal and concentration gradients in the molten metal and waves and oscillations at the free surface etc. all necessarily aggravate such complexity. Consequently, in order to describe such a system via an adequate mathematical model, certain simplifications and assumptions need to be invoked. The following assumptions were made in the mathematical formulation:

(1) The possible influence of a slag layer at the top of liquid steel has been ignored.

(2) The system has been assumed to be isothermal.

(3) The wavy free surface has been approximated by a flat mobile surface.

(4) The gas liquid region has been assumed confined to a cone, whose dimensions in the water model were measured, while the plume is calculated for the real ladle.

(5) Any slip between the bubbles and the liquid were neglected. Consequently, it is implicitly assumed that the gas liquid mixture behaves as a single phase fluid, having its own thermodynamic and transport-property relations.

(6) Bulk flow of liquid was thus induced by the density differences between the bulk one phase and the gas-liquid mixture.

The implications of some of these assumptions are elaborated upon in the text.

Similarity criteria

In studying ladle metallurgy operations, a reduced scale water model is very often employed. To carry out such a model study, it is important to identify the essential factors which dominate in both the real and model systems, so as to preserve similarity between the two.

To obtain quantitative results, it is necessary to maintain mechanical as well as geometrical similarity. The term 'mechanical similarity' incorporates three components: static similarity, kinematic similarity and dynamic similarity. For fluid flow problems, the latter two are important. Kinematic similarity requires that corresponding particles in geometrically similar systems trace out geometrically similar paths in corresponding intervals of time. In many cases it is more convenient to calculate the time scale ratio in terms of 'corresponding velocities', which are the velocities of corresponding particles at corresponding times.

Finally, dynamic similarity which is concerned with those forces which affect the movement of masses in dynamic systems, requires that forces of the same kind (e.g., gravitational etc.) acting upon corresponding particles at corresponding times should also correspond. In fluid systems, kinematic similarity necessarily entails dynamic similarity.

Provided the governing equations of the systems are known, it is relatively easy to deduce key factors in modelling. Johnstone and Thring (33) showed a method for deriving similarity criteria based on the differential equations describing the behaviour of the system.

For fluid flow in a gas stirred ladle, flow fields are essentially expressed in terms of the Navier-Stokes equation. For reasons of simplicity, consider the Navier-Stokes equation for a steady one dimensional flow problem. Expressed in Cartesian co-ordinates, this takes the form:

$$\rho u \frac{du}{dx} = - \frac{dp}{dx} + \mu \frac{d^2u}{dx^2} + \rho g \qquad (1.1)$$

As equation (1.1) must apply for both the real system (system 1) and the model system (system 2),

$$\rho_1 u_1 \frac{du_1}{dx_1} = - \frac{dp_1}{dx_1} + \mu_1 \frac{d^2u_1}{dx_1^2} + \rho_1 g_1 \qquad (1.2)$$

and

$$\rho_2 u_2 \frac{du_2}{dx_2} = - \frac{dp_2}{dx_2} + \mu_2 \frac{d^2u_2}{dx_2^2} + \rho_2 g_2 \qquad (1.3)$$

Supposing that linear relationships between variables in equations (1.2) and (1.3) are applied; i.e.,

$$\rho_2 = K_\rho \rho_1 \qquad u_2 = K_u u_1$$

$$x_2 = K_L x_1 \qquad p_2 = K_p p_1 \tag{1.4}$$

$$\mu_2 = K_\mu \mu_1 \qquad g_2 = K_g g_1$$

Then substituting equations (1.4) in equation (1.3), we obtain:

$$\frac{K_\rho K_u^2}{K_L} \rho_1 u_1 \frac{du_1}{dx_1} = -\frac{K_p}{K_L} \frac{dp_1}{dx_1} + \frac{K_\mu K_u}{K_L^2} \mu_1 \frac{d^2 u_1}{dx_1^2} + K_\rho K_g \rho_1 g_1 \tag{1.5}$$

Comparing equations (1.2) and (1.5), the following equations must be satisfied to maintain similarity between the two systems.

$$\frac{K_\rho K_u^2}{K_L} = \frac{K_p}{K_L} = \frac{K_\mu K_u}{K_L^2} = K_\rho K_g \tag{1.6}$$

From these equations, we can obtain the following independent relations:

$$\frac{K_\rho K_u^2}{K_p} = 1 \tag{1.7}$$

$$\frac{K_\rho K_u K_L}{K_\mu} = 1 \tag{1.8}$$

$$\frac{K_u^2}{K_L K_g} = 1 \tag{1.9}$$

Substituting equation (1.4) in equations (1.7) ∿ (1.9), we can obtain the following dimensionless groups:

From equation (1.7),

$$\frac{\rho_1 u_1^2}{p_1} = \frac{\rho_2 u_2^2}{p_2} \tag{1.10}$$

This equation shows that the ratio of kinetic energy to pressure should be identical between model and the real system.

From equation (1.8), we also require that,

$$\frac{x_1 \rho_1 u_1}{\mu_1} = \frac{x_2 \rho_2 u_2}{\mu_2} \tag{1.11}$$

This group is the well known Reynolds number, representing the ratio of inertial to viscous forces.

From equation (1.9),

$$\frac{u_1^2}{x_1 g_1} = \frac{u_2^2}{x_2 g_2} \tag{1.12}$$

The latter group is a Froude number, representing the ratio of inertial to gravitational forces.

These dimensionless groups indicate that the steady state form of the Navier-Stokes equation in dimensionless form may be written as:

$$\phi' \left(\frac{\rho u^2}{p}, \frac{\rho uL}{\mu}, \frac{u^2}{gL}\right) = \text{constant} \qquad (1.13)$$

or,

$$\frac{\rho u^2}{p} = \phi'' \left(\frac{\rho uL}{\mu}, \frac{u^2}{gL}\right)$$

or $$\left(\frac{1}{N_{Eu}}\right) = \phi'' (N_{Re}, N_{Fr}) \qquad (1.14)$$

Dimensional analysis of fluid flow including surface tension as one of the factors, indicates the possible importance of another dimensionless group, known as the Weber number;

$$\frac{\rho u^2 L}{\sigma} = N_{We} \qquad (1.15)$$

If one includes this number, similarity criteria for the system considered can be expressed as;

$$\frac{\rho u^2}{p} = \phi''' (N_{Re}, N_{Fr}, N_{We}) \qquad (1.16)$$

The relative importance of these three dimensionless numbers and the modelling criteria are discussed in the next section.

In these modelling investigations, thermal similarity was not considered as mentioned previously. Consequently, the possible effects of natural convection have been ignored. This is justified in the present case since most of energy responsible for generating the flow fields in this case derives from the buoyancy action of the upwelling gas-liquid mixture.

Modelling criteria

In general, the Reynolds, Froude, Euler and Weber numbers are considered to be important in fluid flow problems as discussed in the last section. Expressing these dimensionless groups using characteristic symbols for the variables:

$$N_{Re} = \frac{\rho u L}{\mu} \tag{1.17}$$

$$N_{Fr} = \frac{u^2}{gL} \tag{1.18}$$

$$N_{Eu} = \frac{p}{\rho u^2} \tag{1.19}$$

$$N_{We} = \frac{\rho u^2 L}{\sigma} \tag{1.20}$$

In the case considered here, because the equation of motion for flow within the bulk is described by the Navier-Stokes equation,

the role of surface tension is not relevant, except possibly at the upper free surface.

Table 1.1 gives the physical properties of liquid steel and water. It is well known that the kinematic viscosities of water and liquid steel are almost identical. This is one of the reasons why water models are commonly used for investigation of ladle metallurgy. In a full size model, i.e., $L_m = L_{f.s}$, it would be possible to simultaneously keep respective Reynolds and Froude numbers identical by using a same characteristic velocity (e.g., gas flow rate) in the model as that in the full scale system.

However, in a reduced scale model employing fluid of the same kinematic viscosity, it is impossible to respect similarity criteria for both the Reynolds and Froude number.

Therefore, in this investigation, it is assumed that the process is essentially a Froude dominated phenomenon. This assumption is supported by the notion that the inertia of the recirculating liquid in such gas stirred system is balanced by the body force (i.e., buoyancy force in this case) generated by gas injection. Consequently, applying Froude criterion between the model and full scale system, one finds

$$\left(\frac{\bar{U}^2}{gL}\right)_{\text{model}} \simeq \left(\frac{\bar{U}^2}{gL}\right)_{\text{full scale}} \qquad (1.21)$$

Table 1.1 Physical properties of water at 293 K and steel at 1873 K

	Water (293 K)	Steel (1873 K)
Molecular viscosity, kg/(m-s)	0.001	0.0064
Density, kg/m^3	1000	7000
Kinematic viscosity, m^2/s	1×10^{-6}	0.91×10^{-6}
Surface tension, Newton/m	73×10^{-3}	$1600^{*} \times 10^{-3}$

Adopting the empirical correlation proposed by Sahai and Guthrie (13) one can express $\bar{U}$, the mean speed of liquid recirculation, according to

$$\frac{\bar{U}}{U_P} R^{1/3} = \text{Constant} \tag{1.22}$$

Substituting $\bar{U}$ from equation (1.22) in terms of U_p and R in equation (1.21), gives the following relationship between the model and the full scale systems

$$\left|\left(\frac{U_P/R^{1/3}}{gL}\right)^2\right|_m = \left|\left(\frac{U_P/R^{1/3}}{gL}\right)^2\right|_{f.s} \tag{1.23}$$

using geometrical similarity between the model and the full scale system (i.e., $L_m = \lambda L_{f.s}$), one finds that the corresponding plume velocities in the model and full scale system can be expressed via,

$$\frac{(U_P)_m^2}{(U_P)_{f.s}^2} = \frac{L_m}{L_{f.s}} * \frac{R_m^{2/3}}{R_{f.s}^{2/3}} \tag{1.24}$$

or

$$\frac{(U_P)_m}{(U_P)_{f.s}} = \lambda^{5/6} \tag{1.25}$$

Using the macroscopic plume model of Sahai and Guthrie (13) for such gas injection systems, it is possible to express the average plume velocity U_P according to:

$$U_P = K_o (1-\alpha)^{1/12} \cdot \frac{Q^{1/3} \cdot L^{1/4}}{R^{1/3}} \qquad (1.26)$$

where K_o is a dimensional constant.

Substituting U_P from equation (1.26) into equation (1.25), one finally obtains,

$$\frac{|(1-\alpha)^{1/12} \cdot Q^{1/3}|_m}{|(1-\alpha)^{1/12} \cdot Q^{1/3}|_{f.s}} = \lambda^{11/12} \qquad (1.27)$$

If we now assume that the volume fraction of gas in the plume, in model and full scale system are identical, then equation (1.27) reduces to

$$\frac{Q_m}{Q_{f.s}} = \lambda^{11/4} \qquad (1.28)$$

This allows one to deduce corresponding flow rates between the model and the full scale system.

Equation (1.28) provides the key to modelling submerged gas injection systems from first principles.

Thus, under the assumption of a Froude dominated phenomenon, the relationships between the variables in the real process and those in the model can be expressed as follows:

Ladle diameter	D_m	$= \lambda D_{f.s}$	(1.29)
Liquid depth	L_m	$= \lambda L_{f.s}$	(1.30)
Gas flow rate	Q_m	$= \lambda^{11/4} . Q_{f.s}$	(1.31)
Receptacle diameter	d_m	$= \lambda . d_{f.s}$	(1.32)
Receptacle depth in liquid	l_m	$= \lambda . l_{f.s}$	(1.33)

B. Mathematical Formulation

The C.A.S. flow problem was set in its existing industrial form. This involves the central injection of gas into a cylindrical vessel in which a concentric refractory cylinder is placed around the bubble plume. Thanks to this symmetry, flow phenomena are adequately described via a two dimensional flow model in terms of cylindrical polar coordinates.

As will be shown later, the modelling and experimental work were carried out in two stages. At first axisymmetric gas injection into cylindrical vessels by partially, and fully, submerged lances was considered and then the presence of a surface baffle/snorkel around the rising gas liquid plume was taken into account.

For modelling turbulence within the system, an algebraic model for liquid submerged gas injection systems together with the two equation k-ε turbulence model (28) were employed.

The flow equations

For the situation of axisymmetric gas injection, the flow variables considered were assumed to obey axial symmetry (i.e., there is no variation of flow properties in the θ direction). Then in cylindrical polar coordinates, the governing differential equations may be represented as:

Equation of continuity,

$$\frac{\partial u}{\partial z} + \frac{1}{r} \frac{\partial (rv)}{\partial r} = 0 \qquad (1.34)$$

Equation of motion in axial direction,

$$\frac{\partial}{\partial z} (\rho uu) + \frac{1}{r} \frac{\partial}{\partial r} (\rho ruv) = - \frac{\partial p}{\partial z} + \frac{\partial}{\partial z} (\mu_{eff} \frac{\partial u}{\partial z}) + \frac{1}{r} \frac{\partial}{\partial r} (r\mu_{eff} \frac{\partial u}{\partial r}) + S_u \qquad (1.35)$$

where

$$S_u = \frac{\partial}{\partial z} (\mu_{eff} \frac{\partial u}{\partial z}) + \frac{1}{r} \frac{\partial}{\partial r} (r\mu_{eff} \frac{\partial v}{\partial z}) + \rho_L g\alpha \qquad (1.36)$$

Equation of motion in radial direction,

$$\frac{\partial}{\partial z}(\rho uv) + \frac{1}{r}\frac{\partial}{\partial r}(\rho rvv) = -\frac{\partial p}{\partial r} + \frac{\partial}{\partial z}\left(\mu_{eff}\frac{\partial v}{\partial z}\right) + \frac{1}{r}\frac{\partial}{\partial r}\left(r\mu_{eff}\frac{\partial v}{\partial r}\right) + S_v \qquad (1.37)$$

where

$$S_v = \frac{\partial}{\partial z}\left(\mu_{eff}\frac{\partial u}{\partial r}\right) + \frac{1}{r}\frac{\partial}{\partial r}\left(r\mu_{eff}\frac{\partial v}{\partial r}\right) - \mu_{eff}\frac{v}{r^2} \qquad (1.38)$$

The term involving the gas voidage α, and appearing in the axial momentum equation, was used to model the buoyancy force generated by differences in density between the bulk one phase, and the plume two-phase, regions. In the present investigation, α was deduced from a knowledge of plume velocity and shape (see later). In estimating the average plume velocity, slip between gas bubbles and the liquid phase within the plume were ignored. A detailed discussion on bubble slippage within gas stirred reactors is available in reference 13. However, it is to be mentioned that Debroy et al. (6) and Salcudean et al. (16) applied both slip and nonslip models to analyse such physical situations. In their attempts to compare numerical predictions with the experimental measurements of Szekely et al. (4), they found that very reasonable agreement could be achieved by assuming zero slip condition.

The turbulence models

Two turbulence models were used. The first, an algebraic model developed by Sahai and Guthrie (12), is based on the concept that the main form of energy input into a gas stirred ladle of liquid steel (or any other liquid) is primarily potential energy. Through dimensional arguments and energy considerations, they showed that an effective, or average, viscosity for such gas stirred systems is expressed by:

$$\mu_{eff} = C\rho_L L \left\{\frac{(1-\alpha) g Q}{D}\right\}^{1/3} \qquad (1.39)$$

The second turbulence model used was the popular k-ε turbulence model of Launder and Spalding (28). The governing transport equations for turbulence kinetic energy, k, and its dissipation rate, ε, can be represented in cylindrical polar coordinate as (28).

Turbulence kinetic energy:

$$\frac{\partial}{\partial z}(\rho u k) + \frac{1}{r}\frac{\partial}{\partial r}(\rho r v k) = \frac{\partial}{\partial z}\left(\frac{\mu_{eff}}{\sigma_k} \cdot \frac{\partial k}{\partial z}\right) + \frac{1}{r}\frac{\partial}{\partial r}\left(r\frac{\mu_{eff}}{\sigma_k} \cdot \frac{\partial k}{\partial r}\right) + S_k \qquad (1.40)$$

where S_k, the net source term, can be represented as

$$S_k = G - \rho\varepsilon$$

and

$$G = \mu_T \left\{2\left[\left(\frac{\partial u}{\partial z}\right)^2 + \left(\frac{\partial v}{\partial r}\right)^2 + \left(\frac{v}{r}\right)^2\right] + \left(\frac{\partial u}{\partial r} + \frac{\partial v}{\partial z}\right)^2\right\} \qquad (1.41)$$

Dissipation rate of turbulence energy:

$$\frac{\partial}{\partial z}(\rho u \varepsilon) + \frac{1}{r}\frac{\partial}{\partial r}(\rho r v \varepsilon)$$

$$= \frac{\partial}{\partial z}\left(\frac{\mu_{eff}}{\sigma_\varepsilon} \cdot \frac{\partial \varepsilon}{\partial z}\right) + \frac{1}{r}\frac{\partial}{\partial r}\left(r \frac{\mu_{eff}}{\sigma_\varepsilon} \cdot \frac{\partial \varepsilon}{\partial r}\right) + S_\varepsilon \qquad (1.42)$$

where

$$S_\varepsilon = \frac{C_1 \varepsilon G}{k} - \frac{C_2 \rho \varepsilon^2}{k}$$

Effective viscosity, $\mu_{eff} = \mu_L + \mu_T$ (1.43)

where $\mu_T = C_D \rho k^2/\varepsilon$ (1.44)

and $\rho = \alpha \rho_G + (1 - \alpha)\rho_L$ (1.45)

Following the recommendation of Launder and Spalding (28), the five constants appearing in equations (1.40) through (1.44) take the values given in Table 1.2.

Table 1.2 Values of constants in k-ε turbulence model (28)

C_1	C_2	σ_k	σ_ε	C_D
1.43	1.92	1.00	1.30	0.09

The macroscopic plume model

Consider the case of axisymmetric gas injection into a cylindrical vessel, in which the lance is submerged to a depth of βL, where L is the depth of liquid within the ladle and β is a fraction such that $0 < \beta < 1$.

In estimating the average velocity of such a plume, U_p, the macroscopic plume model developed by Sahai and Guthrie (13) was used as a starting point. Thus, for the case of central gas injection at the base of a ladle, the average plume velocity U_p was shown to be related to gas flow, Q, liquid depth, L, and ladle radius, R, in the following manner:

$$U_p = k'' \frac{Q^{1/3} L^{1/4}}{R^{1/3}} \tag{1.46}$$

In developing the model, in which gas was injected at the ladle's base, the residence time of each bubble in the rising plume was computed according to

$$t_R = \frac{L}{U_p} \tag{1.47}$$

from which the number of discrete bubbles in an idealized ascending plume was calculated to be:

$$N_B = \frac{Q}{V_B} \cdot \frac{L}{U_p} \tag{1.48}$$

In the present study with gas injection at fractional depths, βL, this equation (i.e., equation (1.48) needs to be rewritten as

$$N_B = \frac{Q}{V_B} \cdot \frac{\beta L}{U_P} \tag{1.49}$$

where the residence time of each bubble now corresponds to

$$t_R = \frac{\beta L}{U_P}$$

Based on equivalent arguments, it can be shown that the effective viscosity formula developed by the same authors (12) for gas stirred reactors can be modified to

$$\mu_{eff} = CL\rho_L \left|\frac{\beta(1 - \alpha)gQ}{D}\right|^{1/3} \tag{1.50}$$

in comparison to

$$\mu_{eff} = CL\rho_L \left|\frac{(1 - \alpha)gQ}{D}\right|^{1/3} \tag{1.51}$$

With these adjustments, a more generalized version of the macroscopic plume model equation can be introduced:

$$U_P = k'' \beta^{1/3} \frac{Q^{1/3} L^{1/4}}{R^{1/3}} \tag{1.52}$$

Through substitution of appropriate physical values for ladle radius (R), bath depth (L), gas flow rate (Q), and fractional submergence of lance (β), an average plume velocity can be calculated.

Applying the principle of volume continuity, the volume fraction of gas (α) in the gas liquid region can also be readily calculated from the following expression:

$$\alpha = \frac{Q \frac{\beta L}{U_p}}{\pi r_{av}^2 \beta L} \qquad (1.53)$$

Boundary conditions

The boundary conditions used for the numerical solution of the above set of partial differential equations are:

At the axis of symmetry, $(r = 0,\ 0 < z < L)$

$$v = 0$$

$$\frac{\partial u}{\partial r} = 0; \quad \frac{\partial k}{\partial r} = 0 \text{ and } \frac{\partial \varepsilon}{\partial r} = 0$$

At the free surface, $(z = L,\ 0 < r < R)$

$$u = 0$$

$$\frac{\partial v}{\partial z} = 0; \quad \frac{\partial k}{\partial z} = 0 \text{ and } \frac{\partial \varepsilon}{\partial z} = 0$$

At the side walls and bottom surface,

$$u = 0; \quad v = 0; \quad k = 0 \quad \text{and} \quad \varepsilon = 0$$

Close to the vicinity of the walls and the bottom surface, where variations in flow properties are steep, the momentum (u and v) and scalar (k and ε) fields were modelled using wall functions (i.e., logarithmic velocity profile for parallel velocity component etc.). The latter procedures are standard (28) and are not reproduced here.

C. Calculation Procedure

Numerical procedure

Discretization equations derived from equation (1.34) through equation (1.38) and from equation (1.40) through equation (1.44) were solved using an implicit finite difference procedure incorporated in the TEACH-T program code and referred to as SIMPLE (25) (Semi-Implicit Method for Pressure Linked Equations).

For analysis of the gas-liquid region, the GALA (29) (Gas and Liquid Analyser) procedure was incorporated into the SIMPLE algorithm. In this, the physical properties of the fluid mixture in a cell in the two phase region was averaged on a volumetric basis. This required the conventional mass continuity equation being replaced by a volume continuity equation, such that the volume of fluids entering a volume element equalled the total volume of fluids flowing out. Evidently there can be

significant discrepancies between the total mass inflow and outflow to cells on the edge of the plume when modelling a two phase flow system using a single phase approximation (29). The use of GALA allowed computation of hydrodynamic variables over the entire flow domain.

A variable grid network (typically 24 x 16) was chosen for obtaining numerical solutions. Computations were performed on McGill's Amdahl V7 machine. A typical execution required nearly 700 iterations. This corresponded to an execution time of about 162 seconds. A convergence criterion was set (<.005) on all variables, and computations were carried out until the absolute sum of residuals on u, v and volume continuity fell below the stipulated value. A typical grid system is presented in Fig. 1.1.

Modified numerical procedure for central refractory cylinder in the C.A.S. method

The refractory cylinder placed over the eye of the bubble plume, represents a static solid obstacle within the flow system. At the surface of this obstacle, and within the obstacle itself, the numerical procedures must predict zero velocities. Evidently, flow fields must be modelled precisely both in the convective and diffusive sense if temperature and solute distributions are to be predicted with any accuracy. To ensure solutions were independent of numerical procedures, two different techniques (34,35) were used to predict flow fields.

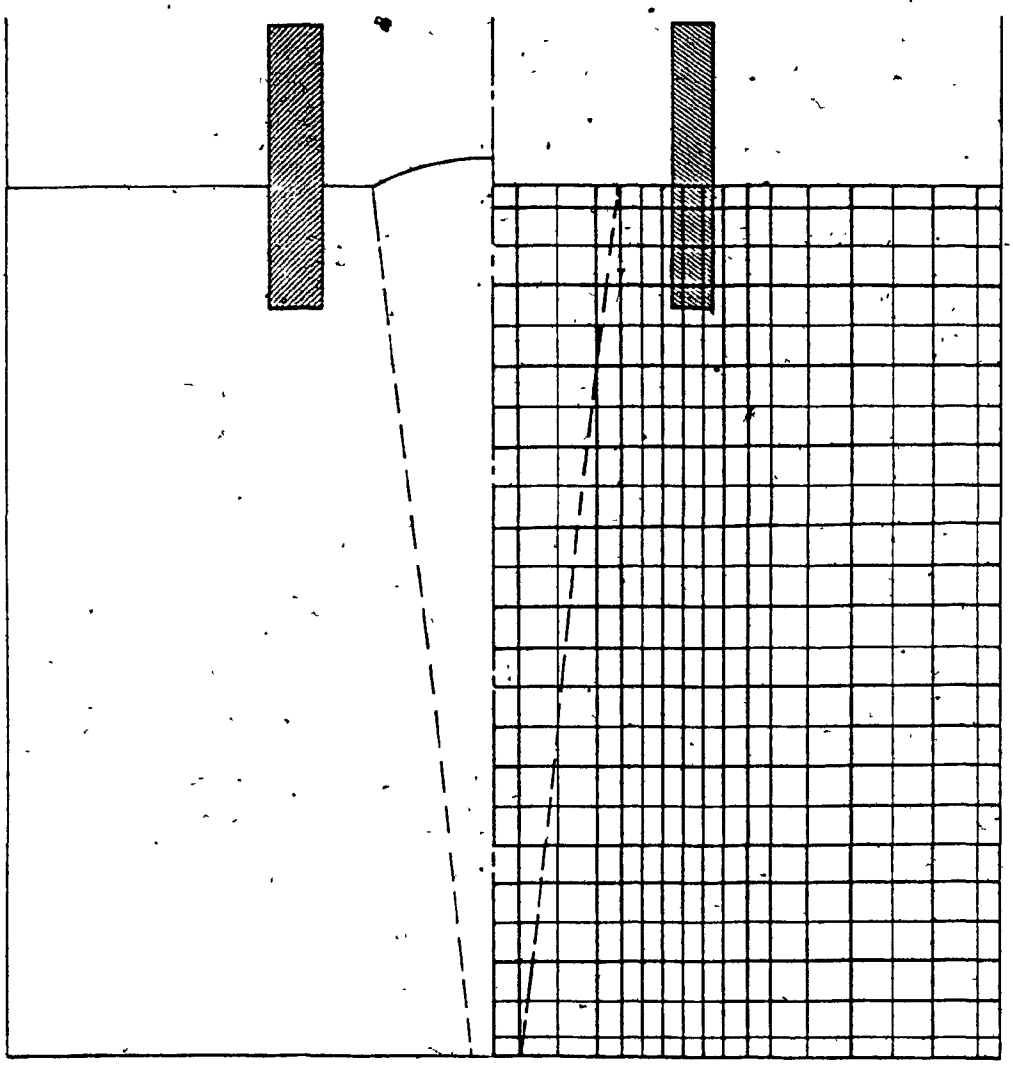

Figure 1.1 Schematic of the C.A.S. alloy addition system, illustrating central gas injection and the grid networks used for the mathematical representation.

The first technique (34) assigned artificially high values of viscosity and low transport coefficients within the obstacle, together with zero velocities at the surface of the obstacle. The second procedure (35) introduced the concept of volume elements (cells) of zero, or fractional, porosity. The two methods are compared by plotting the vertical components of the flow at two different axial heights in Fig. 1.2. As seen, the agreement achieved was excellent.

In the cell blockage procedure (35) the problem was solved in a calculation domain which included both solid and liquid regions. The finite difference grid chosen for encompassing the cylindrical obstacle is illustrated in Fig. 1.3. It can be shown (36) that the discretization equation for a general variable ϕ(u,v,k,ε or m_i) at any nodal point P can be represented in terms of its neighbours (E,W,N and S) as:

$$A_P\phi_P = A_E\phi_E + A_W\phi_W + A_N\phi_N + A_S\phi_S + S \qquad (1.54)$$

Here, A's are the coefficients representing both convection and diffusion of ϕ, while S stands for the 'source term' defined as:

$$S = S_c + S_P\phi_P \qquad (1.55)$$

S_c and S_P are the two functions which depend on the particular ϕ variable concerned, and result by casting the particular

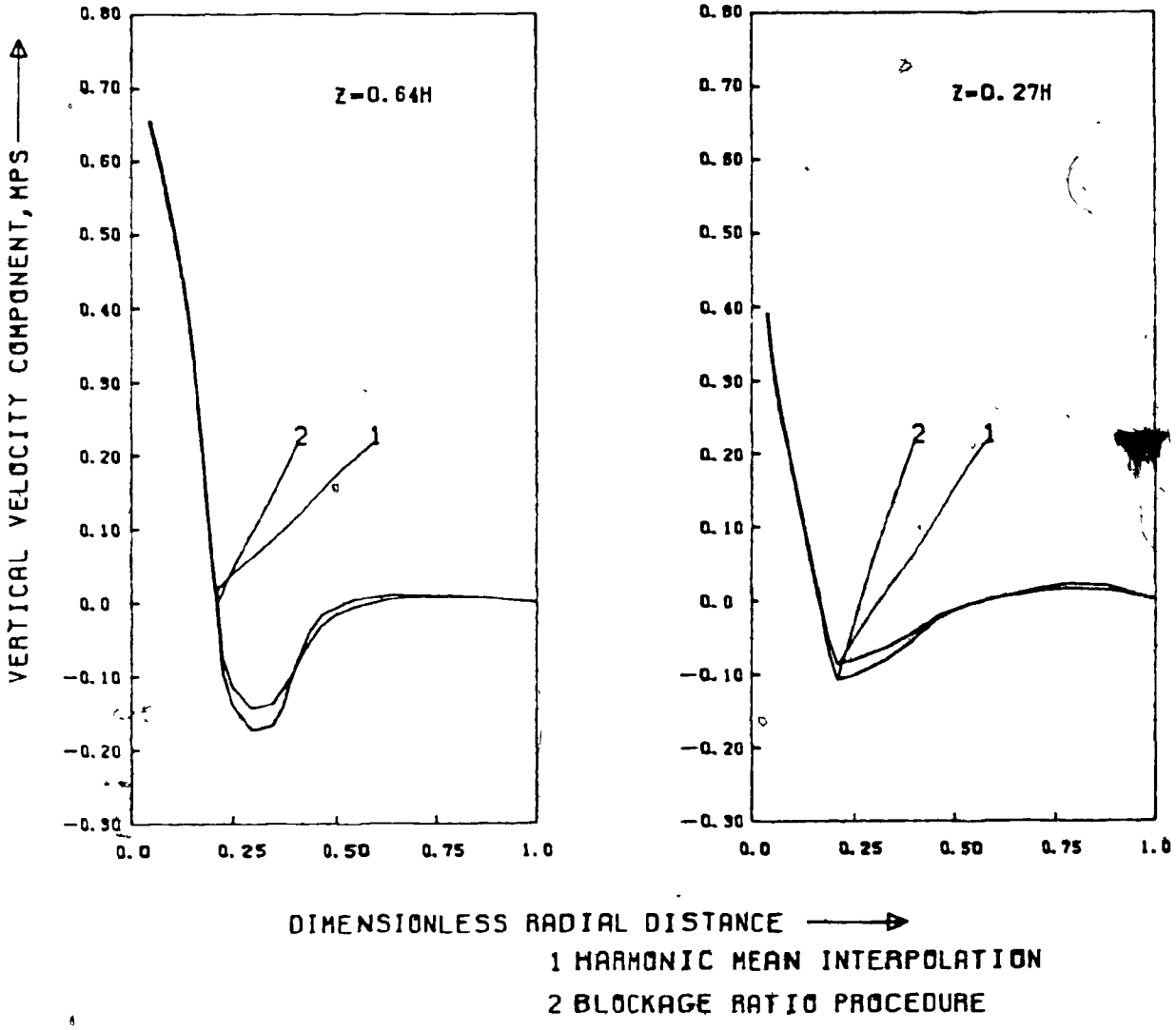

Figure 1.2 Predicted distribution of the vertical component of the flow in the water model using two alternative numerical approaches for modelling the central plexiglass cylinder.

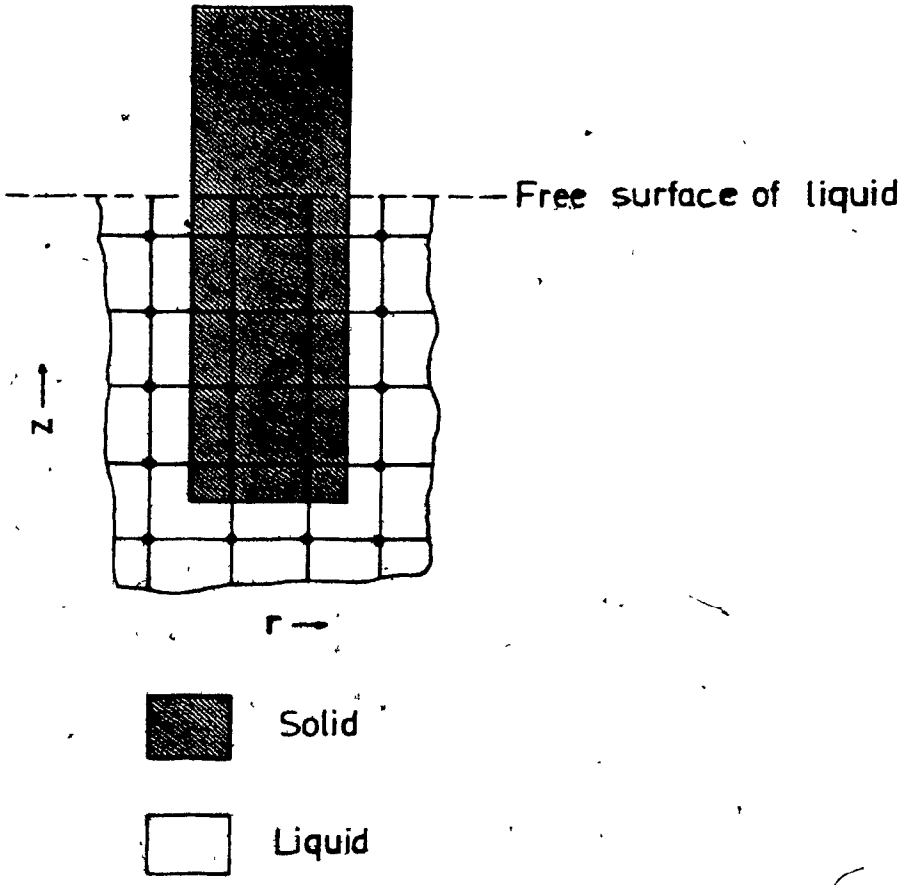

Figure 1.3 Configuration of the central plexiglass cylinder with respect to the finite difference grid illustrating the partially and fully blocked control volumes.

partial differential equation for ϕ, in the form given by equation (1.54).

Depending on the storage locations of the dependant variable, for each of the control volume faces that was cut by the solid refractory cylinder, a blockage ratio or cell porosity was defined. The coefficients of the discretization equation for the node P were calculated in the normal way (designated as A_E^*, A_w^* and so on), and then modified as follows:

$$\begin{aligned} A_E &= (1 - b_E)\, A_E^* \\ A_W &= (1 - b_W)\, A_W^* \\ A_N &= (1 - b_N)\, A_N^* \\ A_S &= (1 - b_S)\, A_S^* \end{aligned} \qquad (1.56)$$

where b's are the blockage ratio (or (1-b)'s are the cell porosity) for the four control volume faces. Evidently these modified coefficients represent the proportion of the area of the control volume face blocked by the solid obstacle.

When all the blockage ratios for a control volume equalled unity, all the neighbour coefficients of the discretization equation became zero and hence the grid node became completely isolated from its neighbours. The value of a variable at such a node could be fixed at any desired value, $\phi_{P,\,desired}$, by redefining the components of the source term as:

$$S_c = 10^{30} * \phi_{P,desired} \text{ and } S_p = -10^{30}$$

With such a prescription, equation (1.53) reduces to

$$-S_p \phi_P = S_c \tag{1.57}$$

or $$\phi_P = -\frac{S_c}{S_p} = \phi_{P,desired} \tag{1.58}$$

Such a technique allowed the value of the dependant variable to be fixed where needed.

In the other procedure (34), the problem was again solved by using a calculation domain that included both the fluid and solid regions. This calculation procedure essentially rests on the ability to handle a large step change in the value of diffusion coefficients (μ_{eff}, Γ_{eff}, μ_{eff}/σ_k, etc.) (in general Γ) through the harmonic mean interpolation technique. When the velocity equations were solved, μ for the grid points that fall in the fluid region was made equal to the viscosity of the fluid, while for the grid points lying in the solid region μ was set equal to a very large number (e.g., 10^{30}). This ensured that the zero velocity specified at the outer surface of the wall prevailed throughout the solid region. By this means the fluid region again experienced the correct boundary conditions in the alternative numerical procedure. The zero velocity condition was specified at the surface of the obstacle through the stan-

dard techniques already mentioned. For solving the scalar transport equations, the Γ field was specified by employing true values in the solid and the liquid regions respectively.

The TEACH-T code and the present computer program

The present computer program represents an extended version of the original TEACH-T computer code for pipe flow problems with,

(i) adaptation to an axisymmetric submerged gas injection system, with baffles, sloping sidewalls, etc.

(ii) incorporation of an unsteady scalar transport equation,

(iii) provision for TDMA traverses in four directions per sweep for improving convergence rates and

(iv) harmonic mean interpolation for diffusion coefficients in u and v momentum equations.

EXPERIMENTAL WORK

Experimental work was carried out in a 0.30 scale water model of a 150 ton teeming ladle. Gas was injected through a central vertical lance into a large cylindrical tank of plexiglass, filled with water, and shown in Fig. 1.4. To simulate the central refractory cylinder, another hollow plexiglass cylinder was placed symmetrically around the bubble plume. Principal dimensions of the model, together with operating parameters are summarised in Table 1.3.

A. Flow Visualisation Studies

Flow visualisation studies were carried out using a suspended gridwork of silken threads. Some of the observed flow patterns are illustrated in Figs. 1.9(c), 1.15(b) and 1.21(c). As seen, these clearly showed the nature of recirculating flows within the ladle. Flow visualisation studies were also carried out by adding potassium permanganate solution to the recirculating bath. These are shown in Fig. 1.5, and also demonstrate the direction of the circulatory loop within the main bulk of the liquid.

B. Flow Measurements with Video-Recorder

Experimental data on velocity fields were obtained on the basis of video recordings of the motion of small rectangular cards (IBM computer punchings, 1 mm x 3 mm x 0.1 mm). These punchings when wet, provided excellent properties and were neutrally buoyant.

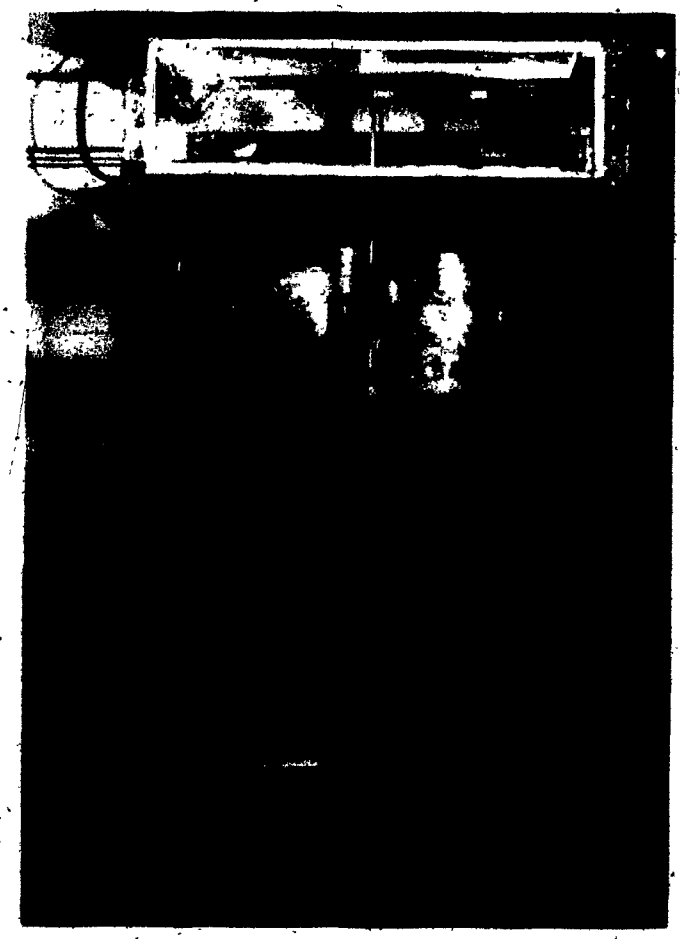

Figure 1.4 Water model showing gas injection through a vertical lance into cylindrical tank of plexi-glass.

Table 1.3 Physical parameters used in full-scale and experimental model in the present investigation

	Full Scale 150 ton ladle	Model 0.30 cylindrical tank of plexiglass
Height, (m, as filled)	3.04	0.93
Diameter, m	3.65	1.12
Nozzle diameter (mm)	20.28	6.35
Refractory cylinder depth, m	0.40	0.12
Refractory cylinder diameter, m	1.26	0.38
Gas flow rate*, m^3/s	1.88×10^{-2}	6.8×10^{-4}
Liquid	steel	water

*Corrected to mean height and temperature of the liquid

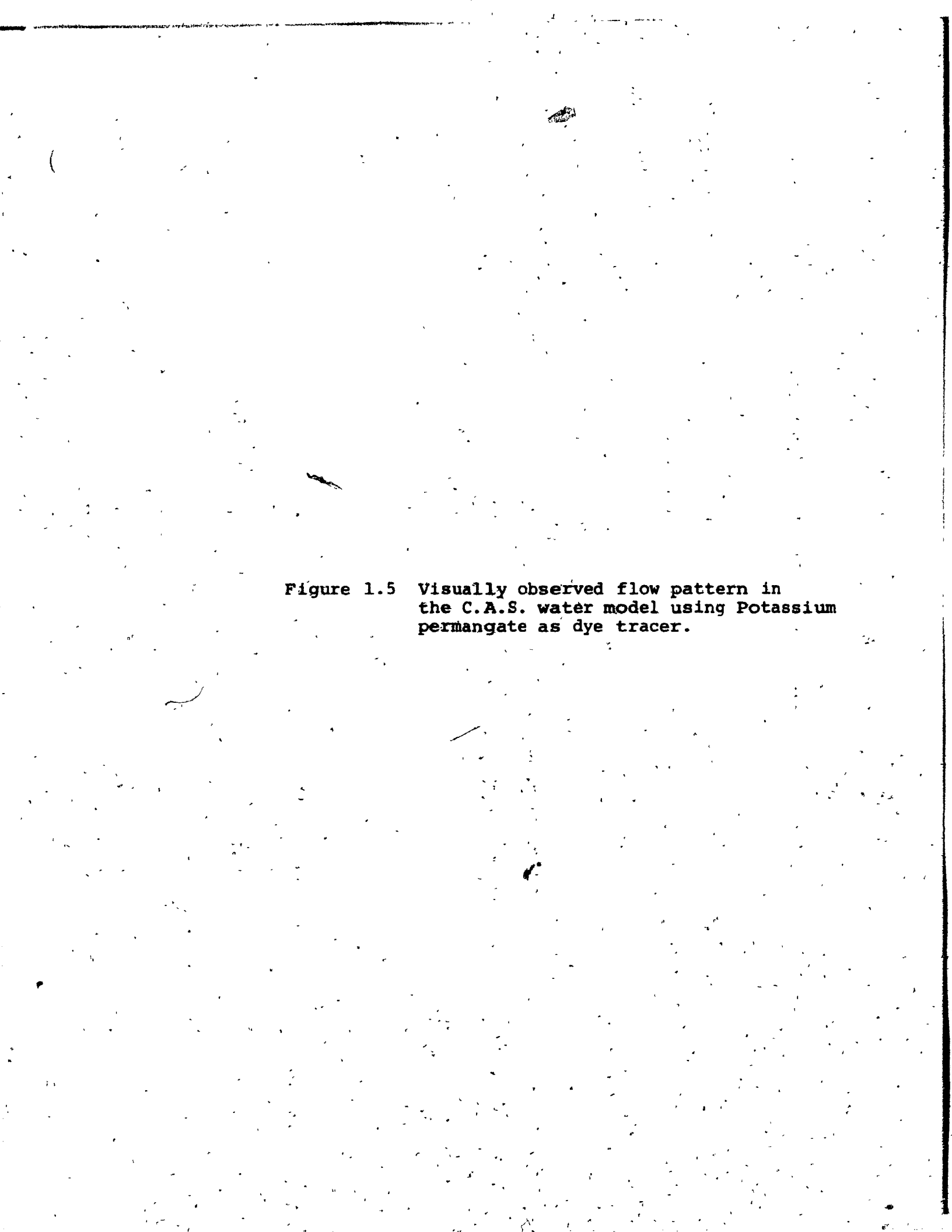

Figure 1.5 Visually observed flow pattern in the C.A.S. water model using Potassium permangate as dye tracer.

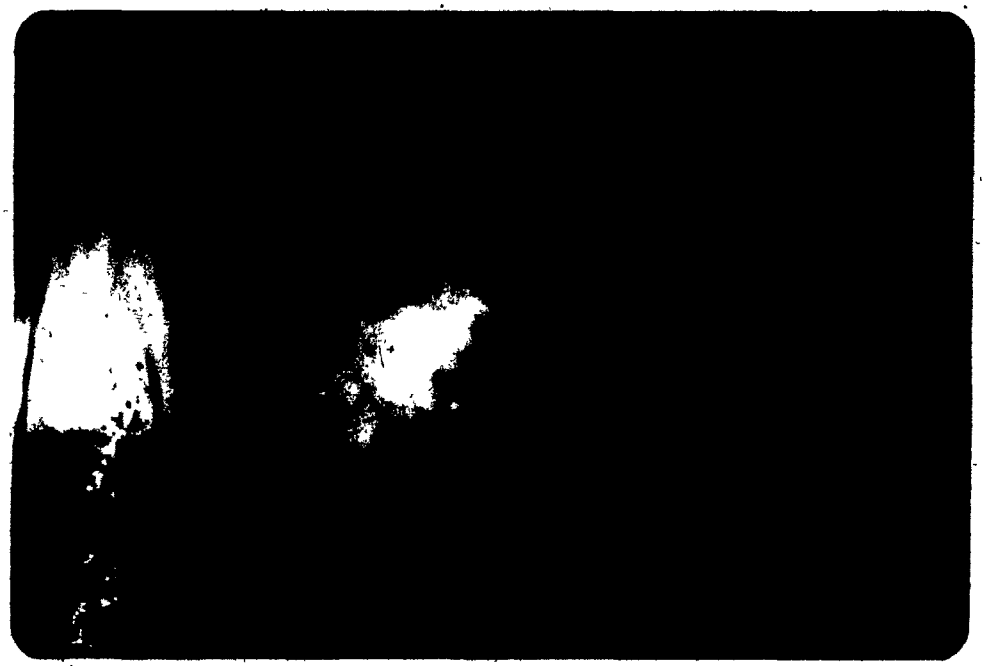

In determining flow fields, a 50 mm x 50 mm grid network was constructed on the front panel of the water model tank. In constructing such a grid network, due care was taken of the parallex effect. A plane light source consisting of a 1500 W quartz lamp between two parallel aluminium plates was used to illuminate the IBM punchings on the central vertical plane of the water model. The trajectories of these cards were then recorded on the video recorder. From frame by frame analysis of the video tape, time, distance and angle of these were measured and from which the velocity components could be estimated and the mean flow pattern within the ladle established. Some typical measurements are reported in Figs. 1.9(a), 1.15(a) and 1.21(a).

C. Flow and Turbulence Kinetic Energy Measurement via Laser Doppler Velocimetry

The experimental set up for velocity measures is shown in Fig. 1.6. As seen, the equipment was a back scatter type L.D.V., employing a 15 mW helium-neon laser. Bursts of laser light, scattered from impurity particles added to the flowing water (10 μm silicon carbide), were collected by the photodetector. This converted the optical signals for processing by a 1900A type counter supplied by Thermo System Inc.. The processed signals were subsequently analysed by means of a microcomputer.

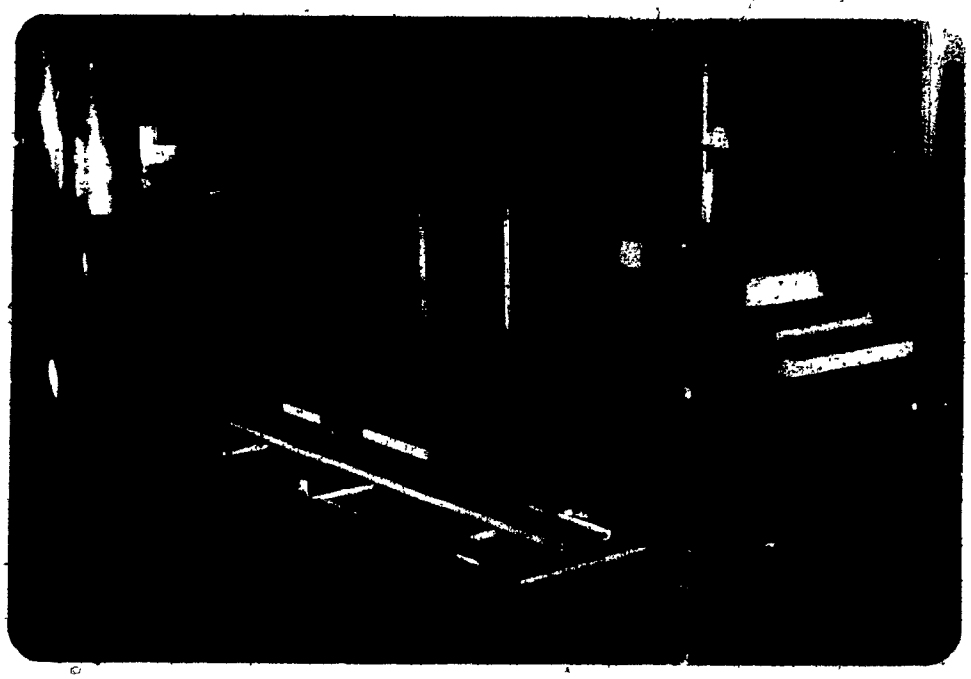

Figure 1.6 The experimental set-up for velocity measurements.

Approximately 1000 data points were collected for each point at a mean rate of approximately 50 per second. The lower limit of detection with the L.D.V. equipment assembled was 10 mm s^{-1}. Mean velocity vectors, and associated turbulence levels were measured at eight different radial positions and at four different axial stations. The maximum variation observed in mean velocity components for successive measurements at a given location was 0-20 mm s^{-1}. To ensure steady state conditions, measurements were only taken some 900 seconds following gas introduction into a quiescent ladle.

Experiments were also carried out in the 0.30 scale water model to study plume geometry as a function of gas flow rate and fractional submergence of lance. Some typical results are shown in Fig. 1.7.

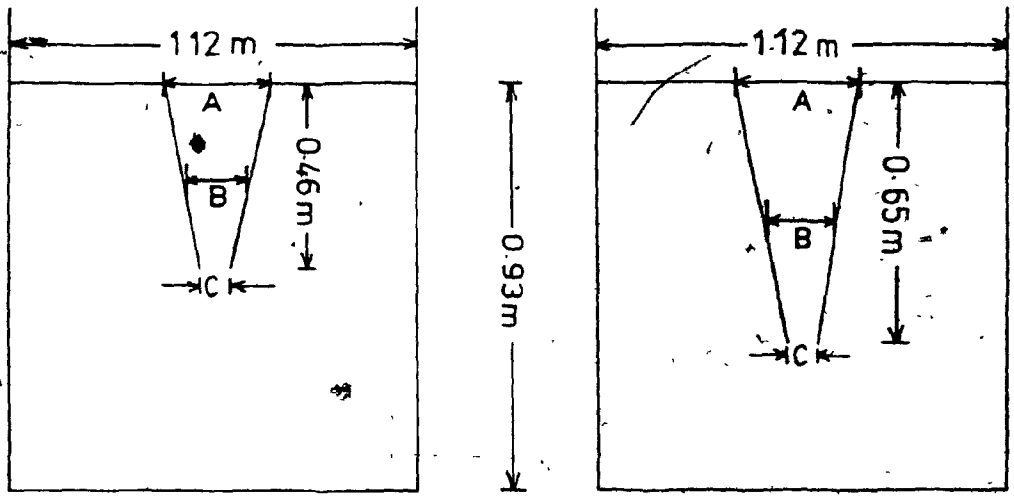

Fractional depth of lance submergence = 0.5

Q. m^3/s	A. mm	B. mm	C. mm
2×10^{-4}	100	70	30
4×10^{-4}	140	94	38
8×10^{-4}	180	110	43

Fractional depth of lance submergence = 0.7

Q. m^3/s	A. mm	B. mm	C. mm
2×10^{-4}	110	72	37
4×10^{-4}	160	95	40
8×10^{-4}	205	130	50

Figure 1.7 Plume geometry as a function of gas flow rate and fractional depth of lance submergence (nozzle diameter = 6.35 mm).

RESULTS AND DISCUSSION

A. Conventional Ladle Stirring

Influence of grid size on model predictions

The influence of grid size distribution upon model performance has been illustrated in Fig. 1.8. This shows how the model predictions for vertical velocity component vary for a variety of grid configurations. It was found that increasing the number of grids beyond 18 x 15 produces no significant difference in the nature of model predictions. In testing a 25 x 23 grid, results were essentially identical to that for the 18 x 15 grid, indicating that the latter produces results which are effectively independent of nodal configuration.

Comparison between measured and predicted flows

It was found that flows generated in the 0.3 scale water model at 50 pct lance submersion were practically identical to those generated by gas entering at the base of the model ladle. The flow fields as depicted by Fig. 1.9(a) clearly show a recirculating vortex located high in the ladle and displaced toward the outside wall. Predicted results based on the numerical solution of governing differential equations are presented in Fig. 1.9(b). These exhibit close geometric similarity with measured flow fields. The quantitative nature in the agreement between the measured and predicted flow fields is illustrated in Fig. 1.10, where the vertical components of the flow at various depths in the water model are compared. As seen, the

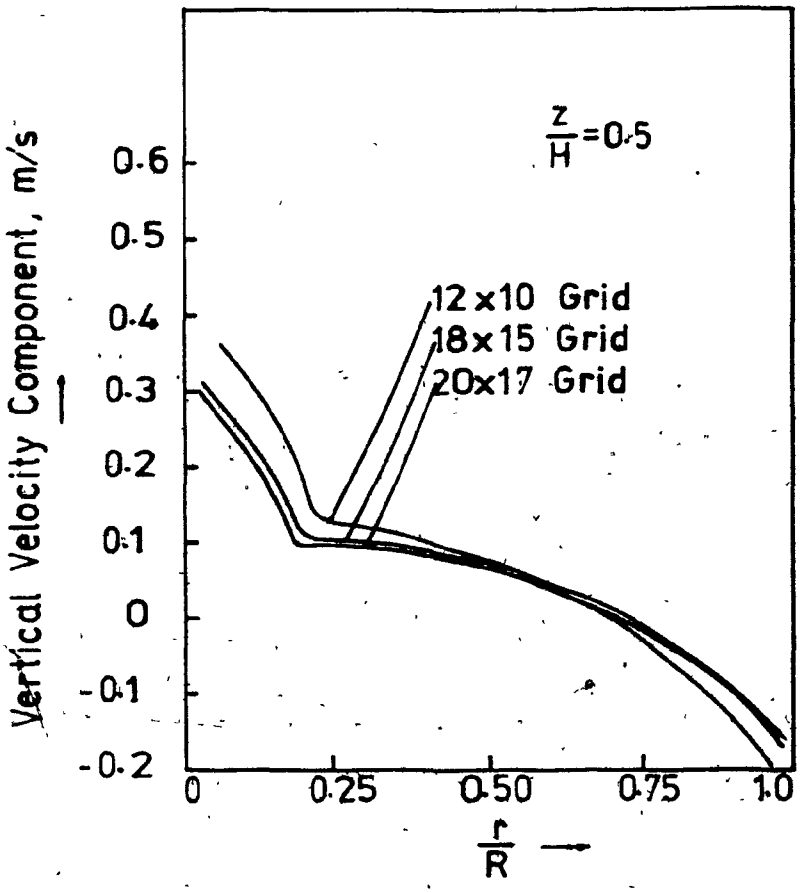

Figure 1.8 The influence of grid configurations upon model prediction.

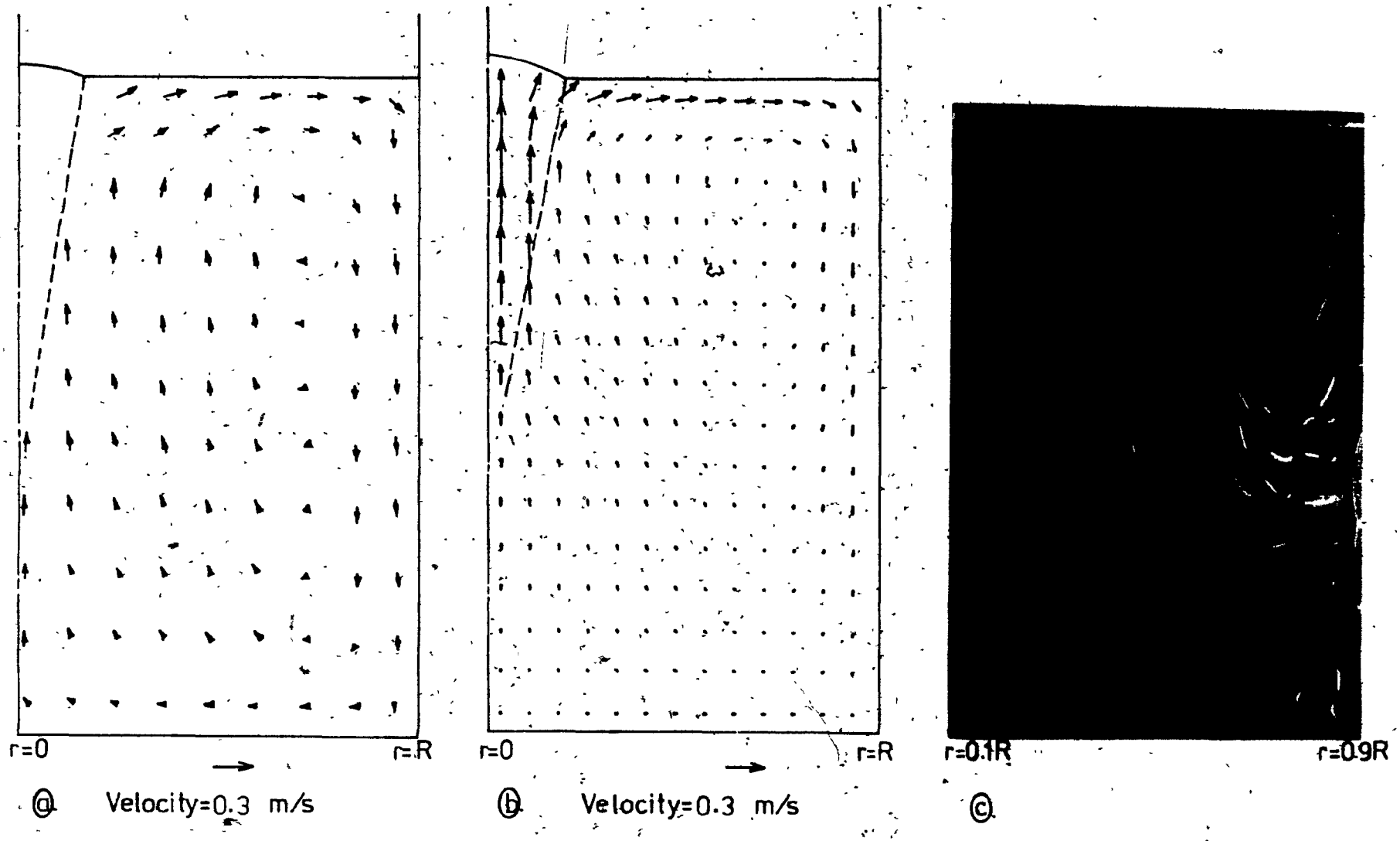

Figure 1.9 (a) Experimentally measured velocity field (m/s) in the water model. Tank diameter = 1.12 m, liquid depth = 0.93 m, gas flow rate = $6.8 \times 10^{-4} m^3/s$, and fractional depth of lance submergence = 0.5. (b) Theoretically predicted velocity field (m/s) in the water model of dimensions and gas flow rate given in (a). (c) Observed flow fields with a suspended grid work of silken threads.

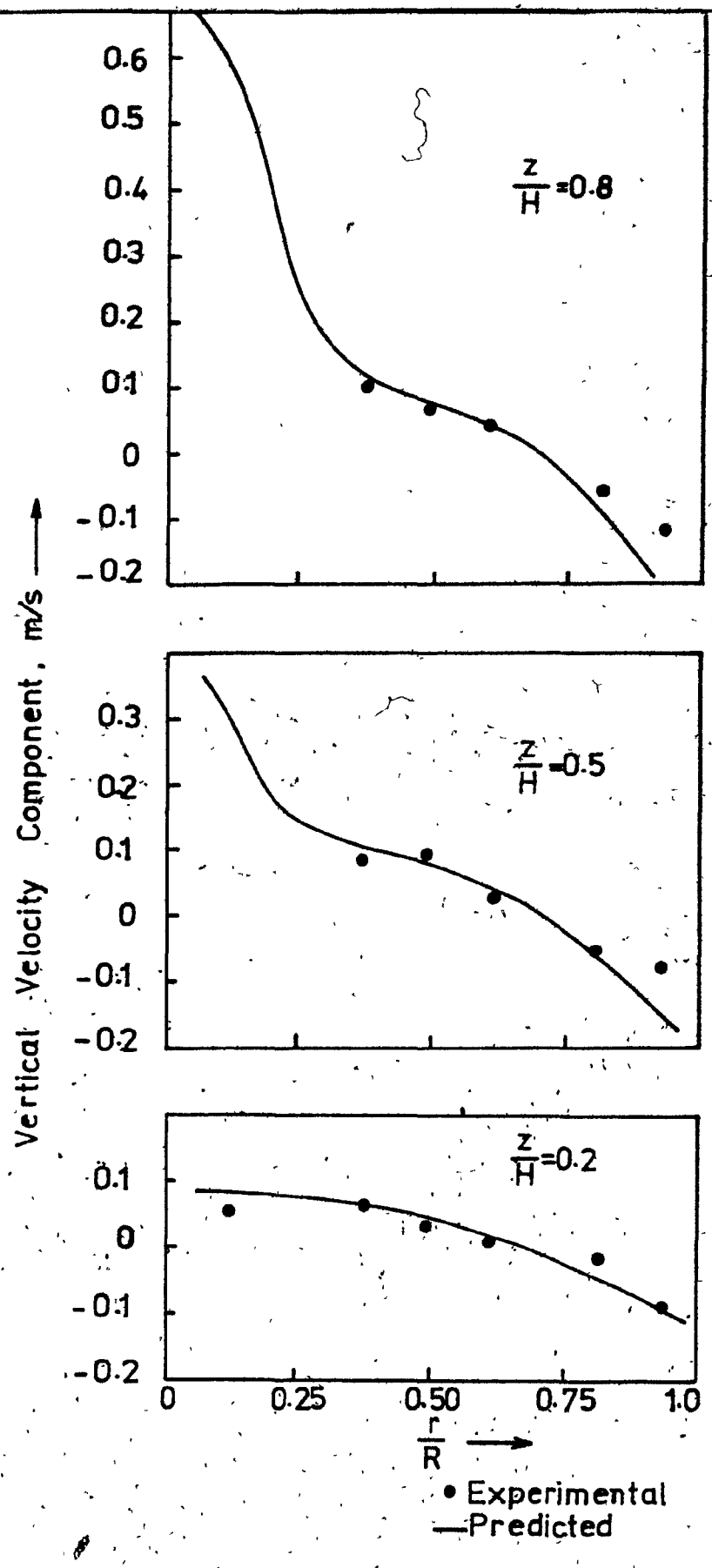

Figure 1.10. Comparison of experimentally measured and theoretically predicted vertical velocity component at different depths in water model for 50 pct lance submersion (L = 0.93 m, R = 0.56 m, Q = 6.8 x 10^{-4} m^3/s).

reasonable agreement between the measured and predicted flow field is at once evident, with relative deviations of less than 20 pct everywhere. It is to be mentioned here that the discrete data points in Fig.1.10 were obtained on the basis of video recording of the flow.

Influence of effective viscosity models on model predictions

Figure 1.11 shows the predicted distribution of vertical velocity components in the water model, using two alternative models for effective viscosity (i.e., the k-ε model and an algebraic, bulk effective viscosity model). It is seen that the agreement between the flow fields, using either of these two models, is excellent and indicative of the fact that inertial forces predominate in such systems. It is also instructive to note that the ratio between the volumetric average bulk effective viscosity predicted by the k-ε turbulence model and equation (1.39) is approximately 1.20 (i.e., 0.95: 0.78).

Plume dimensions in the water model and the sensitivity of flow prediction to plume dimensions

Plume dimensions and geometry are not, in reality, as precise as those suggested in Fig. 1.7. There the results have been presented in terms of an idealized plume, that is, conical in shape, and has a uniform distribution of gas voidage. In reality, the two phase regions are discontinuous and turbulent, and any 'interface' between the plume and the bulk of the liquid can only be drawn imprecisely. The uncertainty associ-

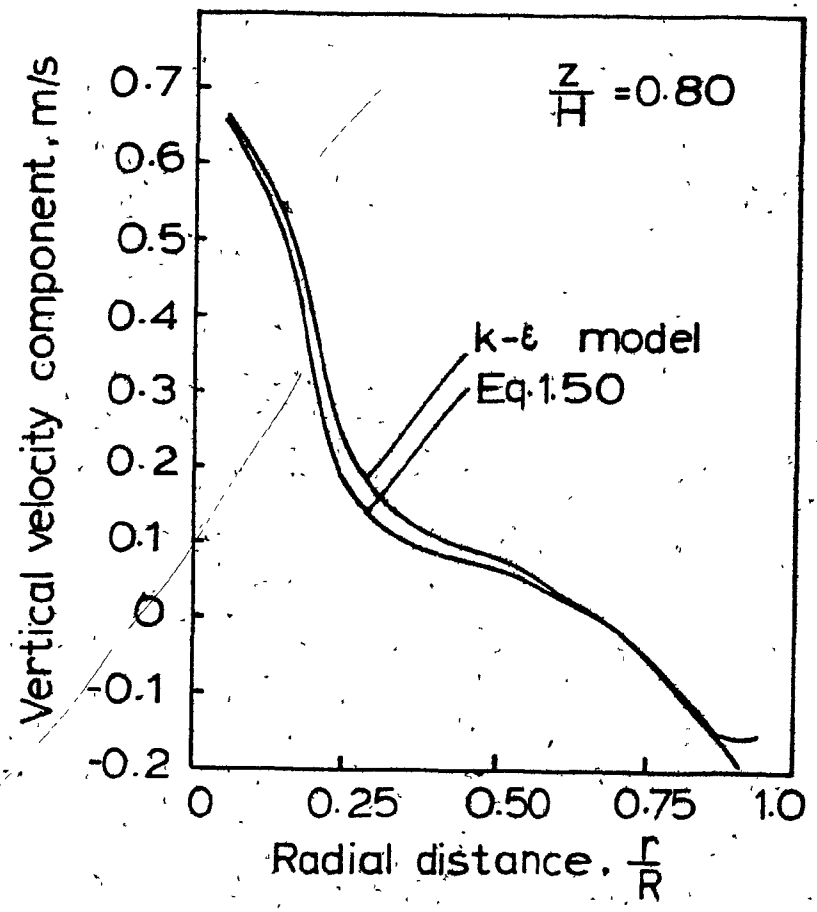

Figure 1.11 Comparison of theoretically predicted velocity component in water model, using two alternative models of effective viscosity. ($L \equiv 0.93$ m, $R = 0.56$ m, $Q = 6.80 * 10^{-4} m^3/s$ and $\beta = 0.5$).

ated with the discontinuous nature of the plume would pose almost insuperable difficulties in any precise modelling of such gas stirred systems. Fortunately, by idealizing the actual situation in the way presently suggested, it is possible to model such buoyancy driven flows with some confidence.

With regard to the volume fraction, or voidage, α, of gas within the two phase region, the value incorporated in the mathematical model is calculated according to equation (1.53), and corresponds to the value of α referred to the mean plume height. Significant variations in the density of the gas liquid mixture can be expected along the axial direction of the plume, however. Assuming a Gaussian velocity distribution in the two phase region(37,38), and equating the mass flux of gas at two different but arbitrary axial coordinates, z_1 and z_2, it can be shown that the axial distribution of α can be expressed through

$$\frac{\alpha_{z_1}}{\alpha_{z_2}} = \frac{\rho_{g,z_2}\left|1 - \exp(-\frac{r_2^2}{b^2})\right|}{\rho_{g,z_1}\left|1 - \exp(-\frac{r_1^2}{b^2})\right|} \qquad (1.59)$$

where $b^2 = 2c^2 (z + h_o)^2$

In the present theoretical treatment, the linear rate of spread of the two phase region, c, and h_o, the height above the

analytic origin needs to be determined experimentally. The constant, c, is affected by gas flow rate, vessel radius, and liquid depth, while h_o, as one can anticipate, varies predominantly with fractional depth of lance submergence. Taking the present experimental results for $\beta = 0.50$ in Fig. 1.9(a) as a typical example, the angle of jet spread, $2\phi_o$, was 0.384 rad, while the virtual origin was 140 mm below the nozzle exit for $z_o = 0.46$ m and $Q = 6.8 \times 10^{-4}$ m^3/s. The value of α at 1/10 and 7/10 of βL were therefore 11 pct and 8 pct, respectively.

As a final note, bulk flow fields are relatively insensitive to the precise geometry of the bubble plume. For equivalent gas flows, a 50 pct. wider plume with an appropriately reduced voidage will generate an essentially similar flow within the bulk of the ladle as seen in Fig. 1.12. Nevertheless, the width of the surfacing plume can be of significant practical interest and significance.

B. The C.A.S. Method

Numerical computation of flow

Predicted flow fields for a typical gas flow rate of 6.80×10^{-4} m^3/s (e.g., 40.8 l/min) in the water model are shown in Figs. 1.13 and 1.14 respectively. Comparison between k-ε predictions in Fig. 1.13 and observations jointly shown in Fig. 1.15(a) and 1.15(b), respectively clearly demonstrate that computations based on the standard two equation model produced a very different flow field to that actually observed. Re-

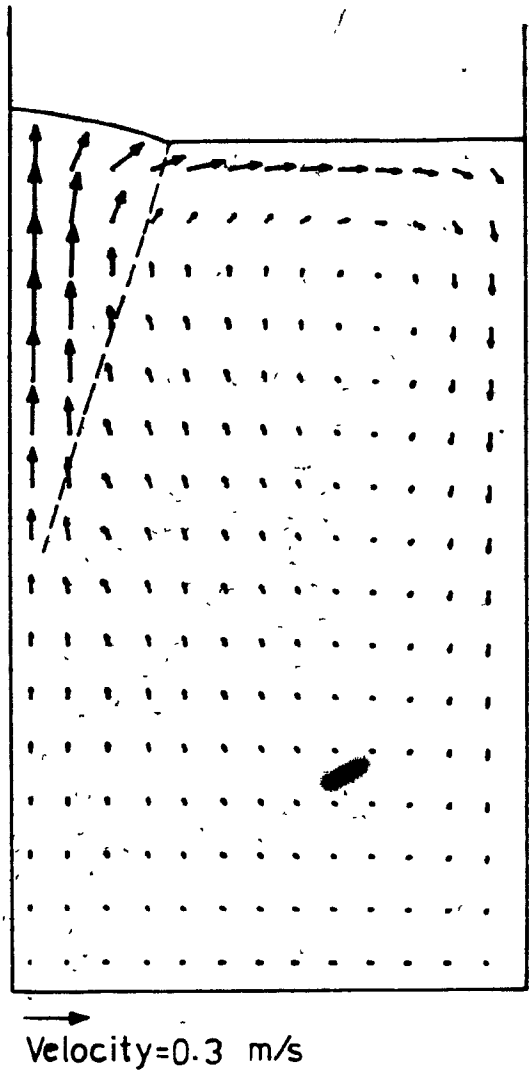

Figure 1.12 Predicted velocity field (m/s) in water model for an assumed 50 pct wider plume than in fig. 1.9(a).

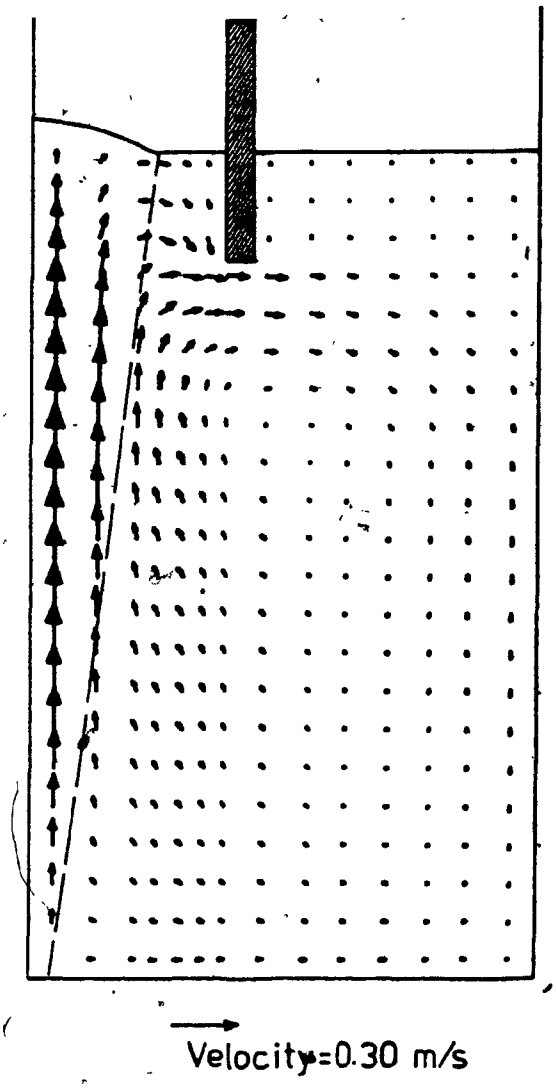

Figure 1.13 Predicted velocity field (m/s) in the water model (L = 0.93 m, R = 0.56 m) at a gas flow rate of 6.8 x $10^{-4}m^3/s$, using the k-ε model with standard values of the empirical constants (viz., Table 1.2).

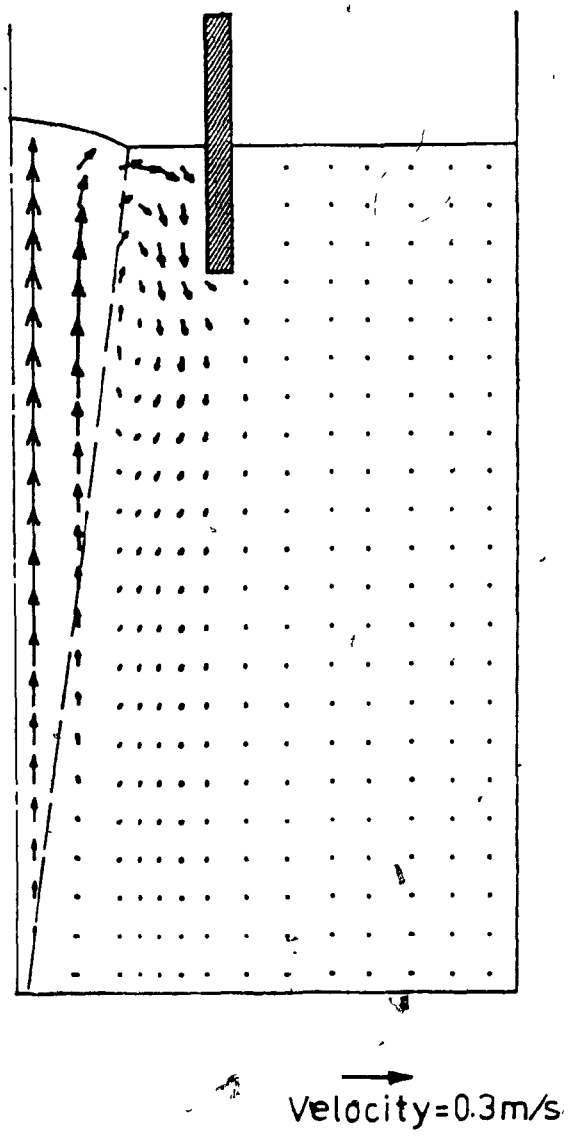

Figure 1.14 Predicted velocity field (m/s) in the water model for the same operating condition as those in Fig. 1.13, using the bulk-effective viscosity formula (viz., Equation (1.39)).

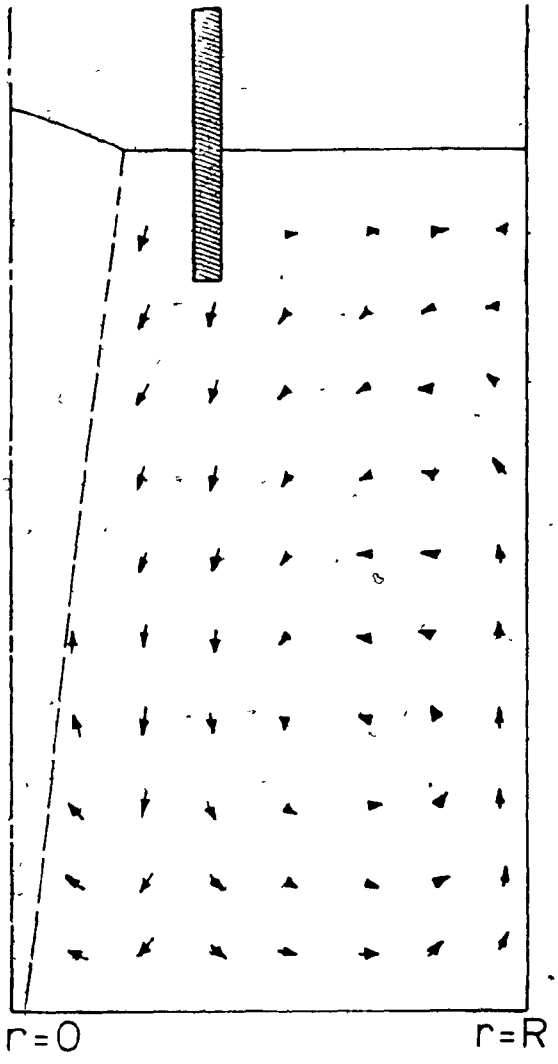

Figure 1.15(a) Experimentally measured velocity field (m/s) in water model using the video recording technique (liquid depth = 0.93 m, vessel radius = 0.56 m, gas flow rate = 6.8 x $10^{-4}m^3/s$, inner radius of plexiglass cylinder = 0.19 m, plexiglass cylinder immersion depth = 0.12 m).

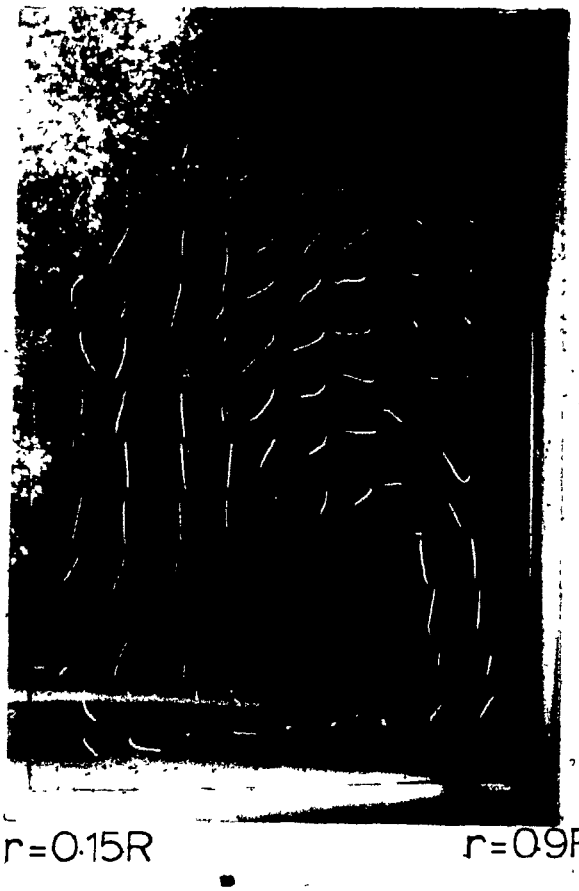

Figure 1.15(b) Visually observed flow field in the water model for the same conditions as those in Fig. 1.15(a), using a suspended network of silken threads

ferring to Fig. 1.14, which shows equivalent computations using the bulk effective viscosity formula for gas stirred liquids, it is seen that very realistic predictions were achieved. As seen, the strong recirculatory flow beneath the cylindrical baffle, together with a much slower anti-clockwise vortex in the main bulk of the ladle were properly predicted.

Analysis for failure of k-ε turbulence model

The inadequacy of the k-ε turbulence model, when using the standard set of constants, posed a serious problem to further numerical studies on mixing, heat transfer and particle motion.

Examples cited in the literature (1-3) have already shown that the k-ε turbulence model with standard constants, can predict recirculating flows in ladles with an accuracy that is sufficient for most purposes. However, the turbulence model is based on a number of simplifying assumptions and these are known to fail for various systems. These include axisymmetric jets issuing into stagnant surroundings, far field jets and wakes, where the generation and dissipation of turbulence are not in balance, etc.

The k-ε model is based on a number of assumptions:

i) the eddy viscosity hypothesis, i.e., $\tau = \rho\nu_T \frac{\partial u}{\partial y}$

ii) isotropic turbulence,

iii) a gradient formulation for turbulent fluxes, and

iv) a local balance between production and dissipation of turbulence energy,

together with five empirical constants noted in Table 1.2. These were obtained on the basis of simple shear flows, decay of turbulence behind grids, etc.

In seeking reasons for the failure of the k-ε model, the possibility of enhanced turbulence in the vertical direction of the rising plume was considered. However, for the present case, the magnitude of the inlet densimetric Froude Number ($Fr = U_o/\sqrt{gr_o(\rho_L-\rho_G)/\rho_L}$) was estimated to be 50, indicating buoyancy effects on the k and ε equation should be negligible.

Part of the explanation may rest with assumption (i) of the k-ε model. This breaks down across the shear layer between liquid in the rising plume and the bulk liquid flowing downwards; there the velocity gradient within an annular region around the plume reduces to zero in a region of high turbulence. Evidently, the transport of turbulent motions across this layer must generate non-zero shear stresses. It is important to note that the simple algebraic model did not run into such difficulties.

Figure 1.16 shows predicted distributions of turbulence energy dissipation (at z=0.8H) for the two numerical approaches just described. One sees that the algebraic model (curve 1) adopts an energy dissipation rate equal to the rate of potential energy input (viz., 7×10^{-3} m^2 s^{-3}) whereas the k-ε model with standard constants, predicts much higher dissipation rates. Fig. 1.17 gives associated turbulence viscosities. There, the

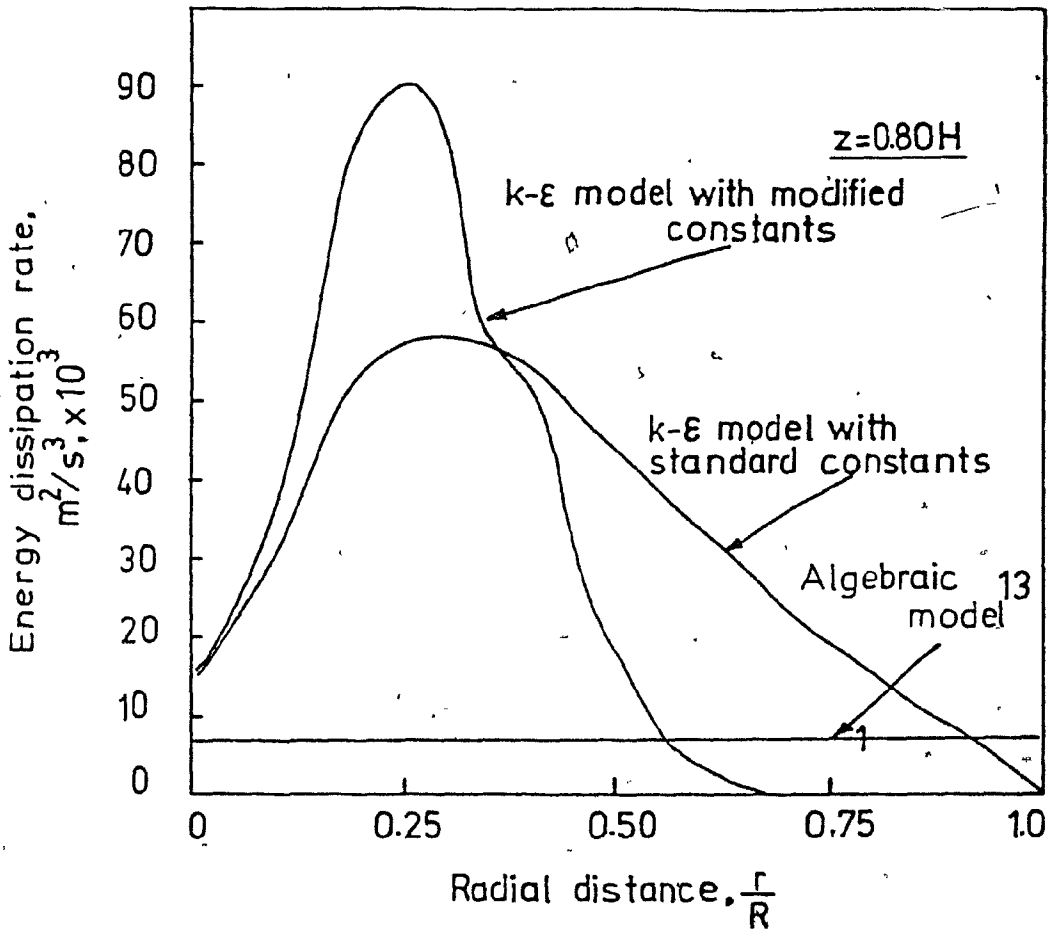

Figure 1.16 Predicted change in the turbulence kinetic energy dissipation rate (m^2/s^3) versus radius at Z/H = 0.80 for the conditions given in Fig. 1.15(a).

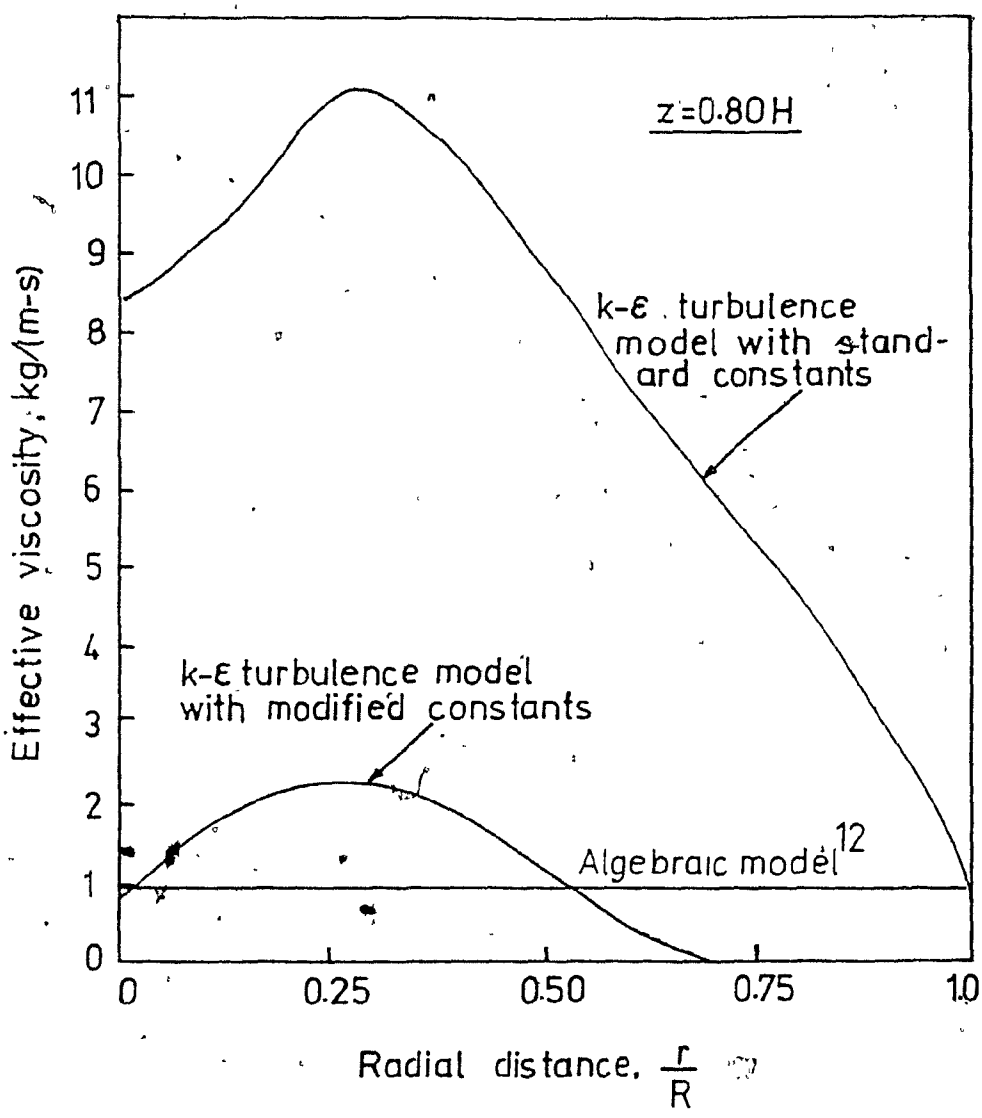

Figure 1.17 Predicted radial variation of effective viscosity (kg/(m-s)) at Z/H = 0.80 for the conditions given in Fig. 1.15(a).

two equation values of 1-11 kg m^{-1} s^{-1} run up to ten times higher than those of the algebraic model (viz., 1 kg m^{-1} s^{-1}). However, on increasing the bulk turbulence viscosity to 16 kg m^{-1} s^{-1}, the highest local value for the standard k-ε procedure, and re-running the program with a constant effective viscosity, an equivalently incorrect flowfield to that presented in Fig. 1.13 was produced (i.e., a single recirculating vortex).

Comparison between measurements and prediction of flow and turbulence kinetic energy

The predicted flow field using the modified values of the empirical constants (viz., Table 1.4) is presented in Fig. 1.18 together with corresponding ε and μ_{eff} curves in Figs. 1.16 and 1.17. One can observe that these exhibit close geometric similarity with measured flow fields, while providing a much more complete description of the flow.

For the purposes of quantitative comparison, the mean vertical velocity components of the flow at four different axial heights were compared with mean Laser Doppler measurements. Excellent agreement between measurements and predictions were achieved as illustrated in Fig. 1.19. Based on discrete L.D.A. data, radial distributions of turbulence kinetic energy per unit mass (i.e. k) at four axial stations were measured. These are compared directly against predictions in Fig. 1.20. Again very reasonable agreement between the two is indicated.

Table 1.4 The values of the empirical constants in k−ε turbulence model, used for predicting flows in C.A.S. procedure

C_1	C_2	C_D	σ_k	σ_ε
1.58	1.75	0.09	1.0	1.3

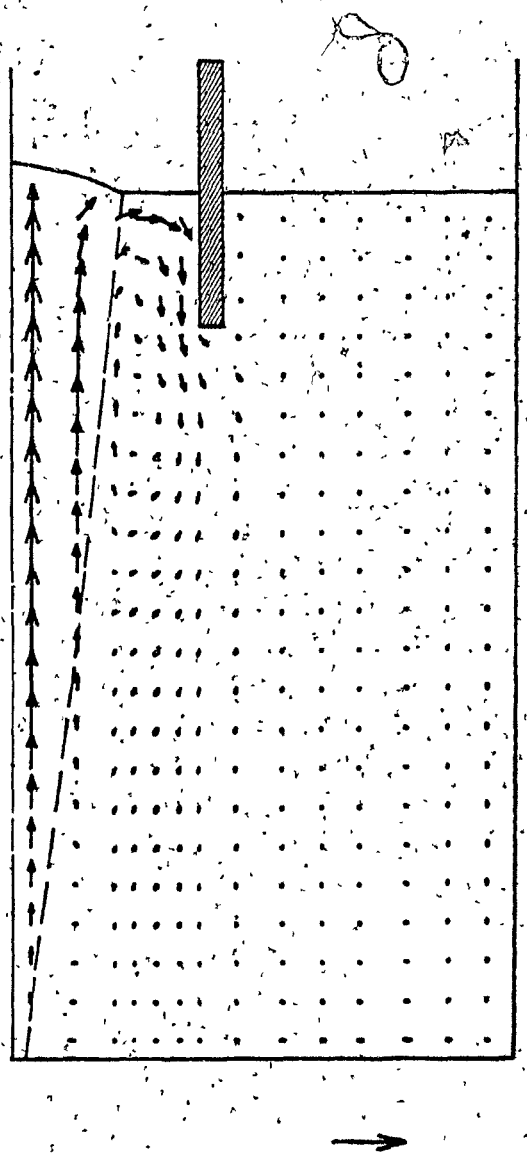

Figure 1.18 Predicted velocity field (m/s) in the water model using the k-ε model with constants and their values shown in Table 1.4.

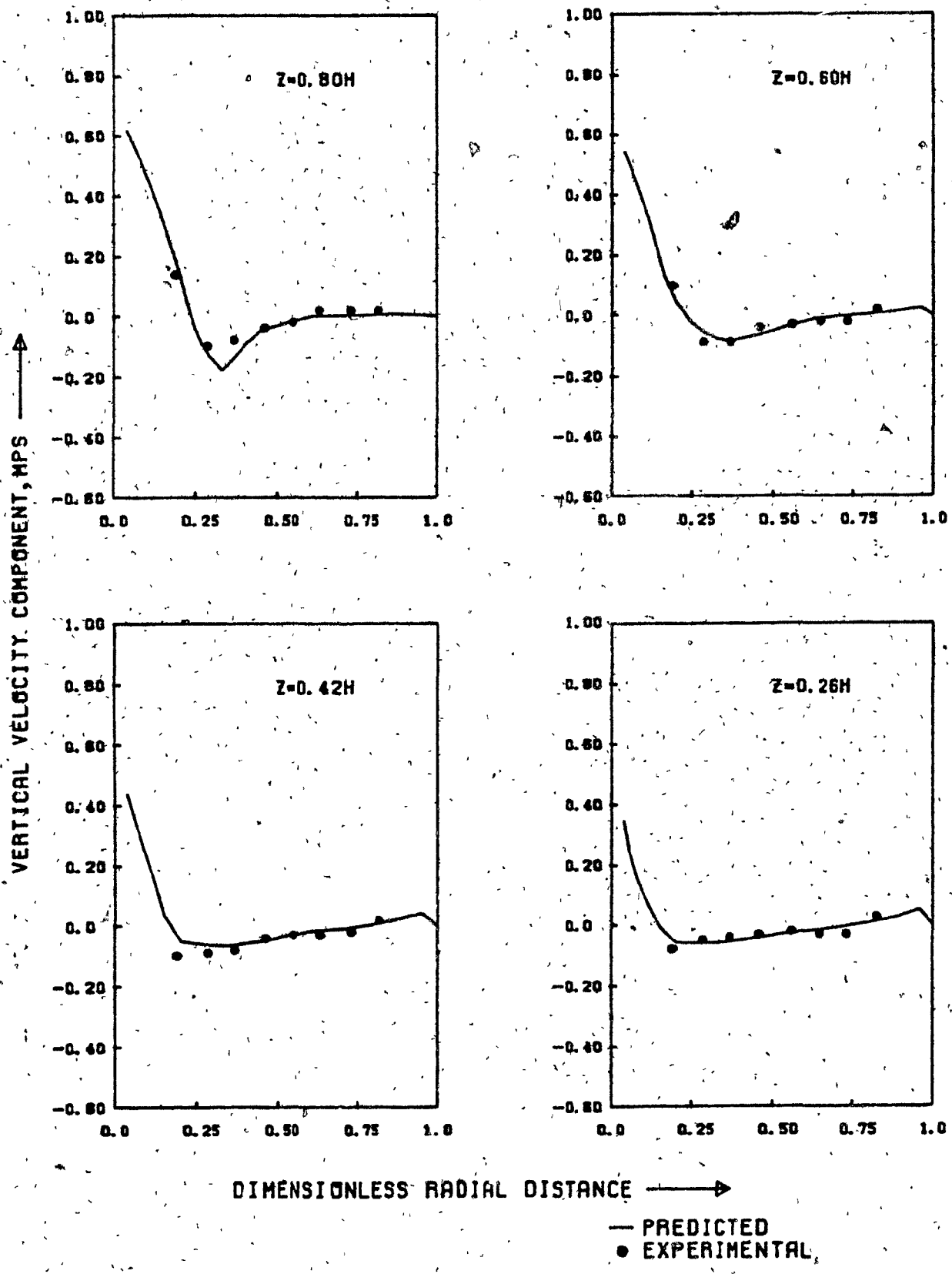

Figure 1.19 Comparison of theoretically predicted and experimentally measured vertical velocity component at four different depths in the water model for the conditions given in Fig. 1.15(a). (Constants from Table 1.4 were used for prediction.)

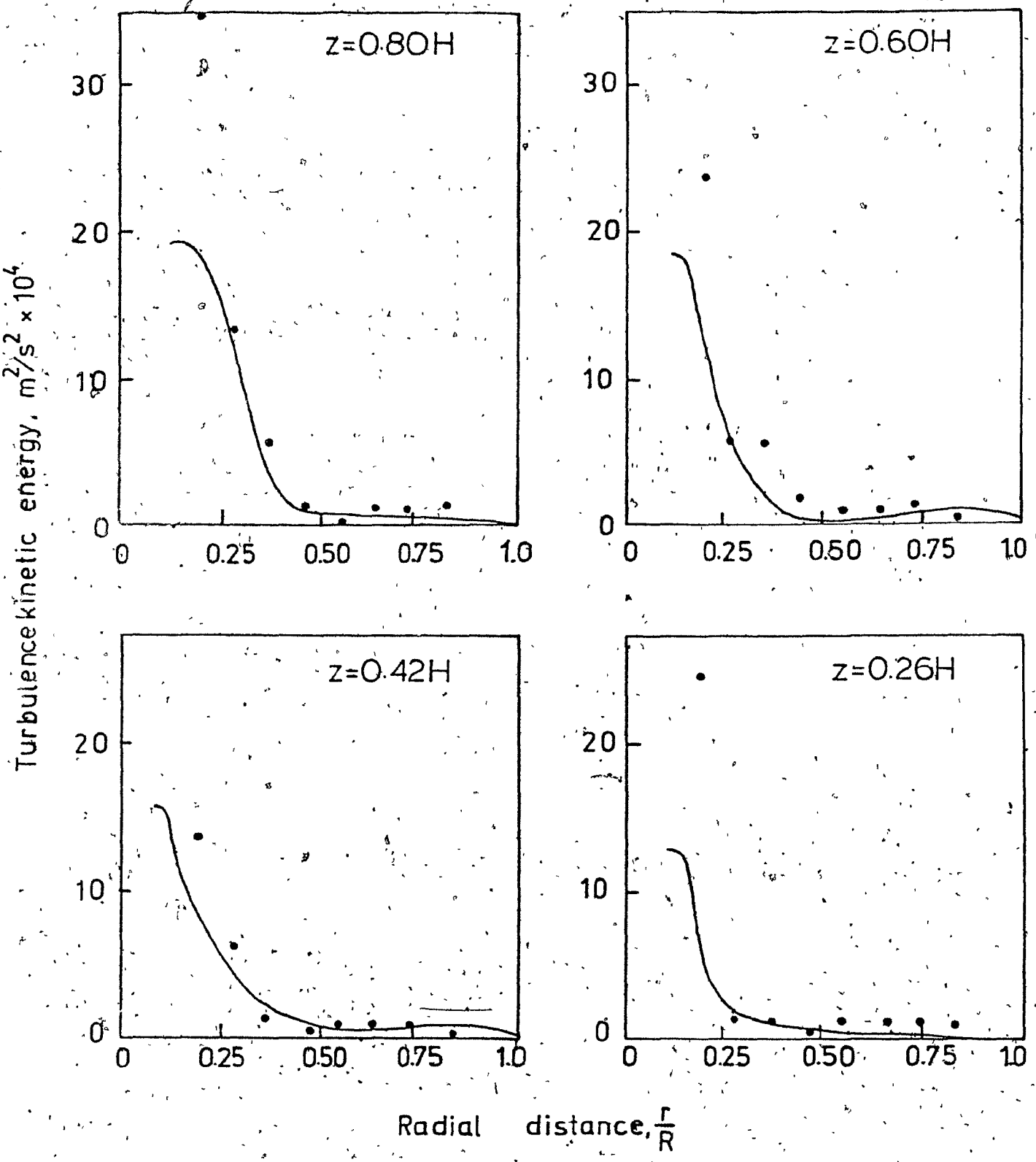

Figure 1.20 Comparison of theoretically predicted, and experimentall measured, turbulence kinetic energy (m^2/s^2) at four different depths in the water model for the conditions given in Fig. 1.15(a). (Constants from Table 1.4 were used for prediction.)

Flow at half lance submersion: Numerically predicted flow and turbulence kinetic energy distribution and their comparison with measurements

Predicted velocity fields for 50 pct. lance submersion shown in Fig. 1.21(b) again reveal the two vortices that are characteristic of the C.A.S. system. The model predictions for vertical components of the flow have been compared with laser doppler measurements in Fig. 1.22, while predicted and measured turbulence kinetic energy distributions in the water model are compared in Fig. 1.23. Good agreement between measurements and predictions is again apparent. It is to be noted here that the depth of the circulatory loop associated with the bubble plume shrinks in accordance with the extent of lance immersion.

Sensitivity of flow prediction to plume dimensions

Computations presented so far are based on the concept of an idealised plume, taken to be conical in shape with a uniform distribution of gas voidage. In reality, the structure of the plume is complex and the complexity is further aggravated in the present case by a downcoming stream of liquid adjacent to the plume. This downflow actually entrains a significant amount of gas from the upwelling gas-liquid mixture near to the free surface of the liquid. Consequently, it becomes extremely difficult to draw any precise line of demarcation between the bubble plume and the liquid, particularly in the vicinity of the free surface. Nevertheless, it is useful to note that bulk

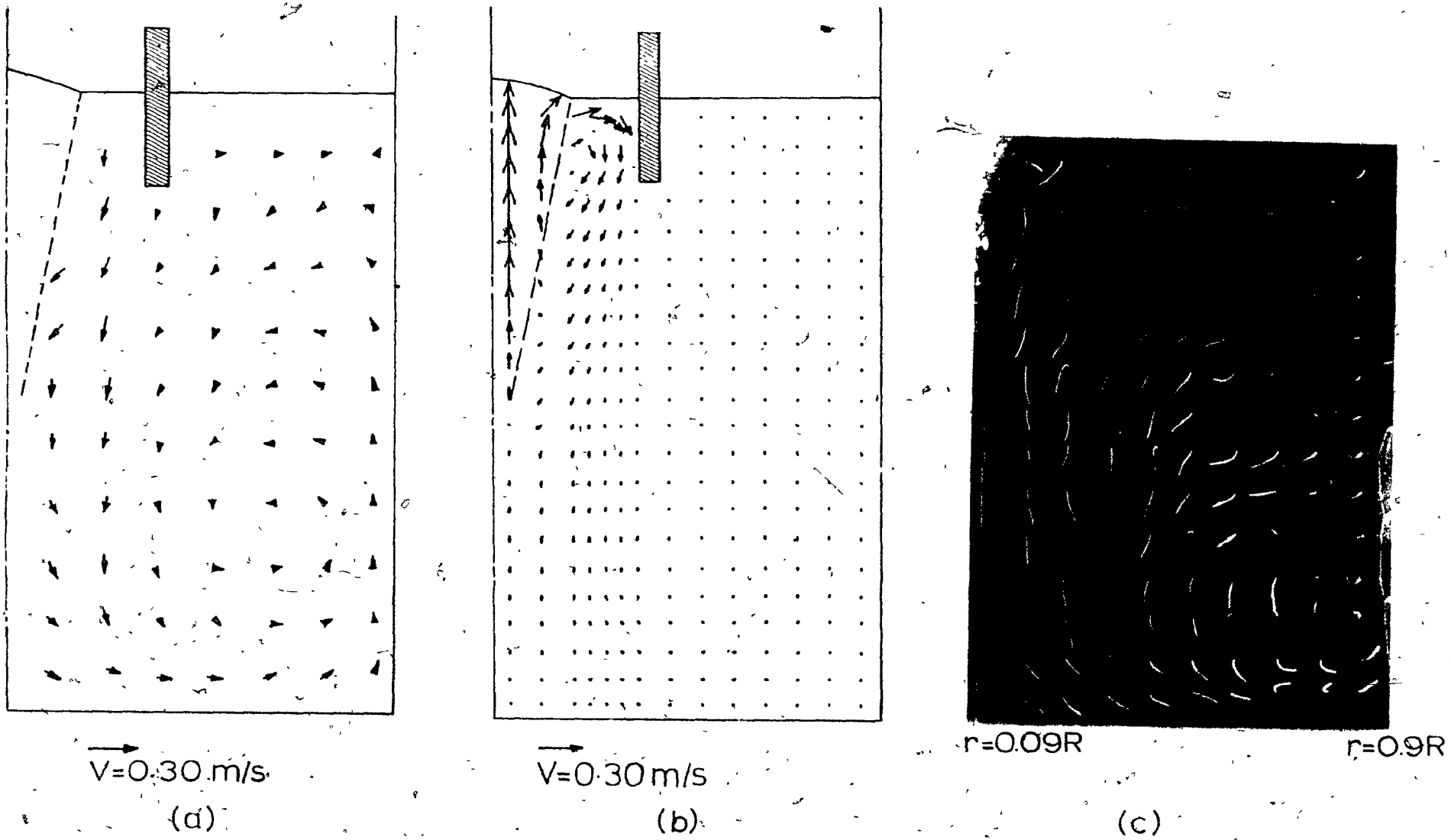

Figure 1.21 (a) Experimentally measured velocity field (m/s) in the water model (tank diameter = 1.12 m, liquid depth = 0.93 m, gas flow rate = $6.8 \times 10^{-4} m^3/s$, fractional depth of lance submergence = 0.5, inner radius of plexiglass cylinder = 0.19 m and plexiglass cylinder immersion depth = 0.12 m). (b) Theoretically predicted velocity field (m/s) in the water model of dimensions and gas flow rates given in (a). (c) Observed flow fields with a suspended gridwork of silken threads. (Computations in Fig. 1.21 (b) were based on the values of the constants given in Table 1.4.)

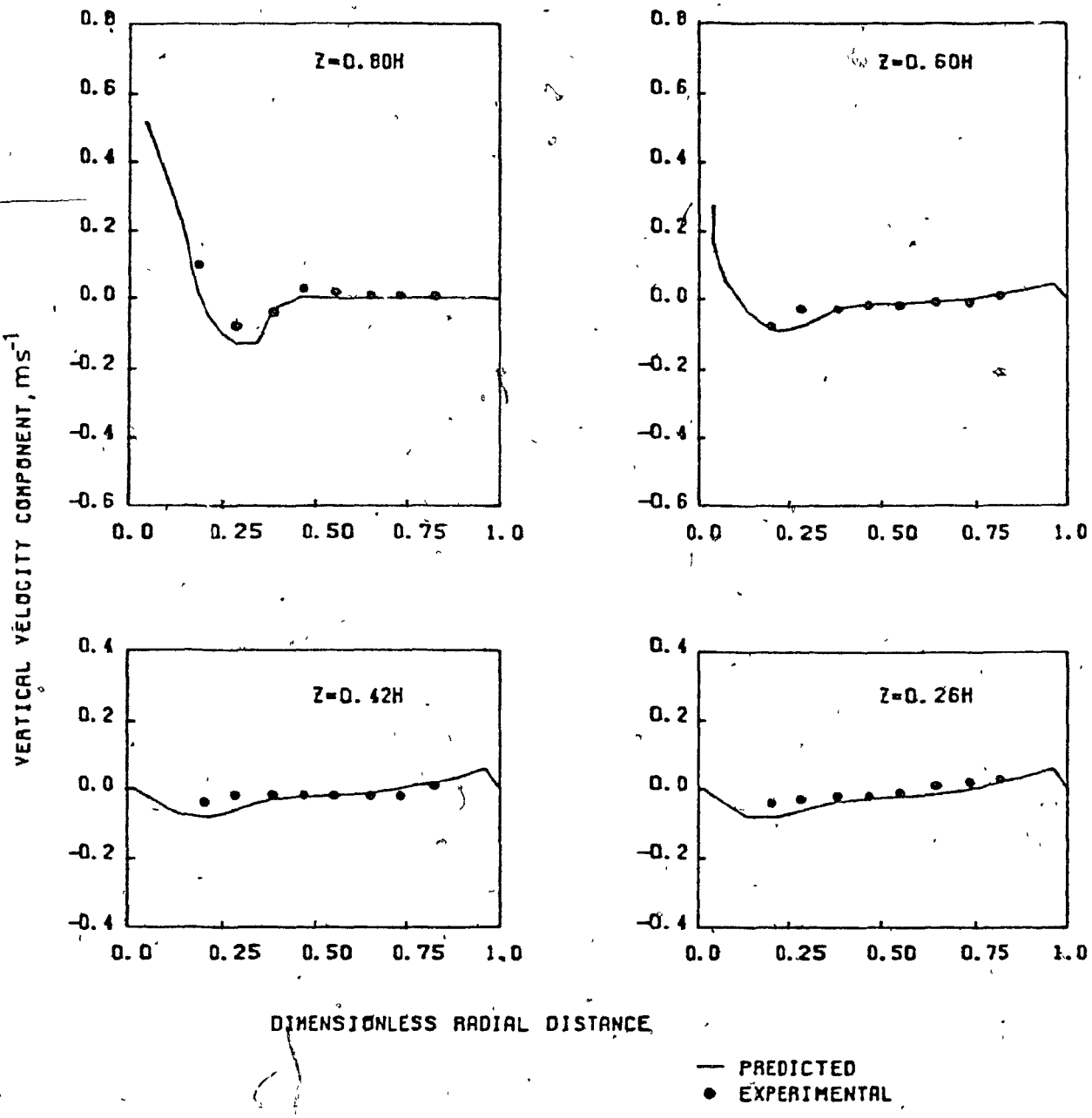

Figure 1.22 Comparison of experimentally measured and theoretically predicted vertical velocity component at different depths in water model for the conditions given in Fig. 1.21(a). (Constants from Table 1.4 were employed for numerical computation.)

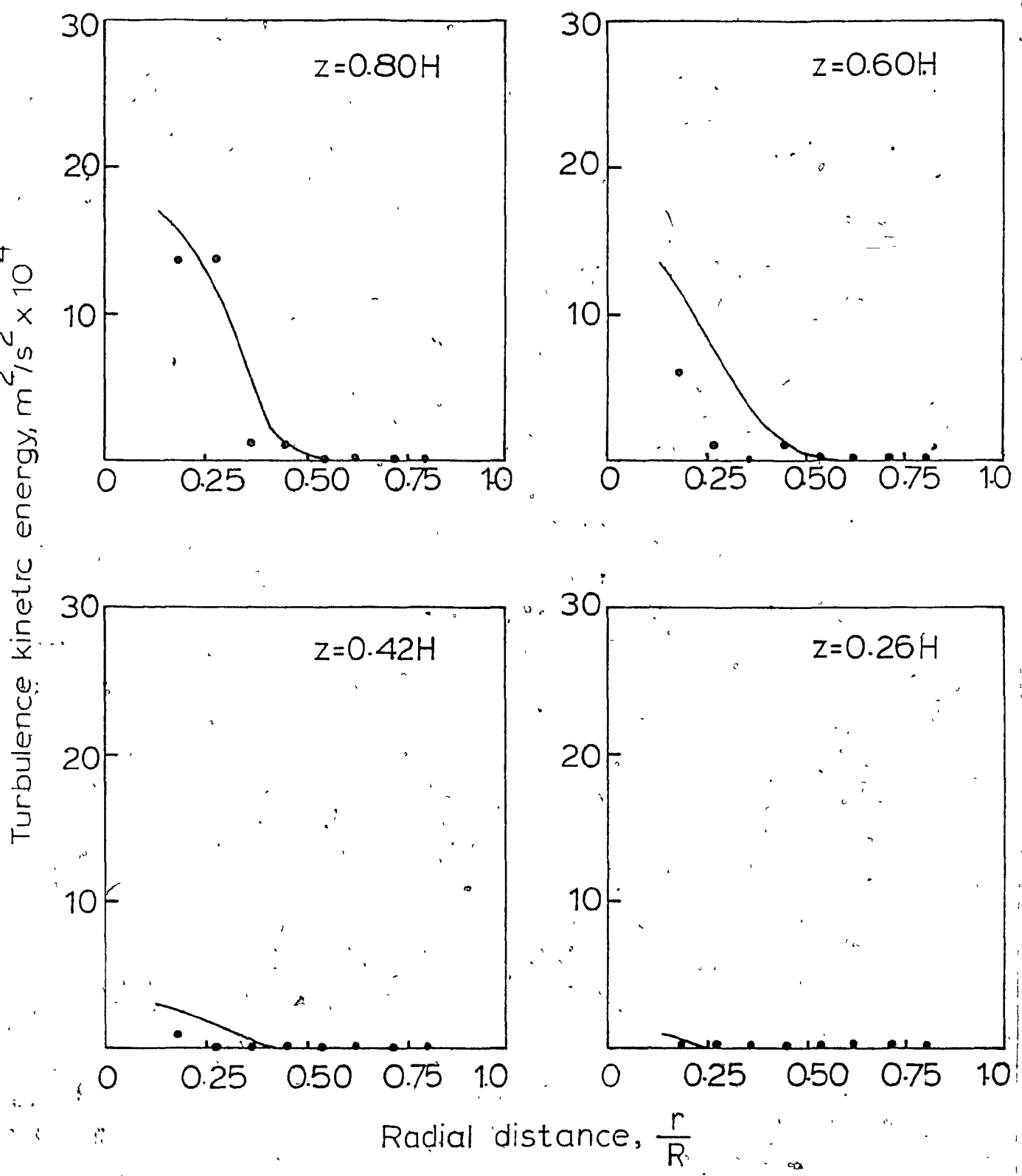

Figure 1.23 Comparison of experimentally measured and theoretically predicted turbulence kinetic energy (m^2/s^2) at four different depths in water model for the conditions given in Fig. 1.21(a). (Constants from Table 1.4 were employed for numerical computation.)

flow fields are relatively insensitive to the precise geometry of the plume. For example, at an equivalent gas flow, a 25 pct. wider plume with an appropriately reduced voidage, will generate an essentially similar flow within the ladle. This is seen from Fig. 1.24. Furthermore, predicted mean speeds of liquid recirculation are also very similar (i.e., 0.0397 m s^{-1}: 0.037 m s^{-1}). If however, the plume diameter is arbitrarily increased, so that a part of the plume is exposed outside the plexiglass cylinder, the resultant flow field can be drastically changed from that presented in Fig. 1.18.

Predicted distribution of effective viscosity in the water model

The use of a differential model of turbulence also clearly shows the variation in different turbulence quantities (i.e., k,μ_e,u'/u, etc.) within the system, which evidently is not available via an average effective viscosity prescription. The k-ε analysis shows that the vortex associated with the bubble plume is relatively more turbulent ($k \simeq 10^{-3}$ m^2 s^{-2}; $\mu_T \simeq 2$ kg m^{-1} s^{-1}) compared to the outer contrarotating vortex with the bulk fluid, where $k \simeq 10^{-4}$ m^2 s^{-2} and $\mu_T \simeq 0.05$ kg m^{-1} s^{-1}. Predicted spatial distributions of effective viscosity shown in Fig. 1.25 provides a very reasonable representation of the observed distribution of turbulent characteristics (i.e., k) within the system (see Fig. 1.20).

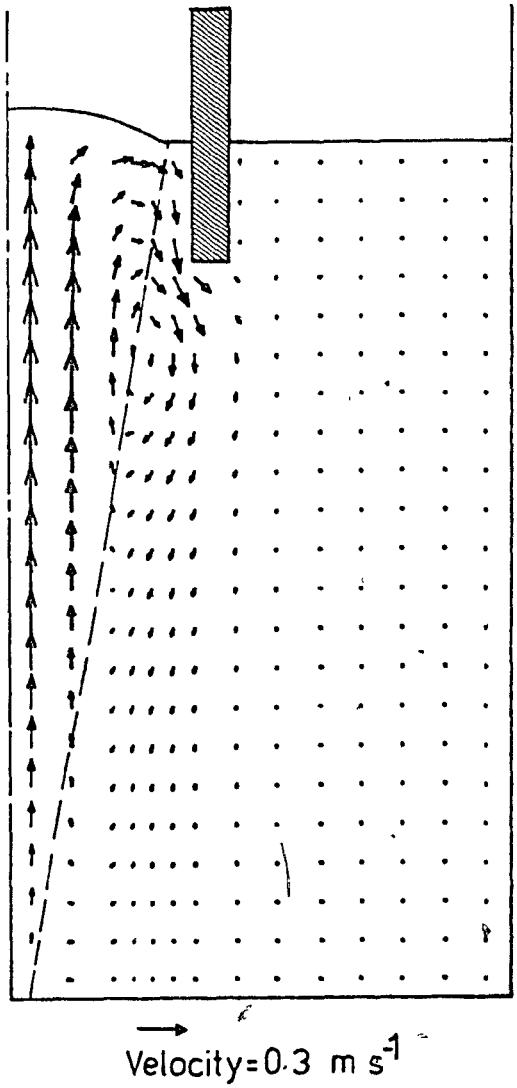

Figure 1.24 Predicted velocity field in water model for an assumed 25 pct wider plume in the Fig. 1.15(a).

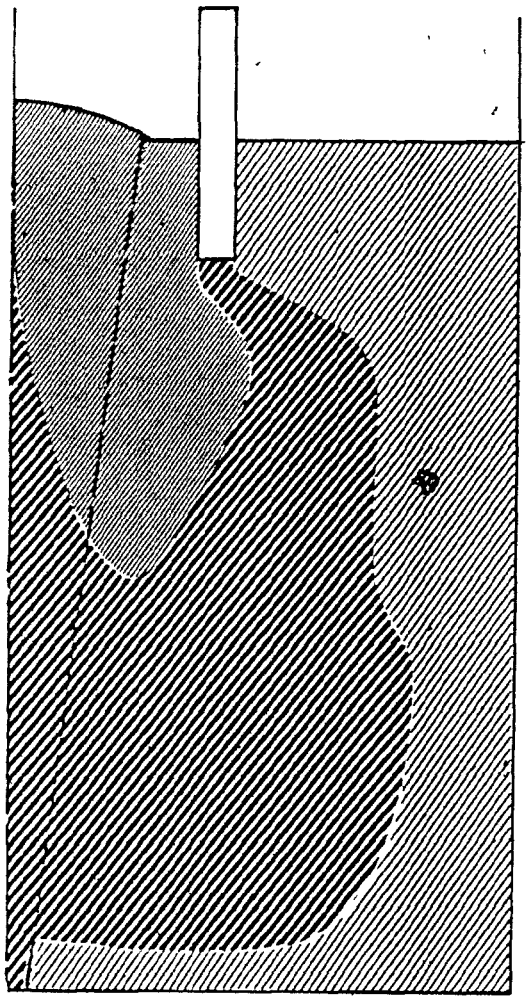

Figure 1.25 Predicted distribution of effective viscosity (Kg m^{-1} s^{-1}) in water model of dimensions and gas flow rate given in Table 1.3.

C. Industrial Applications

Evidently a comprehensive investigation of full scale liquid metal processing ladles would pose serious experimental difficulties. Indeed, many months and several thousand heats were needed to arrive at an empirical optimisation of the Gary Works C.A.S. operation (39). Consequently it is useful to extrapolate the present mathematical model beyond its currently validated limits of vessel size, gas flow rate and liquid, to predict liquid steel flows, plume velocities etc. in industrial size vessels.

As a typical example of the model's capabilities in this respect, predicted recirculatory flow fields generated in a typical 150 ton unbaffled ladle at a gas flow rate of 0.0188 $m^3 s^{-1}$ and 50 pct. lance submersion are presented in Fig. 1.26. The velocity field predicted in Fig.1.26 shows the strong recirculatory vortex characteristic of the 0.30 scale water model. As seen, plume velocities of about 1.1 m s^{-1} would be observed, and steel flow down the side-walls would exhibit velocities of approximately 0.35 m s^{-1}.

Table 1.5 presents the average recirculation speeds and the average plume velocities as a function of fractional depth of lance submergence. Although the flow patterns generated in these cases are very similar, one can note that increasing the lance depth by 20 to 25 pct. causes liquid steel recirculation speeds to increase by about 8 to 15 pct.

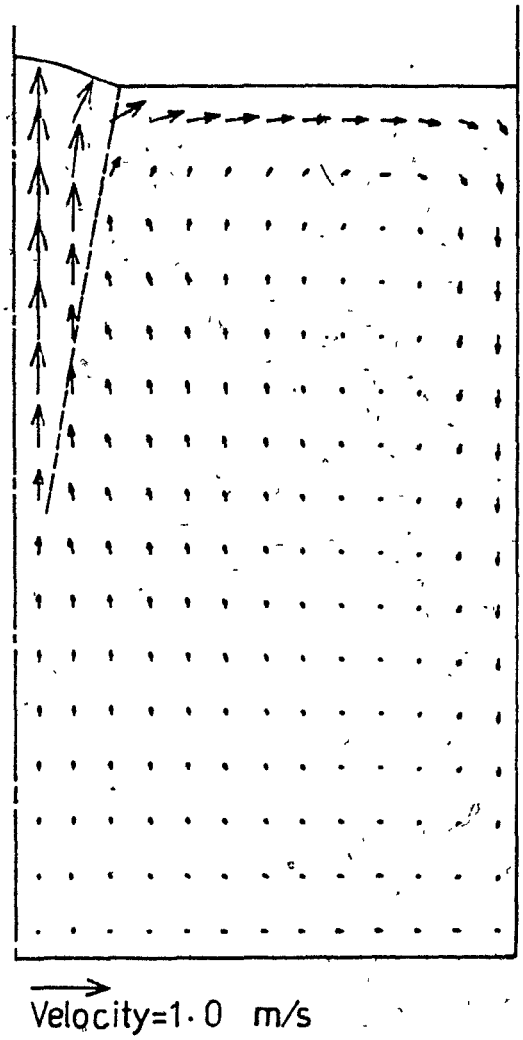

Figure 1.26 Predicted velocity field in a 150 ton cylindrical ladle with central gas injection at a gas flow rate of $1.88 \times 10^{-2} m^3/s$. (Vessel diameter= 3.65 m, liquid depth = 3.04 m and fractional depth of lance submergence = 0.5).

Table 1.5 Average bath recirculation speed and average plume velocity at different depths of lance submergence

Fractional Depth of Lance Submergence	Average Plume Velocity, $m\ s^{-1}$	Average Bath Recirculation Speed, $m\ s^{-1}$
0.50	0.92	0.136
0.75	1.06	0.156
0.95	1.14	0.167

Vessel diameter = 3.65 m, liquid depth = 3.04 m, and gas flow rate = $1.88 \times 10^{-2} m^3 s^{-1}$

Figure 1.27 presents the recirculatory flow field generated during gas injection at 50 pct. depth of lance submergence for a 150 ton teeming ladle with a taper of 5 deg, tapered rather than vertical ladle walls being more typical of industrial practice. It is significant to note that the taper causes a secondary recirculatory motion adjacent to the base of a typical ladle. Also, average speeds of recirculation are very similar to the equivalent untapered case (i.e., 0.129 m s^{-1} vs 0.136 m s^{-1}).

Figure 1.28 presents the predicted distribution of turbulence kinetic energy for the 150 ton ladle. As seen, maximum turbulence kinetic energies ranging between 0.06 to 0.015 m^2 s^{-2} are to be found in the plume region and close to the free surface, showing that turbulence mixing is most intensive in this region.

Predicted recirculatory flows generated in a 150 t ladle during C.A.S. procedure are presented in Fig. 1.29. The flow field in Fig. 1.29 shows the two recirculatory vortices in common with the 0.30 scale water model. As seen, plume velocities about 1.2 m/s would be observed, while upward flows of steel along the vertical side walls would be about 0.05 m/s. It is however interesting to note that steel flow down the wall of the central refractory cylinder would exhibit velocities as high as 0.50 m/s. The high momentum of outward flowing steel associated with this high velocity can be expected to cause

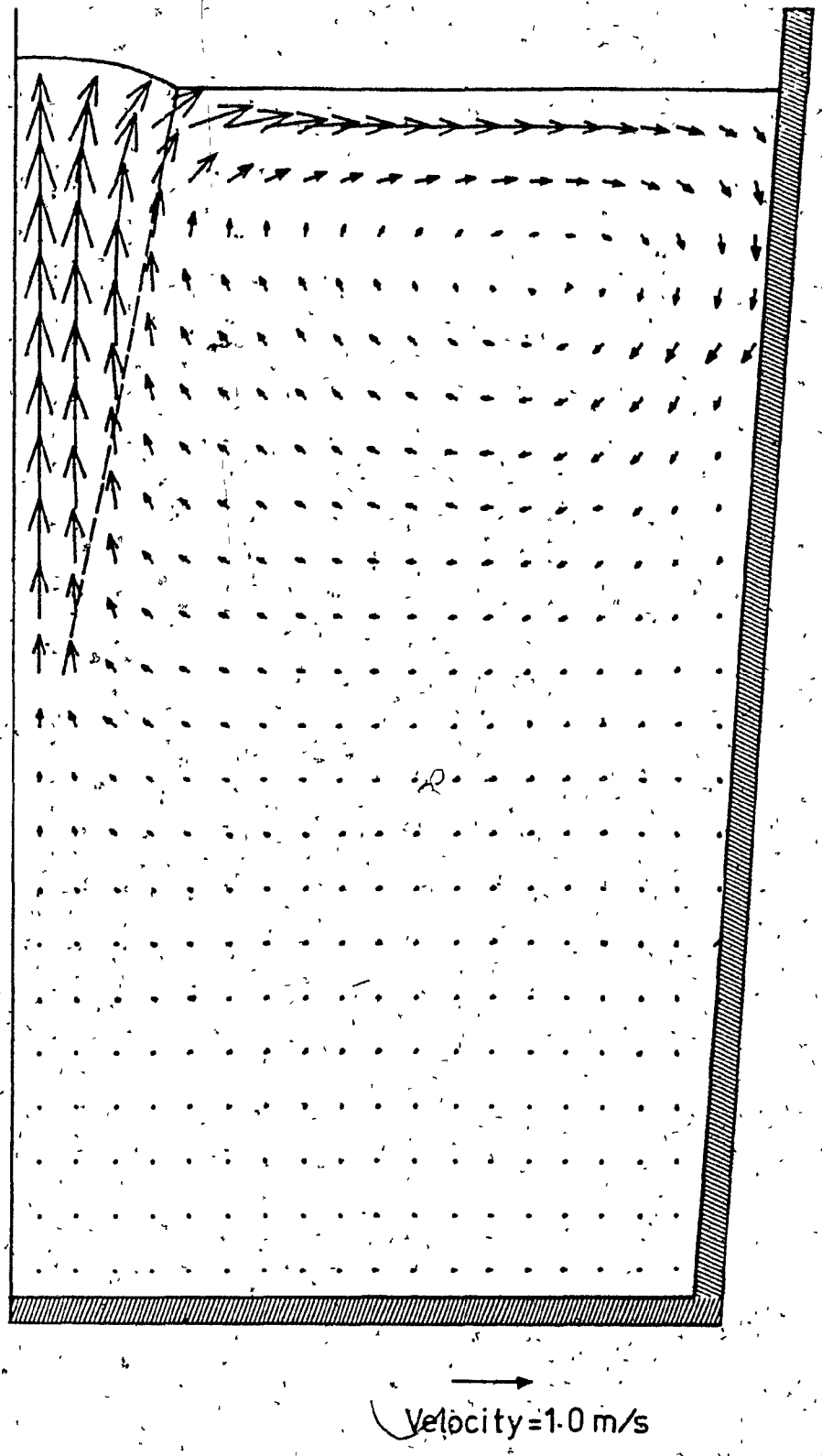

Figure 1.27 Predicted velocity field in a 150 ton steel ladle with central gas injection and a taper of 5 degree at a gas flow rate of $1.88 \times 10^{-2} m^3/s$. (Vessel radius= 1.825 m, liquid depth = 3.04 m, and fractional depth of lance submergence = 0.5).

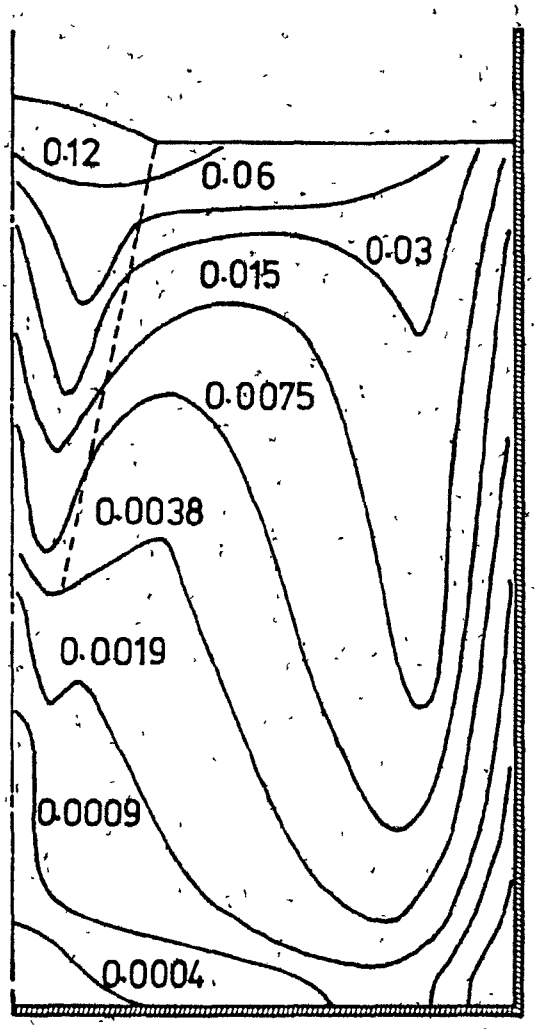

Figure 1.28 Predicted turbulence kinetic energy distribution ($m^2\ s^{-2}$) in the 150 ton vessel of dimensions and gas flow rate given in Fig. 1.26.

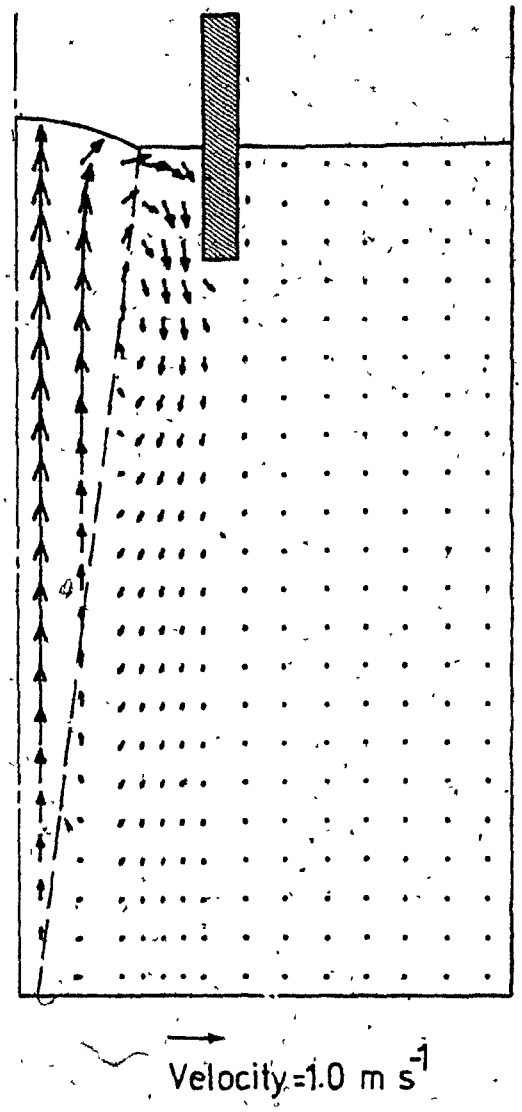

Figure 1.29 Predicted velocity field (m/s) in the 150 ton vessel of dimensions and gas flow rate given in Table 1.3.

hydrodynamic erosion of the refractory cylinder lining. This, in turn, could represent a source of inclusions.

Figure 1.30 shows flow fields generated during C.A.S. operations in a 150 t ladle with a taper of 5^{o}. Two points worth noting here are; a small secondary recirculation zone near the junction of the surface with the ladle side walls and secondly, the lower position of the recirculating vortex in the bulk compared to previous predictions in a vertical cylindrical ladle. These differences essentially result from the inclination of the side walls, even though this is only 5^{o}. It is noted that the lower position of the vortex in this ladle arises because of a lower rate of backflow in the upper regions of the tapered side walls as liquid moves towards the downcoming stream of steel adjacent to the rising plume. Continuity requirements for the tapered ladle then results in a lower position of the vortex.

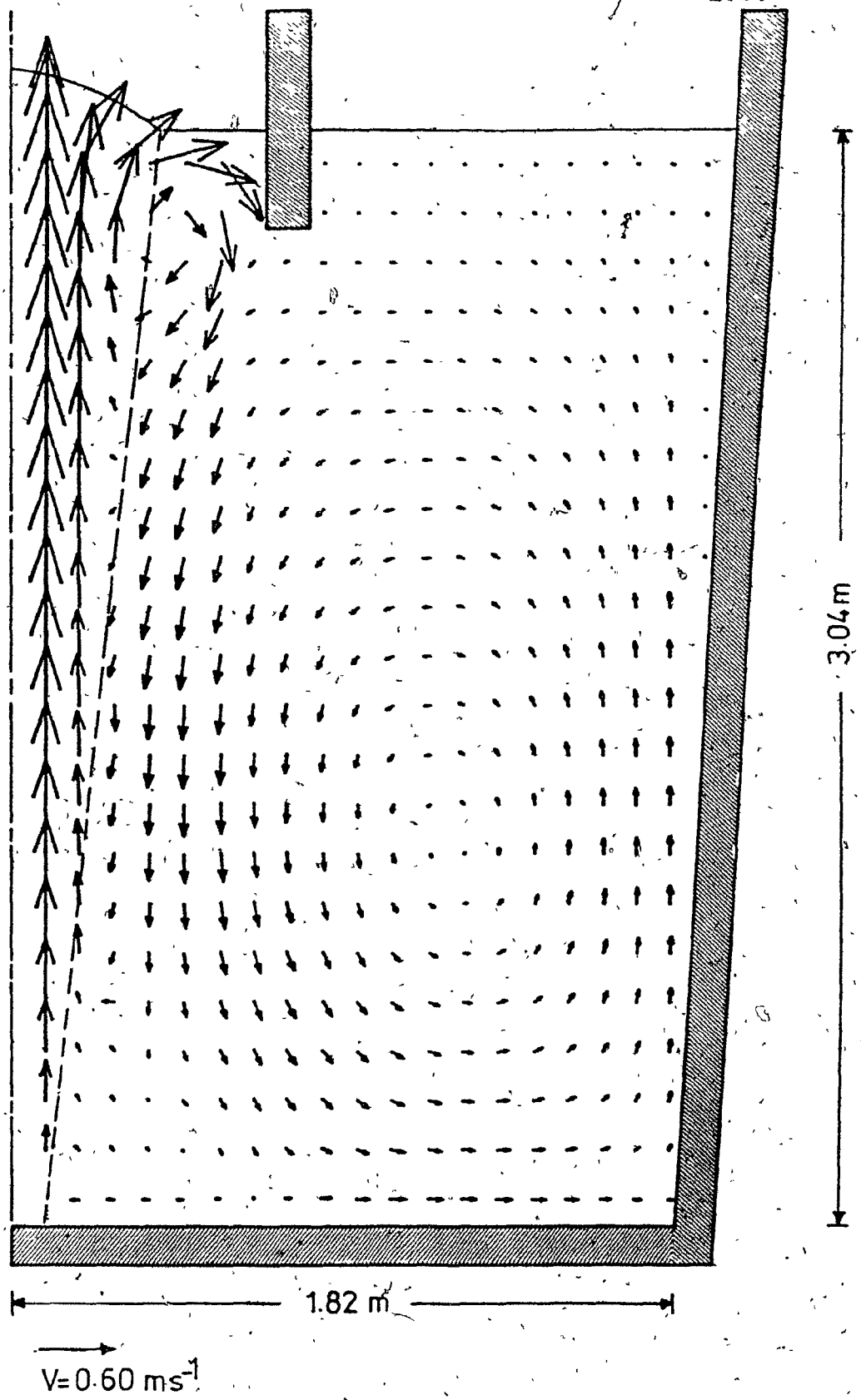

Figure 1.30 Predicted velocity field in a 150 ton steel ladle with a taper of 5°, of dimensions and gas flow rate given in Table 1.3.

CONCLUSIONS

A steady-state, turbulent flow model has been developed to model various axisymmetric gas injection configurations found in industrial ladle refining practices. On the basis of studies conducted with a reduced scale water model, it was demonstrated that quantitative agreement could be achieved between predicted and observed flow fields. This justifies the adequate nature of the current theoretical approach which is based on numerical solution of differential equations describing such phenomena.

LIST OF SYMBOLS

A_P, A_E, A_W, A_N, A_S	Coefficients of discretization equation (1.54) representing the effect of convection and diffusion
b_E, b_W, b_N, b_S	The proportion of control volume faces blocked by the obstacle in four different directions
b	Defined in equation (1.59)
c	Constant in expression for b; equation (1.59)
C	Constant defined by equation (1.39): has a value of 0.0055
C_D	Dissipation rate constant; has a value of 0.09
D	Diameter of the vessel, m
$d_{f.s}$	Diameter of the central refractory cylinder, m
k	Kinetic energy of turbulence per unit mass, $m^2\ s^{-2}$
k"	Constant defined by equation (1.52); has a value $4.19\ m^{1/12}\ s^{-2/3}$
$l_{f.s}$	Depth of refractory cylinder in the liquid, m
L,H	Liquid depth, m
N_B	Total number of bubbles in the plume
N_{Re}	Reynolds number, $\rho uL/\mu$
N_{Fr}	Froude number, u^2/gL
N_{Eu}	Euler number, $p/\rho u^2$
N_{We}	Weber number, $\rho u^2 L/\sigma$
p	Pressure within liquid (gauge; referenced to local hydrostatic pressure), Pa
Q	Gas flow rate, $m^3\ s^{-1}$

Q_m Model gas flowrate, $m^3\ s^{-1}$

$Q_{f.s}$ Gas flowrate in a full scale steel ladle, $m^3\ s^{-1}$

r The radial coordinate, m

r_o Radius of lance orifice, m

r_{av} Average plume radius, m (= $1/\sqrt{3}$ radius at surface)

R Radius of the vessel, m

S The source term in discretization equation (1.54)

S_c Constant part of linearised source term

S_p The slope of the linearised source term

t_R Average residence time of bubbles, s

u Axial component of velocity, $m\ s^{-1}$

$\bar{U}$ Mean speed of liquid recirculation, $m\ s^{-1}$ (Ref. 13)

U_p Average plume velocity, $m\ s^{-1}$

U_o Free space velocity of air through lance orifice, $m\ s^{-1}$

v Radial component of velocity, $m\ s^{-1}$

V_B Average volume of bubble in the plume, m^3

z_o Axial coordinate of nozzle exit, m

z The axial coordinate, m

α Volume fraction of gas in the plume

β Fractional depth of lance submergence

ε Turbulence kinetic energy dissipation rate per unit mass, $m^2\ s^{-3}$

μ, μ_L Molecular viscosity, $kg\ m^{-1}\ s^{-1}$

μ_e/μ_{eff} Effective viscosity, $kg\ m^{-1}\ s^{-1}$

μ_T Turbulence viscosity, $kg\ m^{-1}\ s^{-1}$

ν_T Turbulence kinematic viscosity ($= \mu_T/\rho$), $m^2\ s^{-1}$

Γ Turbulent exchange coefficient, $kg\ m^{-1}\ s^{-1}$

ρ Density, $kg\ m^{-3}$

ρ_L Density of liquid, $kg\ m^{-3}$

ρ_G Density of gas, $kg\ m^{-3}$

ϕ General variable of the discretization equation (1.54)

ϕ_o The half zet cone angle, radian

λ Geometrical scaling factor ($= L_m/L_{f.s}$)

C_1, C_2, C_D, σ_k and σ_ε Constants of k - ε turbulence model

$\dot{m}$ Mass flowrate, $kg\ s^{-1}$

u' Fluctuating velocity component, $m\ s^{-1}$

σ Surface tension, $Newton\ m^{-1}$

Γ_{eff} Effective exchange coefficient, $kg\ m^{-1}\ s^{-1}$

REFERENCES

1. D. Mazumdar and R.L. Guthrie: Metall. Trans., 1985, vol. 16B, pp. 83-90.

2. M. Salcudean and R.I.L. Guthrie: Metal. Trans., 1978, vol. 9B, pp. 673-680.

3. J.H. Grevet, J. Szekely and N. El-Kaddah: Int. J. Heat and Mass Transfer, 1982, vol. 25, No. 4, pp. 487-497.

4. J. Szekely, H.J. Wang and K.M. Kiser: Metall. Trans., 1976, vol. 7B, pp. 287-295.

5. J. Szekely, A.H. Dilawari and R. Metz: Metall. Trans., 1979, vol. 10B, pp. 33-41.

6. T. Debroy, A.K. Majumdar and D.B. Spalding: Applied Mathematical Modelling, 1978, vol. 2, pp. 146-150.

7. J. Szekely, T. Lehner and C.W. Chang: Ironmaking and Steelmaking, 1979, vol. 6, pp. 285-293.

8. T.C. Hsiao, T. Lehner and B. Kjellberg: Scand. J. Metallurgy, 1980, vol. 9, pp. 105-110.

9. J. Szekely, N. El-Kaddah and J.H. Grevet: Second International Conference on Injection Metallurgy, Jernkontoret, Sweden, 1980, pp. 5:1-32.

10. N. El-Kaddah and J. Szekely: Ironmaking and Steelmaking, 1981, vol. 6, pp. 269-278.

11. T. Debroy and A.K. Majumdar: Journal of Metals, 1981, vol. 33, No. 11, pp. 42-47.

12. Y. Sahai and R.I.L. Guthrie: Metall. Trans., 1982, vol. 13B, pp. 125-127.

13. Y. Sahai and R.I.L. Guthrie: Metall. Trans., 1982, vol. 13B, pp. 193-202.

14. Y. Sahai and R.I.L. Guthrie: Metall. Trans., 1982, vol. 13B, pp. 203-211.

15. J.W. McKelliget, M. Cross and R.D. Gibson: Applied Mathematical Modelling, 1982, vol. 6, pp. 469-480.

16. M. Salcudean, C.H. Low, A. Hurda and R.I.L. Guthrie: Chemical Engineering Communication, 1983, vol. 21, pp. 89-103.

17. M. Salcudean, K.Y.M. Lai and R.I.L. Guthrie: The Canadian Journal of Chemical Engineering, 1985, vol. 63, No. 1, pp. 51-61.

18. D. Mazumdar and R.I.L. Guthrie: Ironmaking and Steelmaking, in press.

19. D. Mazumdar and R.I.L. Guthrie: Applied Mathematical Modelling, in press.

20. N.C. Markatos: Proceedings, Second World Congress of Chemical Engineering, Montreal, Canada, 1980, vol. 5, pp. 301-305.

21. C. Aldham, N.C. Markatos and M. Cross: Proceeding of POLYMODELS, International Conference on Process Modelling, 1982, Teeside Polytechnique, Middlesborough, Cleveland, U.K.

22. A.D. Gosman, W.M. Pun, A.K. Runchal, D.B. Spalding and M. Wolfshtein: Heat and Mass Transfer in Recirculating Flows, Academic Press, London and New York, 1969.

23. D.B. Spalding: VDI - Forschungsh, 1972, vol. 38, No. 549, pp. 5-16.

24. W.M. Pun and D.B. Spalding: Proceeding of the XVII International Astronautical Congress, Pergamon Press/PWN - Polish Scientific Publishers, 1967, vol. 3, pp. 3-21.

25. S.V. Patankar and D.B. Spalding: Int. Journal Heat and Mass Transfer, 1972, vol. 15, pp. 1787-1805.

26. P.S. Bulson: Dock Harbour Authority, 1961, pp. 15-22.

27. G.B. Wallis: One Dimensional Two Phase Flow, McGraw Hill, New York, 1969.

28. B.E. Launder and D.B. Spalding: Computer Methods in Applied Mechanics and Engineering, 1974, vol. 3, pp. 269-289.

29. D.B. Spalding: Heat Transfer and Turbulent Buoyant Convection, D.B. Spalding and N. Afgan, eds., Hemisphere Publishing Corporation, New York, 1977, pp. 569-586.

30. C.W. Hirt and J.L. Cook: Journal of Computational Physics, 1972, vol. 10, pp. 324-340.

31. A.M.C. Chan and S. Banerjee: Journal of Heat Transfer, 1979, vol. 101, pp. 114-119.

32. F. Oeters, H.C. Dromer and J. Kepura: Third International Conference on Injection Metallurgy, 1983, Jernkontoret, Sweden, pp. 7:1-7:22.

33. R.E. Johnstone and M.W. Thring: Pilot Plants, Models and Scale-up Methods in Chemical Engineering, McGraw-Hill, New York, 1957.

34. S.V. Patankar: Proceeding of the Sixth International Heat Transfer Conference, Toronto, 1978, vol. 3, pp. 297.

35. A. Moult, D.B. Spalding and N.C. Markatos: Transaction of Institution of Chemical Engineers, 1979, vol. 57, pp. 200-204.

36. S.V. Patankar: Numerical Heat Transfer and Fluid Flow, Hemisphere Publishing Corporation, New York, 1980.

37. H.E. Cobus: Coastal Engineering Conference, London, 1968, Vol. II, pp. 1016-1031.

38. K.H. Tacke, H.G. Schubert, D.J. Weber and K. Schwerdtfeger: Metall. Trans., 1985, vol. 16B, pp. 263-275.

39. C.L. Trout, D.L. Paterson and S.M. Hughes: Proceeding of the AISE Conference, Pittsburg, Pennsylvania, 1983.

LIST OF FIGURES

Figure 1.12 Predicted velocity field (m/s) in water model for an assumed 50 pct wider plume than in fig. 1.9(a).

Figure 1.13 Predicted velocity field (m/s) in the water model (L = 0.93 m, R = 0.56 m) at a gas flow rate of $6.8 \times 10^{-4} m^3/s$, using the k-ε model with standard values of the empirical constants (viz. Table 1.2).

Figure 1.14 Predicted velocity field (m/s) in the water model for the same operating condition as those in Fig. 1.13, using the bulk-effective viscosity formula (viz. Eqn. 1.39).

Figure 1.15 (a) Experimentally measured velocity field (m/s) in water model using the video recording technique (liquid depth = 0.93 m, vessel radius = 0.56 m, gas flow rate = $6.8 \times 10^{-4} m^3/s$, inner radius of plexiglass cylinder = 0.19 m, plexiglass cylinder immersion depth = 0.12m).

(b) Visually observed flow field in the water model for the same conditions as those in Fig. 1.15 (a), using a suspended network of silken threads.

Figure 1.16 Predicted change in the turbulence kinetic energy dissipation rate (m^2/s^3) versus radius at Z/H = 0.80 for the conditions given in Fig. 1.15 (a).

Figure 1.17 Predicted radial variation of effective viscosity (kg/(m-s)) at Z/H = 0.80 for the conditions given in Fig. 1.15 (a).

Figure 1.18 Predicted velocity field (m/s) in the water model using the k-ε model with constants and their values shown in Table 1.4.

Figure 1.19 Comparison of theoretically predicted and experimentally measured vertical velocity component at four different depths in the water model for the conditions given in Fig. 1.15 (a). (Constants from Table 1.4 were used for prediction.)

Figure 1.20 Comparison of theoretically predicted, and experimentally measured, turbulence kinetic energy (m^2/s^2) at four different depths in the water model for the conditions given in Fig. 1.15 (a). (Constants from Table 1.4 were used for prediction.)

Figure 1.21 (a) Experimentally measured velocity field (m/s) in the water model (tank diameter = 1.12 m, liquid depth = 0.93 m, gas flow rate = $6.8 \times 10^{-4} m^3/s$, fractional depth of lance submergence = 0.5, inner radius of plexiglass cylinder = 0.19 m and plexiglass cylinder immersion depth = 0.12 m). (b) Theoretically predicted velocity field (m/s) in the water model of dimensions and gas flow rates given in (a). (c) Observed flow fields with a suspended gridwork of silken threads. (Computations in Fig. 1.21 (b) were based on the values of the constants given in Table 1.4.)

Figure 1.22 Comparison of experimentally measured and theoretically predicted vertical velocity component at different depths in water model for the conditions given in Fig. 1.21 (a). (Constants from Table 1.4 were employed for numerical computation.)

Figure 1.23 Comparison of experimentally measured and theoretically predicted turbulence kinetic energy (m^2/s^2) at four different depths in water model for the conditions given in Fig. 1.21 (a). (Constants from Table 1.4 were employed for numerical computation.)

Figure 1.24 Predicted velocity field in water model for an assumed 25 pct. wider plume in the Fig. 1.15 (a).

Figure 1.25 Predicted distribution of effective viscosity ($Kg\ m^{-1}\ s^{-1}$) in water model of dimensions and gas flow rate given in Table 1.3.

Figure 1.26 Predicted velocity field in a 150 ton cylindrical ladle with central gas injection at a gas flow rate of $1.88 \times 10^{-2} m^3/s$. (Vessel diameter = 3.65 m, liquid depth = 3.04 m and fractional depth of lance submergence = 0.5).

Figure 1.27 Predicted velocity field in a 150 ton steel ladle with central gas injection and a taper of 5 degree at a gas flow rate of $1.88 \times 10^{-2} m^3/s$. (Vessel radius = 1.825 m, liquid depth = 3.04 m, and fractional depth of lance submergence = 0.5).

Figure 1.28 Predicted turbulence kinetic energy distribution ($m^2\ s^{-2}$) in the 150 ton vessel of dimensions and gas flow rate given in Fig. 1.26.

Figure 1.29 Predicted velocity field (m/s) in the 150 ton vessel of dimensions and gas flow rate given in Table 1.3.

Figure 1.30 Predicted velocity field in a 150 ton steel ladle with a taper of 5^{o}, of dimensions and gas flow rate given in Table 1.3.

LIST OF TABLES

PART II

SUBSURFACE MOTIONS OF SOLID ADDITIONS IN LADLE METALLURGY OPERATIONS

ABSTRACT

Through a series of simple experiments, the extent of reduction in steady translational drag force in bubbly Newtonian liquids has been analysed. It has been found that small entrained bubbles can reduce drag on large spheres, the extent being proportional to gas flow rate. Taking a reduced drag coefficient (≈50%) in the gas-liquid region to that calculated from standard drag curve, the trajectories of spherical shaped particles in gas agitated cylindrical ladles were predicted from Newton's law for the system. The predicted trajectories were found to be in very reasonable agreement with those measured.

It was found that most buoyant particles (sp. gr. = 0.4 and 0.6) will hardly penetrate inside such baths, whereas neutrally buoyant particles have the potential to undergo prolonged subsurface motion. Heavier particles (sp. gr.= 1.14) on the other hand always settled to the ladle bottom.

The implication of these results together with an assessment of the relevance of these results to industrial size ladles are discussed in the text.

INTRODUCTION

The addition of alloying elements to liquid steel baths for adjusting steel chemistry to required specifications is common steelmaking practice. In the steelmaking industry where large tonnages of many grades of steel are made, there is considerable interest in developing, or at least identifying, cheap efficient methods of adding additions to steel baths. Although the bulk of the additions in today's steelworks are made in the holding vessels (e.g., ladles etc.) during furnace tapping, a specific problem faced by steelmakers for many years has been the low and erratic recoveries of light metal additions, particularly aluminium, etc.. Furthermore, the conventional argon stirring technique was not found to be a viable alternative for introducing buoyant alloy additions so as to improve their recovery rates.

To overcome these difficulties a superior method of alloy addition was introduced by Nippon Steel Corporation (1) in 1976. This novel addition making technique, known as C.A.S. (composition adjustment by sealed argon bubbling systems). utilizes argon gas that is bubbled into the molten steel through a porous plug or a submerged lance. The rising gas-liquid plume creates an opening in the slag cover through which a refractory lined cylinder is lowered into the steel. The essential idea is to make bulk alloy addition inside this slag free region under an inert atmosphere. This procedure of alloy addi-

tion is currently in practice at the Gary works of U.S. Steel Corporation (2). Although industry have reported (2) on superior and more reproducible aluminium recoveries, the nature of particle liquid interactions in such system remains yet to be quantified.

Also, it is necessary to recognise here that the additions in the C.A.S. procedure are introduced into a gas-liquid region, rather than into the bulk of a single phase. The purpose of the present work was to elucidate the movements of solids through this upwelling gas-liquid mixture. For convenience, the motions of spherical shaped additions were chosen for study.

PREVIOUS WORK

For a submerged spherical particle, moving through a fluid, Newton's second law of motion takes the following form (3):

$$\frac{4}{3}\pi R_p^3 \rho_p \frac{dU_p}{dt} = \frac{4}{3}\pi R_p^3 g\,(\rho_p - \rho) - \frac{C_D}{2}\pi R_p^2 \rho U_r |U_r|$$

$$- C_A \frac{4}{3}\pi R_p^3 \rho \frac{dU_p}{dt} - C_H R_p^2 (\pi\rho\mu)^{1/2} \int_o^t \frac{dU_p}{d\tau} \frac{d\tau}{\sqrt{t-\tau}} \qquad (2.1)$$

Guthrie et al. (4) showed that this equation was able to describe particle trajectories in a stagnant bath remarkably well, even though a cavity was formed during entry of the solid sphere into the liquid phase. In a series of model experiments, these authors (4) determined the trajectories of wooden spheres, dropped from typical industrial heights into vessels containing water. Comparisons were made between experimental and predicted trajectories, the latter being obtained through numerical integration of equation (2.1). It was shown that equally satisfactory, or even better results could be obtained without using the Basset history term. In their calculation, C_D was determined using the standard drag coefficient curve, and a classical value of 0.5 was taken for C_A. Predicted and measured maximum penetration depths were found to be in excellent agreement (within 5 pct.), over a wide range of conditions.

Tanaka (5) extended Guthrie et al's model (4) to predict spherical particle trajectories in recirculating flows (i.e., the motion of spherical particles in cylindrical vessels during simulated furnace tapping operations). In that study (5), not only was the effect of partial immersion of the particle at initial entry taken into account, but so also was the effect of cavity formation on the added mass coefficient. Based on published information (6), the added mass coefficient for the 'cavity running particle' was taken to be 60 pct. of its standard value. During partial submersion, each drag force was multiplied by the fraction of sphere volume immersed. Allowance was also made for initial entry in the added mass term. Once again, measured and predicted maximum immersion depths, total immersion times etc. were found to be in excellent agreement.

The computer program originally developed by Tanaka (5), was used by the author to predict subsurface trajectories of spherical additions in the C.A.S. system. These trajectories were calculated for the flow fields which had already been established and reported in Part I of this thesis.

PRESENT WORK

In making numerical predictions of particle motion in the gas-liquid plume region of a gas stirred ladle, it was not obvious that the standard drag coefficients for submerged objects in steady translation could be used. However a literature survey on the subject yielded no information on the matter.

It was found that the depth of penetration of 25.4 mm diameter buoyant spheres (0.4, 0.6 and 0.99 specific gravity) into the plume region were some 50 to 60 pct. greater than those predicted on the basis of Newton's law for this system (4).

The effect is illustrated in Fig. 2.1, for a typical buoyant addition (sp. gr = 0.99). As seen predicted and measured subsurface trajectories show major differences. Since the flow fields, added mass effect, buoyancy forces and gas voidage were well prescribed, it seemed likely that there might be a more fundamental reason for this discrepancy, i.e., reduced drag forces on submerged objects in bubbly flow systems.

A. Measurement of Drag Coefficient in Bubbly Newtonian Liquids

Figure 2.2 shows the apparatus that was built to test this hypothesis. A vertical plexiglass column (L = 0.85 m, ID = 0.076 m) was provided with three inlets at its base so that water and air could be introduced. A perforated plate with nine symmetrical holes (5.0 mm diameter) was fitted inside the column at a height of about 0.16 m from the bottom, in order to produce a fine dispersion of gas bubbles within the rising flow of

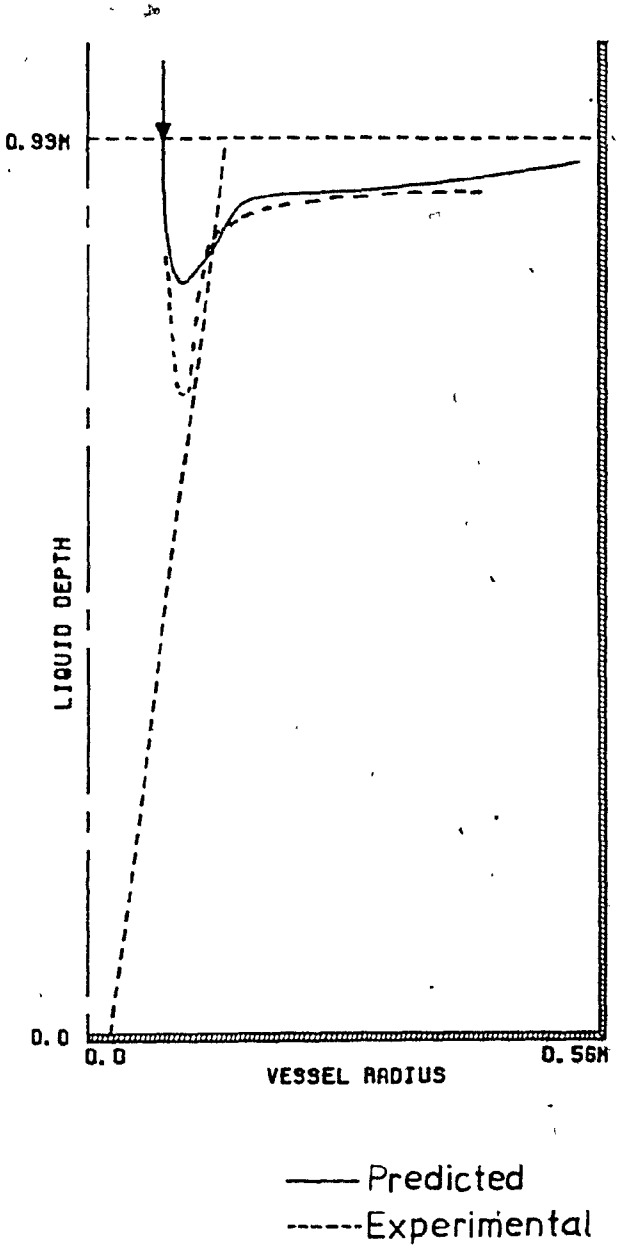

Figure 2.1 Predicted subsurface trajectory of buoyant spherical particle (Sp. gr. = 0.991) in an unbaffled water model ladle (L = 0.93 m, R = 0.56 m, Q = 6.8×10^{-4} m^3/s, $\beta = 0.94$) using drag coefficient valued derived from standard Re v. C_D curve[8] (U_{entry} = 3.83 m/s).

Figure 2.2 The experimental set-up used for measuring drag coefficients in bubbly Newtonian liquids.

(a) The plexiglass column filled with water.

(b) A suspended wooden sphere in a gas-liquid dispersion.

liquid. Three wooden spheres with specific gravity approximately 1.03 were made, their features and properties being listed in Table 2.1.

At the beginning of each experiment, water was introduced inside the column through the central inlet, and a sphere was dropped inside the column. The flow of water was then carefully regulated so as to position the sphere into a zone of equilibrium, within the flowing liquid. Using this approach, liquid flow rates could be recorded, and an average liquid velocity determined.

Once the sphere was essentially stationary for periods of 30 to 40 seconds, gas was then introduced inside the column using the two other inlets. The spheres would then begin to sink and liquid flows had to be increased, so as to establish the sphere in its equilibrium zone. The water flow rate needed to do this was again measured and an average liquid velocity determined. Three measurements were carried out on each sphere and averaged. The procedure was repeated for all three spheres.

Three gas flow rates were investigated. These were chosen so that the volume fraction of gas inside the column varied between 1 to 10 pct., this being typical of some chemical and metallurgical gas injection practices (7).

Table 2.1 Physical characteristics of wooden spheres used for measurement of drag coefficients.

Sphere No.	Mass, 10^{-3} kg	Radius, 10^{-2} m	Volume, 10^{-6} m^3	Density, 10^3 kgm^{-3}
1	9.032	1.278	8.743	1.033
2	9.027	1.279	8.764	1.030
3	8.984	1.277	8.723	1.030

B. Measurement and Prediction of Trajectories of Spherical Particles in Gas-Stirred Ladles

Modelling criteria

To determine the experimental conditions necessary to provide adequate simulation, on the basis of Froude modelling criteria used for the flow field investigation outlined in Part I, it was necessary that

(i) the particle diameter be,

$$d_{p,m} = \lambda \cdot d_{p,f.s} \tag{2.2}$$

(ii) and the entry velocity of the particle be,

$$U_{entry,m} = \sqrt{\lambda} \cdot U_{entry,f.s} \tag{2.3}$$

Recognising that the forces of greatest significance acting on a submerged particle in the present system, were those relating to the particle weight, F_g, its buoyancy, F_B, fluid drag forces, F_D, and added mass force, F_A, resulting during periods of acceleration or deceleration in the fluid, Newton's equation of motion takes the following form for a spherical shaped particle:

$$\frac{4}{3} \pi R_p^3 \rho_p \frac{dU_p}{dt} = F_g + F_B + F_D + F_A \tag{2.4}$$

where,

$$F_g = \frac{4}{3} \Pi R_p^3 \rho_p g \tag{2.5}$$

$$F_B = -\frac{4}{3} \Pi R_p^3 \rho g \tag{2.6}$$

$$F_D = -C_D \frac{\Pi R_p^2 \rho}{2} U_r |U_r| \tag{2.7}$$

and $$F_A = -C_A \frac{4}{3} \Pi R_p^3 \rho \frac{dU_p}{dt} \tag{2.8}$$

The added mass term, F_A, can be regarded as an 'apparent (or added mass') of fluid associated with the particle. Thus equation (2.4) becomes

$$(M_S + M_A) \frac{dU_p}{dt} = F_g + F_B + F_D \tag{2.9}$$

where,

$$M_S = \frac{4}{3} \Pi R_p^3 \rho_p \tag{2.10}$$

and $$M_A = C_A \frac{4}{3} \Pi R_p^3 \rho \tag{2.11}$$

Equation (2.9) signifies that the trajectory of the particle together with its 'apparent mass' $(M_S + M_A)$ is determined by gravitational, buoyant and drag forces.

Based on Froude number similarity between model and prototype, the ratio of equivalent forces then became:

$$\frac{(F_g)_m}{(F_g)_{f.s}} = \frac{\rho_{p,m}}{\rho_{p,f.s}} \lambda^3 \tag{2.12}$$

$$\frac{(F_B)_m}{(F_B)_{f.s}} = \frac{\rho_m}{\rho_{f.s}} \lambda^3 \tag{2.13}$$

$$\frac{(F_D)_m}{(F_D)_{f.s}} = \frac{(C_D)_m}{(C_D)_{f.s}} \frac{\rho_m}{\rho_{f.s}} \lambda^3 \tag{2.14}$$

Similarly,

$$\frac{(M_S + M_A)_m}{(M_S + M_A)_{f.s}} = \frac{|\nu_m + (C_A)_m|}{|\nu_{f.s} + (C_A)_{f.s}|} \frac{\rho_m}{\rho_{f.s}} \lambda^3 \tag{2.15}$$

As is clear from equation (2.9), corresponding particles in the model and in the full scale system will exhibit geometrically similar trajectories if, and only if,

$$\left(\frac{dU_p}{dt}\right)_m = \left(\frac{dU_p}{dt}\right)_{f.s} \tag{2.16}$$

or,

$$\frac{(F_g + F_B + F_D)_m}{(F_g + F_B + F_D)_{f.s}} * \frac{(M_S + M_A)_{f.s}}{(M_S + M_A)_m} = 1 \tag{2.17}$$

Using relationships from equation (2.12) to equation (2.15), one finds that the identity (viz. equation (2.17) holds between model and full scale provided ν, the particle/liquid density ratio, is equivalent for the two, and provided the values of drag coefficient and added mass coefficients are identical for both systems. Even though the drag coefficient is a function of Reynolds number and turbulence intensity, it does remain practically constant at $10^3 \sim 10^5$ Reynolds numbers, provided turbulence intensity is sufficiently small. Therefore, if corresponding particles in model and full scale system experience Reynolds number of $10^3 \sim 10^5$ at small levels of turbulence intensity, they should exhibit geometrically similar trajectories in recirculating baths and ladles.

However, apart from the above-mentioned case, drag coefficients in the model and prototype generally differ from each other depending on their Reynolds number and depending on the turbulence intensity of the fluid. Consequently, in this investigation of particle trajectories, the agreement between the results of the model study and those which are to be expected to happen in full scale systems is considered to be quite representative, but not completely quantitative.

The mathematical model

As mentioned previously, the history term in equation (2.1) could be ignored because the Reynolds number is high throughout the sphere's motion. Consequently, equation (2.1) takes the

following form:

$$\frac{4}{3}\pi R_p^3 \rho_p \frac{dU_p}{dt} = \frac{4}{3}\pi R_p^3 g\,(\rho_p - \rho) - \frac{C_D}{2}\pi R_p^2 \rho U_r |U_r| - C_A \frac{4}{3}\pi R_p^3 \rho \frac{dU_p}{dt} \tag{2.18}$$

or,

$$(\rho_p + C_A\rho)\frac{dU_p}{dt} = (\rho_p - \rho)g - \frac{3C_D}{8R_p}\rho U_r |U_r| \tag{2.19}$$

where,

$$\frac{dX}{dt} = U_p \tag{2.20}$$

Figure 2.3, shows, in schematic form the forces acting on a spherical particle. Since both particle and fluid are supposed to be in motion the force directions are not simple. F_g and F_B represent the gravitational and buoyant forces respectively, and, as such are parallel to gravity. F_D, the drag force, is taken to be parallel to the relative velocity of the particle in the fluid. F_A, the added mass term, is taken to be parallel to the acceleration vector of the particle. Furthermore, any rotation of the particle during its translation has been ignored.

These simultaneous ordinary differential equations (viz., equations (2.19) and (2.20) were first written for the two

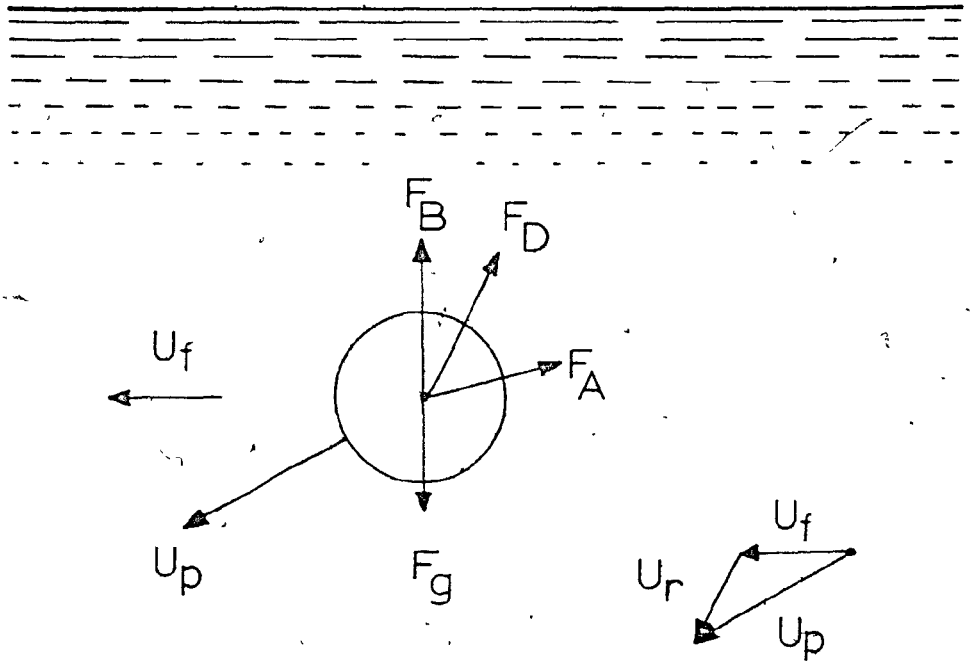

$$F_D \parallel U_r$$

$$F_A \parallel \frac{dU_p}{dt}$$

$$F_g, F_B \parallel g$$

Figure 2.3 Forces acting on a spherical particle in a recirculating bath.

coordinate directions (i.e., axial and radial axes respectively). The initial, and boundary, conditions employed were, (i) at t = 0 and z = 0, $u_p = U_{entry}$ along the axial coordinate and (ii) at t = 0 and r = r_{entry}, $v_p = V_{entry}$ (V_{entry} = 0 for vertical entry) along the radial axis. The set of equations together with the corresponding initial and boundary conditions were then numerically solved by a fourth order Runge-Kutta-Gill method (5).

However, before carrying out any trajectory prediction in gas stirred systems, it was first necessary to re-evaluate the performance of the computer program (5), so that the prediction of particle trajectories could be made with some confidence. Consequently, as a preliminary test, trajectories of buoyant spherical particles (ρ_p = 600 kg/m^3, d_p = 10 mm and U_{entry} = 2.7 m/s) in stagnant water were computed and in Fig. 2.4 compared directly against equivalent computations by Tanaka (5). As expected perfect agreement between the two sets of computations was achieved.

Experimental work

Based on equation (2.2), four wooden spheres of approximately 25.4 mm diameter and various densities were made. The densities chosen were 400, 600, 900, and 1400 kg/m^3 as shown in Table 2.2, to reflect the apparent densities of typical alloy additions used in steelmaking. The latter are given in Table 2.3.

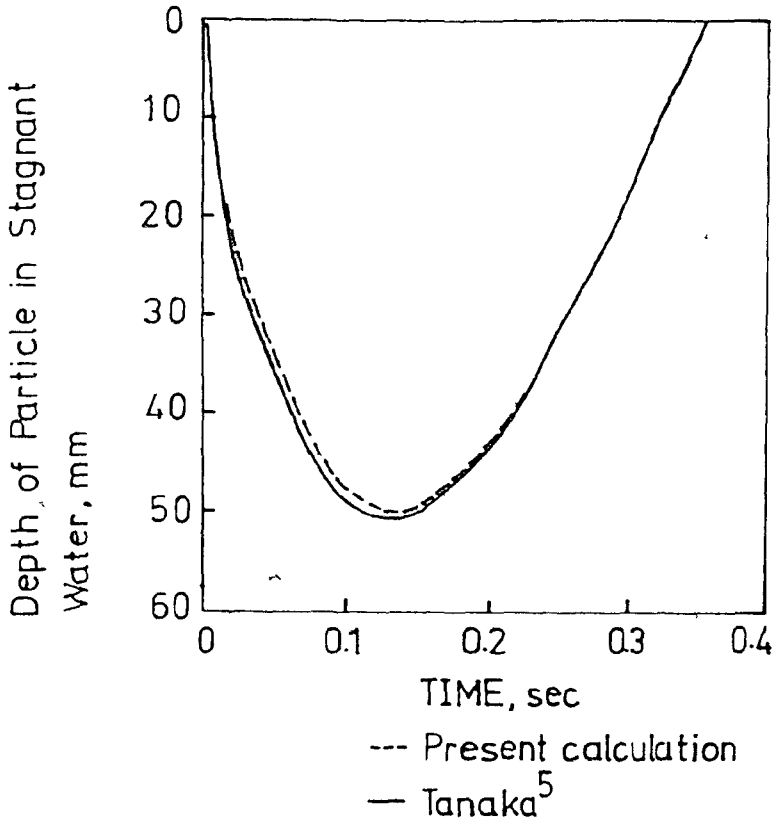

Figure 2.4 Predicted trajectory (time v. depth) of a buoyant spherical particle (ρ_p = 600 Kg/m^3, d_p = 10 mm and U_{entry} = 2.7 m/s) in stagnant water and its comparison with an equivalent computation reported by Tanaka (5).

Table 2.2 Dimensions and densities of spherical particles in model experiments

Sphere Number	Diameter 10^{3}m	Volume $10^{-9}m^{3}$	Mass 10^{-3}Kg	Density $10^{6}Kg/m^{3}$	Apparent Density
1	25.6	8784.6	3.56	0.000405	0.405
2	25.5	8682.0	5.21	0.0006	0.600
3	25.4	8580.3	8.51	0.000991	0.991
4	25.5	8682.0	9.89	0.00114	1.14

Table 2.3 Apparent densities of some alloy additions used in steelmaking

Alloys/Deoxidizers	Apparent Density
Al	0.39
50% FeSi	0.58-0.67
FeMn	0.90-1.04
FeNb	1.15

The particle's 25.4 mm diameter represented typical 80 ∿ 90 mm lump additions for a full scale operation.

The wooden spheres were dropped in free fall, from a constant height of approximately 0.20 m above the bath surface, so as to give a constant entry velocity of approximately 2.0 m/s. The velocity of 2 m/s was determined on the basis of equation (2.3), in which frictional effects could be ignored (4), i.e.,

$$U_{entry,m} = \sqrt{2gH_{f,m}} \qquad (2.21)$$

The height of fall in the model, $H_{f,m}$ $(=\lambda H_{f,f.s})$, was estimated according to the 0.70 m drop height from the alloy chute position to the liquid steel surface in the industrial equipment summarised in reference 1.

Flow fields were generated using the same equipment and techniques as those described in Part I. For observation of trajectories, the whole inside of the tank was illuminated from above, using two 500 W photographic lamps. All particle trajectories were recorded on video tape and subsequently analysed. To facilitate this, a 50 x 50 mm grid network was constructed on the front plexiglass plate of the water model tank. In constructing the grid network, due care was taken to compensate for parallex effects. A minimum of three runs were carried out for each set of conditions.

It is to be noted here that for particles with specific gravities 0.4, 0.6 and 1.14, only marginal differences in successive trajectories were observed as illustrated in Figs. 2.8 through 2.15. Owing to the complexities (i.e., intermittent discontinuous two phase flow) at the edge of the gas-liquid boundary it is surprising such small variations were observed experimentally. As a result, all trajectories were essentially reproducible, barring the neutrally buoyant addition as shown in Fig. 2.7.

It is also to be mentioned here that to study the spherical particle trajectories in the C.A.S. configuration, two different hollow plexiglass cylinders were employed (0.30 m and 0.39 m internal diameter respectively). Their depth of immersion was however kept constant ($\sim$0.12 m). The diameter of the central plexiglass cylinder had practically no significant effect on the overall nature of the particles' trajectories.

RESULTS AND DISCUSSION

A. Drag Coefficient in Bubbly Newtonian Liquids

When the sphere is in equilibrium and only water flows past it (see Fig. 2.2), drag and gravity forces must balance each other. Consequently, equation (2.1) reduces to

$$\frac{C_D}{2} \Pi R_p^2 \rho_\ell U_\ell^2 = \frac{4}{3} \Pi R_p^3 (\rho_p - \rho_\ell) g \qquad (2.22)$$

Since all the parameters appearing are known, U_ℓ the liquid velocity being obtained from Q_l/A_t, where Q_l is the liquid flowrate and A_t is the cross sectional area of the tube, drag coefficients, C_D, are readily calculable via equation (2.22). The drag coefficients derived by this procedure, and corresponding to particle Reynolds numbers between 3000-3600, are compared with standard literature values (8) in Table 2.4. These show, that despite ignoring possible effects of turbulence intensity (9) and the simplicity of the experimental procedure, reasonably accurate values for C_D were possible.

As previously mentioned, introducing gas into the column, caused the spheres to settle, even though a number of micro-bubbles sometimes stuck to their surfaces. The spheres were treated with wetting reagents, prior to experiments, so as to keep such bubble attachment to a minimum. This settling is indicative of the fact that gas-liquid dispersions cause some

Table 2.4 Experimental drag coefficients in a homogeneous liquid, compared with standard values[8]

Sphere Number	Experiment Number	Volumetric Flow Rate of Water $10^{-4}m^3/sec$	Particle Reynolds Number $U_\ell d_p \rho_\ell / \mu_\ell$	Standard Drag Coefficients	Measured Drag Coefficients	Average Drag Coefficients
1	A(1)	7.75	4368	0.385	0.36	0.393
	B(1)	7.66	4321	0.385	0.38	
	C(1)	7.33	4133	0.384	0.44	
2	A(2)	6.5	3666	0.384	0.39	0.433
	B(2)	6.83	3854	0.384	0.44	
	C(2)	6.83	3854	0.384	0.47	
3	A(3)	6.75	3800	0.384	0.46	0.456
	B(3)	7.16	4034	0.384	0.44	
	C(3)	7.00	3941	0.384	0.47	

reduction in drag below that observed in homogeneous fluids. Consequently, in all experiments, liquid flow-rate had to be increased in order to make the entrained submerged sphere stationary with respect to the experimentalist.

Thus, when the sphere was in equilibrium in an upwelling gas-liquid dispersion, the appropriate force balance equation is:

$$\frac{C_D}{2} \pi R_p^2 \rho_{mix} U_{mix}^2 = \frac{4}{3} \pi R_p^3 (\rho_p - \rho_{mix}) g \qquad (2.23)$$

where, the average gas-liquid velocity is given by

$$U_{mix} = U_{ol} + U_{og} \qquad (2.24)$$

Here the nominal or superficial gas velocity, U_{og}, and superficial liquid velocity, U_{ol}, were estimated from corresponding flow rates and the cross sectional area of the column. The mixture density, ρ_{mix}, was defined and estimated according to:

$$\rho_{mix} = \alpha \rho_G + (1 - \alpha) \rho_\ell \qquad (2.25)$$

or $$\rho_{mix} \simeq (1 - \alpha) \rho_\ell \qquad (2.26)$$

Here, α is the volume fraction of gas within the column. Depending on whether there is gas slippage through the liquid or

not, α can be approximated via the following expressions:

$$\alpha = \frac{U_{og}}{U_{ol} + U_{og}} \tag{2.27}$$

for zero slip, and

$$\alpha = \frac{U_{og}}{U_{ol} + U_{og} + U_{B}} \tag{2.28}$$

for slip.

U_B, in equation (2.28) is the rise velocity of a single bubble through a quiescent liquid. Obviously, U_B depends on the average bubble size in the system.

Using these procedures, drag coefficients in the bubbly water environments were estimated from equation (2.23), for both slip and non-slip conditions, and reported in Tables 2.5 to 2.7.

There, it is clear that provided the physical situation within the gas-liquid mixture corresponds to gas slippage, there can be a considerable decrease in a sphere's drag coefficients in bubbly water. However, if zero slip conditions apply, any C_D reductions become equivocal as seen from Tables 2.5 to 2.7. These also contain drag coefficients in bubbly water, as estimated from the standard drag curve and the corresponding Reynolds numbers ($= |U_{mix} d_p \rho_\ell (1 - \alpha)| / |\mu_\ell (1 - \alpha)|$) of the three

Table 2.5 Experimental drag coefficients in a gas-liquid dispersion [$Q_g = 0.083 \times 10^{-4} m^3/sec$].

Sphere Number	Experiment Number	Volumetric Flow Rate of Liquid $10^{-4} m^3/sec$	Particle Reynolds Number $U_{mix} d_p \rho_\ell / \mu_\ell$	Standard Drag Coefficient	Measured Drag Coefficient		Average Drag Coefficient
					No Slip	Slip	(Slip)
1	A(1)	8.83	5024	0.387	0.37	0.33	0.360
	B(1)	8.16	4648	0.386	0.43	0.39	
	C(1)	8.50	4835	0.385	0.40	0.36	
2	A(2)	7.83	4462	0.385	0.44	0.40	0.382
	B(2)	8.16	4651	0.386	0.40	0.366	
	C(2)	8.0	4556	0.386	0.42	0.38	
3	A(3)	8.16	4649	0.385	0.40	0.365	0.385
	B(3)	7.75	4408	0.385	0.44	0.40	
	C(3)	7.83	4457	0.385	0.43	0.39	

Table 2.6 Experimental drag coefficients in a gas-liquid dispersion [$Q_g = 0.21 \times 10^{-4} m^3/sec$].

Sphere Number	Experiment Number	Volumetric Flow Rate of Liquid $10^{-4} m^3/sec$	Particle Reynolds Number $U_{mix} d_p \rho_\ell / \mu_\ell$	Standard Drag Coefficient	Measured Drag Coefficient		Average Drag Coefficient
					No Slip	Slip	(Slip)
1	A(1)	9.33	5344	0.389	0.43	0.36	0.345
	B(1)	9.75	5612	0.390	0.387	0.327	
	C(1)	9.42	5400	0.389	0.42	0.35	
2	A(2)	8.83	5099	0.387	0.45	0.38	0.36
	B(2)	9.33	5347	0.389	0.42	0.35	
	C(2)	9.33	5347	0.389	0.42	0.35	
3	A(3)	9.5	5372	0.389	0.39	0.33	0.35
	B(3)	9.16	5226	0.387	0.43	0.357	
	C(3)	9.16	5226	0.387	0.43	0.357	

Table 2.7 Experimental drag coefficients in a gas-liquid dispersion [$Q_g = 0.29 \times 10^{-4} m^3/sec$].

Sphere Number	Experiment Number	Volumetric Flow Rate of Liquid $10^{-4} m^3/sec$	Particle Reynolds Number $U_{mix} d_p \rho_\ell / \mu_\ell$	Standard Drag Coefficient	Measured Drag Coefficient		Average Drag Coefficient
					No Slip	Slip	(Slip)
1	A(1)	9.83	5707	0.390	0.42	0.34	0.326
	B(1)	10.16	5893	0.392	0.39	0.32	
	C(1)	10.16	5893	0.392	0.39	0.32	
2	A(2)	9.83	5708	0.390	0.40	0.33	0.346
	B(2)	9.66	5610	0.390	0.43	0.35	
	C(2)	9.42	5471	0.389	0.44	0.36	
3	A(3)	9.83	5709	0.390	0.40	0.33	0.336
	B(3)	9.66	5604	0.390	0.42	0.34	
	C(3)	9.66	5604	0.390	0.42	0.34	

spheres tested. These, however, show that for the situation of gas slippage through the liquid, the measured drag coefficients are lower than the standard values calculated.

In analysing these reductions in drag coefficients as shown in Tables 2.5 to 2.7, it was found that the percent reduction in experimentally measured drag coefficients (i.e., $\{|C_{D,S} - C_{D,Gas}|/C_{D,S}\} * 100$) is practically linearly related to the volume fraction of gas, within the column. This is shown in Fig. 2.5. Extrapolating these to the 7 ∿ 8 pct. voidage figure of relevance to the C.A.S. operation, one finds that the corresponding reduction in drag coefficients is approximately 50 pct.. New particle trajectory predictions could then be made on the basis of this information.

Parallel to this, four possible mathematical models were also considered in trying to account for the discrepancy between the observed and measured maximum penetration depths of buoyant additions. These involved the following specifications for the governing differential equation:

(i) reduced fluid density in the plume; standard C_D,

(ii) reduced fluid density and viscosity in the plume; standard C_D,

(iii) reduced fluid density and viscosity in the plume; 50 pct. of standard C_D in the plume and

(iv) reduced fluid density and viscosity in the plume; standard C_D, accounting for the effect of turbulence intensity on drag coefficient.

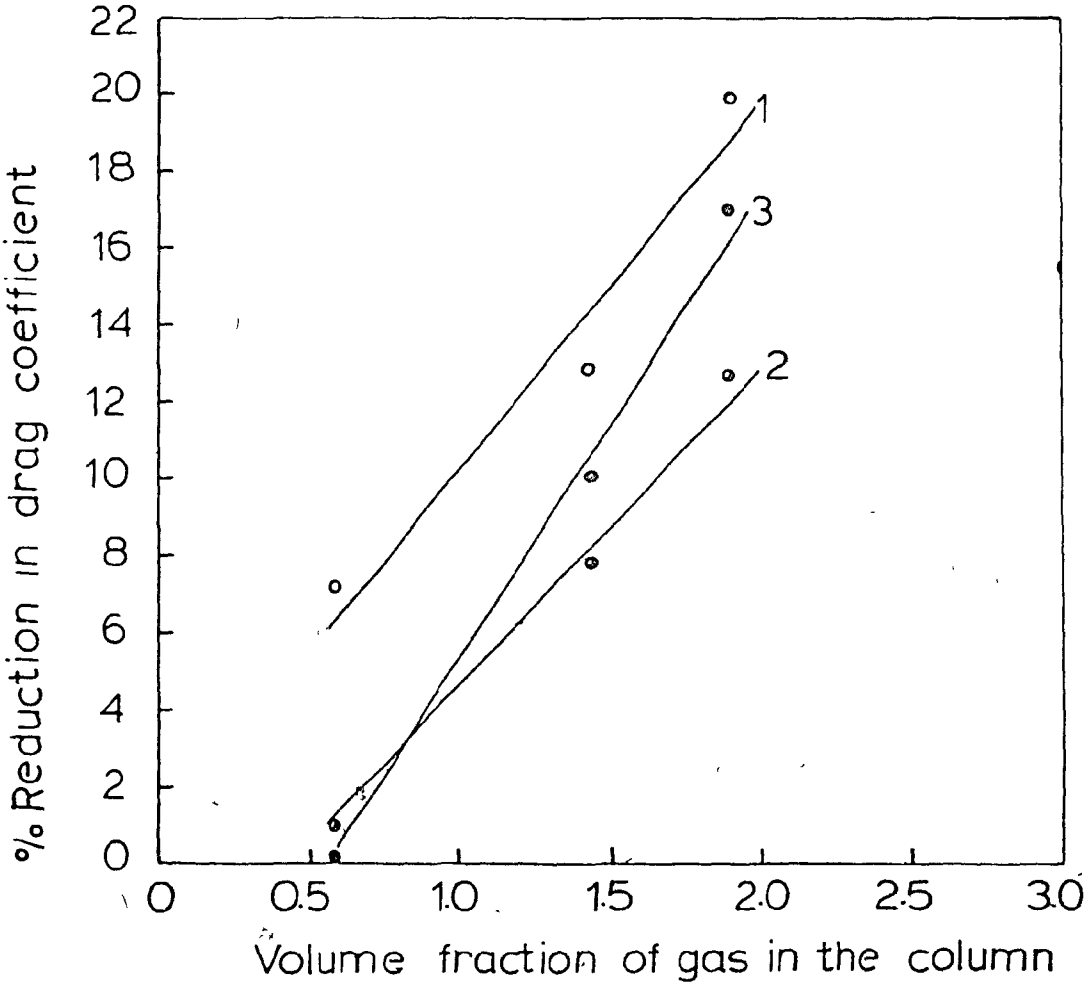

Figure 2.5 Effect of volume fraction of gas in the gas liquid dispersion on the extent of reduction in translational drag on three spherical particles (viz., Table 2.1).

The four corresponding maximum penetration depths predicted for the buoyant sphere (sp. gr. = 0.99) are given in Table 2.8, together with those measured experimentally. There it is readily seen that the predictions via model (iii) (i.e., reduced fluid density and viscosity in the plume; 50 pct. of standard C_D in the plume) is the only combination to provide a maximum depth of penetration that is within 10% of those experimentally measured.

Considering therefore, a 50 pct. reduction in C_D from standard values, the trajectory of the buoyant particle (sp. gr. = 0.99) was recalculated and is shown in Fig. 2.6. The agreement between experimental and predicted trajectories there, is seen to be very close.

The results presented so far appear to indicate that gas-liquid dispersions cause some reduction in drag coefficients versus those observed for homogeneous liquids. However, future work over a much broader experimental range is recommended in order to clarify and quantify the issue further.

In the meantime, it is worth noting that Hsiao Tse-Chiang and coworkers (10) have reported on central plume velocities and free surface velocities in a water model of a 7 ton steel ladle at various gas flow rates. These velocities were measured by means of a precalibrated drag probe from a knowledge of standard drag coefficients and probe dimensions. From these measurements, the average plume velocity was calculated to be

Table 2.8 Influence of various parameters in equation (2.18) on predicted maximum penetration depths of a mildly buoyant sphere (viz., Fig. 2.1) and their comparison with those measured experimentally.

Specification of the model	Predicted maximum penetration depths, m	Average Experimentally measured maximum penetration depths, m
Reduced fluid density in the plume; standard C_D	0.151	0.24
Reduced fluid density and viscosity in the plume; standard C_D	0.153	
Reduced fluid density and viscosity in the plume; 50 pct. of standard C_D in the plume	0.275	
Reduced fluid density and viscosity in the plume; standard C_D, accounting for the effect of turbulence intensity on drag coefficients	0.15	

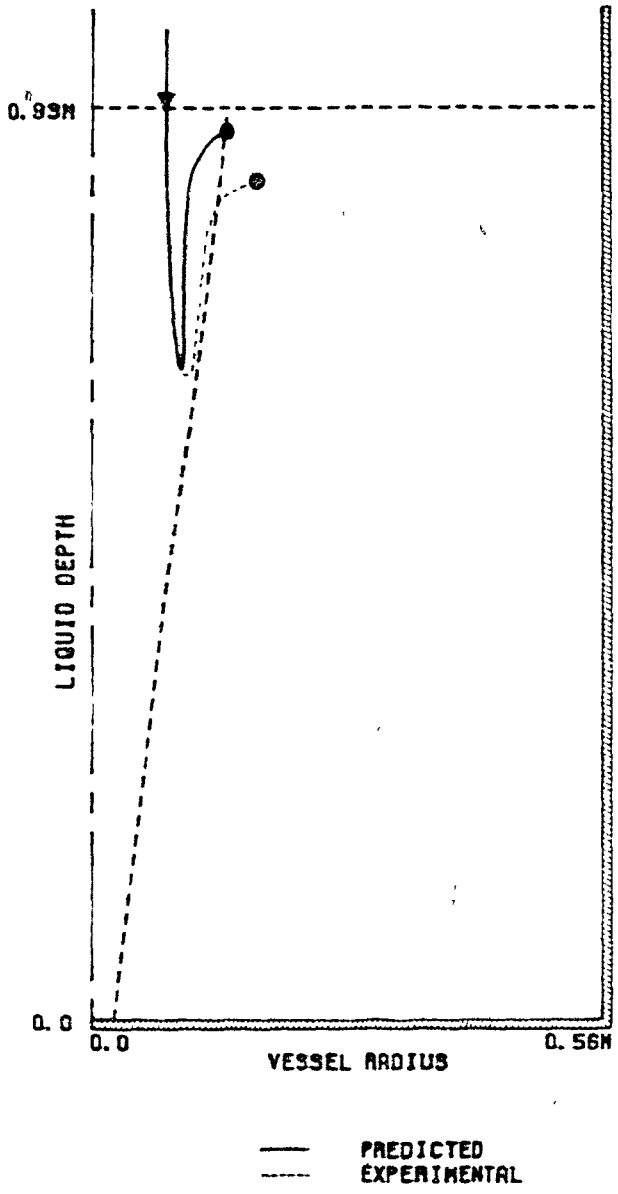

Figure 2.6 Predicted trajectory of the buoyant sphere in Fig. 2.1 taking a 50 pct. reduced value of drag coefficient in the two-phase region.

proportional to (gas flow rate)$^{0.24}$, while the near surface velocity in the one phase region of the flow was found to be proportional to (gas flow rate)$^{0.33}$. However, Sahai and Guthrie (7) have demonstrated theoretically and experimentally that plume velocities increase according to the third power of the gas flowrate, when recirculating flow is induced in a confined body of liquid. Consequently, in view of the present study, it appears that the empirical relationship (i.e., plume velocity proportional to (gas flow rate)$^{0.24}$), as reported by Hsiao Tse-Chiang and coworkers (10), may have resulted from an overestimation of drag coefficient in the two phase plume region, and as a result, too low a dependence of plume velocity on flow rate.

It therefore appears that the presence of many small bubbles (< 5 mm dia.) in the vicinity of a much larger sphere ($\sim$ 25 mm dia.) can act to uncouple the solid sphere from the liquid and cause a reduction in drag forces. Such uncoupling can be expected to be related to the number of bubbles and bubble sizes etc., in the medium, which in turn will be dependant on gas flowrates and the physical properties of the gas and the liquid.

In the absence of liquid flow, maximum bubble sizes observed were around 15-20 mm in diameter. However, when cocurrent streams of gas and liquid were introduced, maximum bubble sizes were observed to be no more than 5 mm in diameter

($U_B \sim 0.12$ m/s). A range of bubble sizes existed for all experiments.

B. Trajectories of Spherical Additions in Gas Stirred Ladles: Reproducibility of measured particle trajectories in the water model

The reproducibility of particle trajectories was found to be reasonably consistent, except those observed for the sphere with a specific gravity 0.991. Several factors may be considered to affect the stochastic nature of the latter's trajectories. It is to be recognised that such a sphere, with a specific gravity of 0.991, can be considered to be essentially neutrally buoyant. Consequently, dynamic instabilities in the flow (i.e., turbulence, etc.) particularly in the gas-liquid region, can affect the trajectory of such particles considerably. Thus, although the essential features of the flow hardly changed with time, careful observation revealed the existence of considerable instabilities in the vicinity of the bubble plume. These are presumably due to the complex nature of such buoyancy driven plumes.

Another possible effect explaining this scatter in particle trajectories, could be the marginal differences in the precise entry location of the particles. Even though the particle holder together with its release mechanism, was fixed to the desired point above the recirculating bath, the location of particle entry varied slightly from run to run. The maximum

observed deviation at entry was 20 mm, and normally much less. However, it is to be mentioned here that the velocity gradient in the vicinity of the bubble plume in such a system is very steep, and consequently such variation in entry point may be quite critical for the trajectories of such neutrally buoyant particles. This scatter in the trajectory of a particle with specific gravity 0.991 has been shown in Fig. 2.7.

Particle trajectories in the C.A.S. system

Figures 2.8 to 2.11 show the predicted trajectories of the four different spheres (viz., Table 2.2) based on the numerical solution of the governing differential equation. Also shown in those figures are the experimentally measured trajectories. In spite of the irregular shape and complex geometry of a real bubble plume, there is very close agreement between the observed and predicted trajectories. Furthermore, it is readily seen that using a 50 pct. reduced drag coefficient in the two phase region, in the computational scheme allows maximum penetration depths predicted to fall much closer to those observed.

Predicted and observed trajectories of extremely buoyant particles (sp. gr. = 0.4 and 0.6), as shown in Figs. 2.8 and 2.9, clearly show the extent to which they penetrate into the bath (typically 80-120 mm). As a consequence, the total immersion times of such particles are extremely small (about 0.5 seconds). This shows that although there is a strong downward flow in the vicinity of the central plexiglass cylinder, there

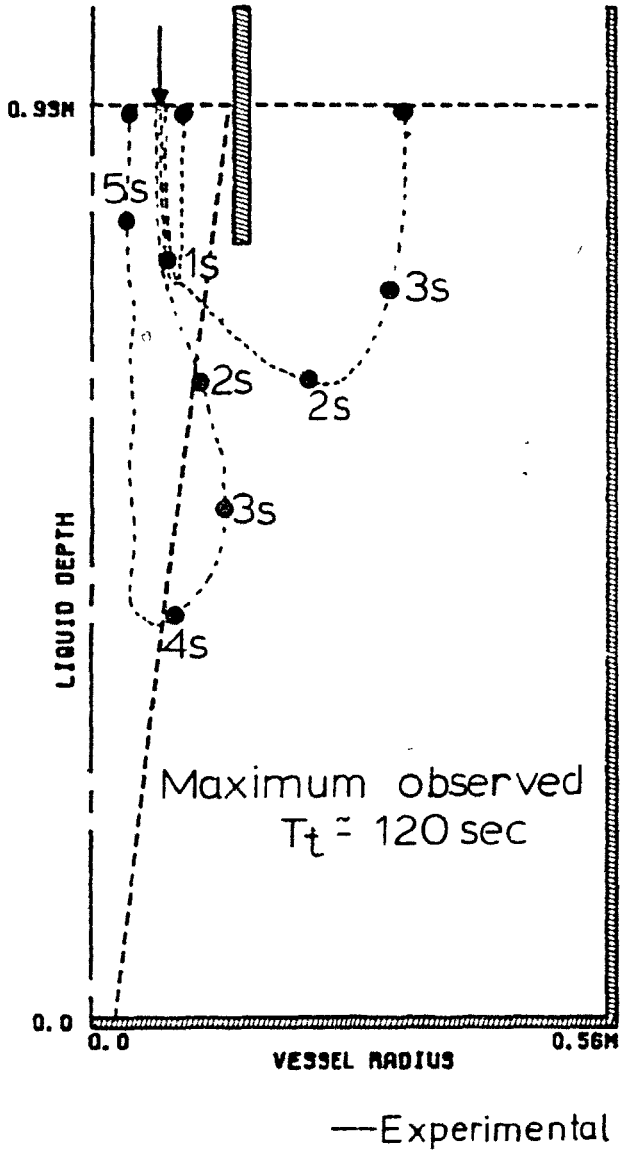

Figure 2.7 Experimental trajectories observed for mildly buoyant spheres (ρ_p = 991 Kg/m^3), illustrating the extent of scatter in successive trajectories.

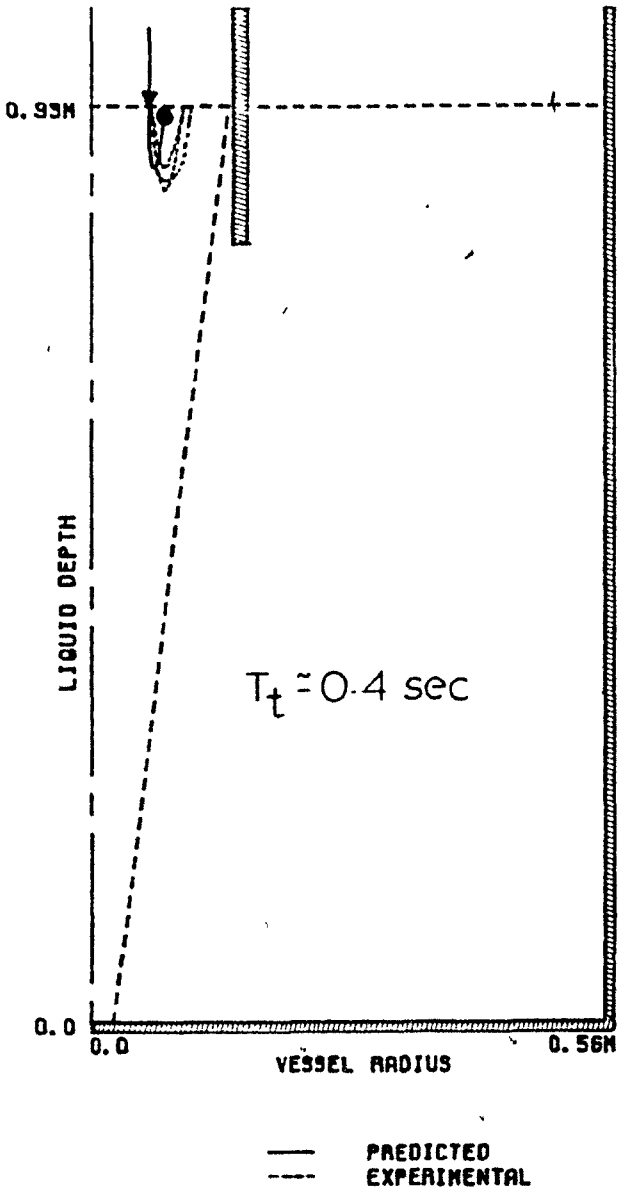

Figure 2.8 Predicted and experimental trajectory of a buoyant sphere (ρ_p = 400 Kg/m^3) during water model simulation of the C.A.S. method of alloy addition (U_{entry} = 2 m/sec).

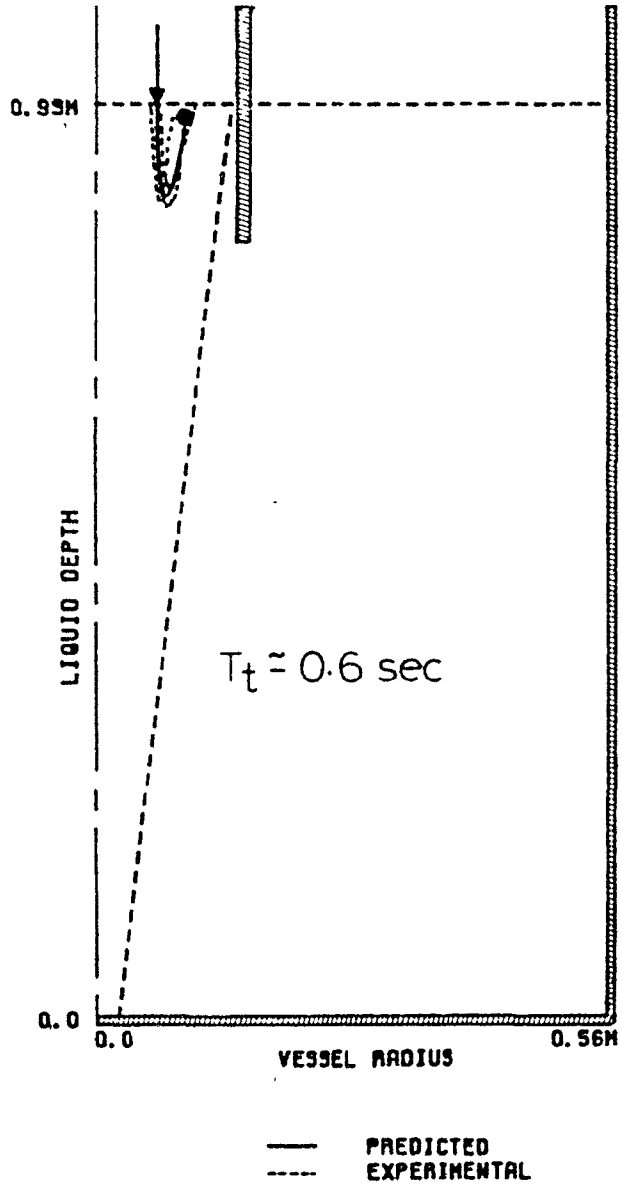

Figure 2.9 Predicted and experimental trajectory of a buoyant sphere (ρ_p = 600 Kg/m^3) during water model simulation of the C.A.S. method of alloy addition (U_{entry} = 2.0 m/sec).

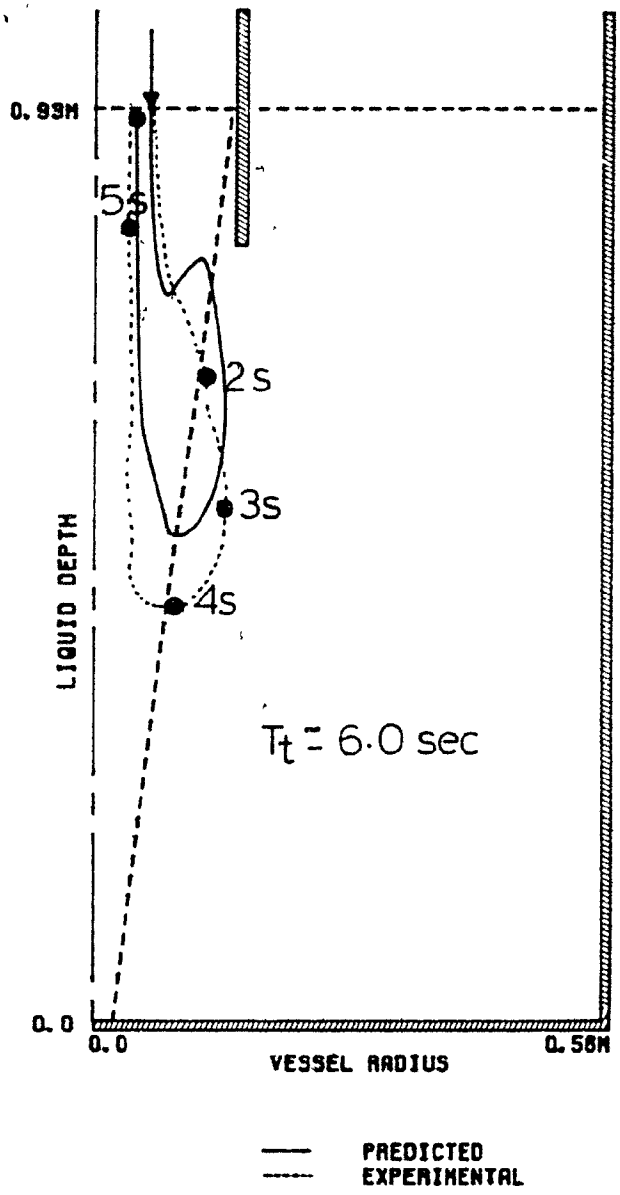

Figure 2.10 Predicted and experimental trajectory of a buoyant sphere (ρ_p = 991 Kg/m^3) during water model simulation of the C.A.S. method of alloy addition (U_{entry} = 2.0 m/sec).

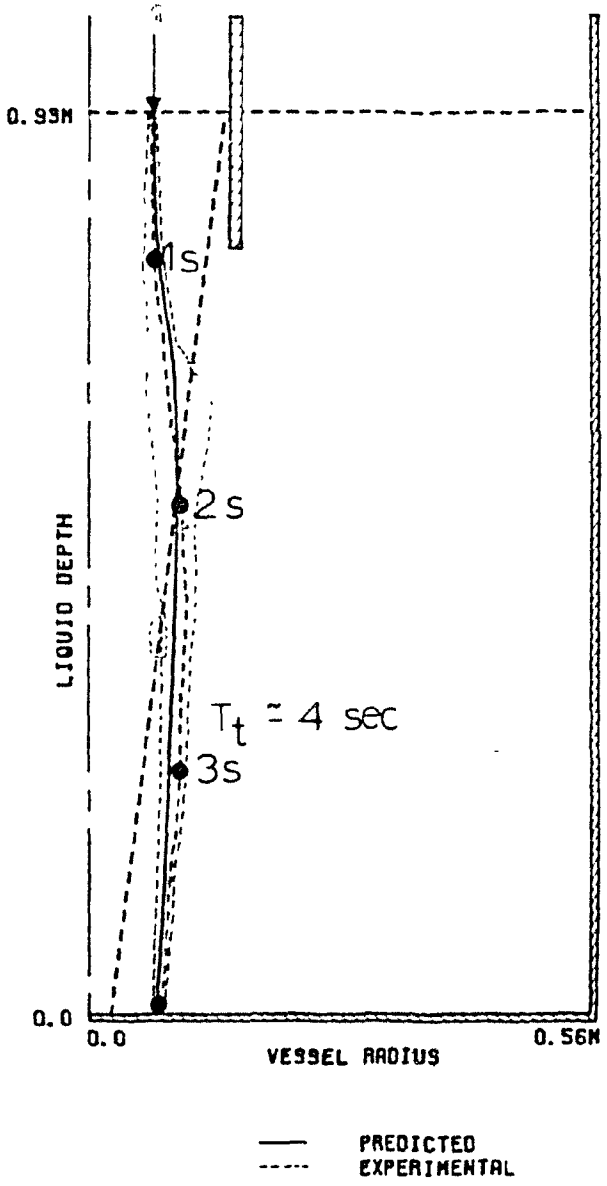

Figure 2.11 Predicted and experimental trajectory of a dense sphere (ρ_p = 1140 Kg/m^3) during water model simulation of the C.A.S. method of alloy addition (U_{entry} = 2.0 m/sec).

is practically no chance that such particles could be entrained and undergo, as a result, prolonged subsurface motion.

On the other hand, the sphere with a specific gravity 0.991 was predicted to penetrate much more deeply (about 250 to 290 mm) and only then be carried upwards by the rising action of the plume (see Fig. 2.10). Following this, the particle was again predicted to be entrained into the bulk by the downflowing liquid in the vicinity of the central plexiglass cylinder wall. Furthermore, it has been observed experimentally that such particles are usually caught up in the narrow recirculating vortex associated with the plume and consequently can undergo prolonged subsurface motion. Nevertheless, ultimately such particles will tend to fall out of this narrow vortex into the main bulk where they can gradually float up to the free surface.

Contrary to all the above additions, heavier particles (sp. gr. = 1.14) were always observed to settle to the bottom of the tank (see Fig. 2.11).

Particle trajectories in conventional ladle stirring operations

Using the same equipment and procedures, trajectories of the four different spheres were also observed in the conventional gas injection configuration and equivalent numerical predictions made. The spheres were dropped from a height 0.75 m to give an entry velocity of about 3.83 m/s. Observed and predicted trajectories are shown in Figs. 2.12 to 2.15. As seen very reasonable agreement between predictions and measurements

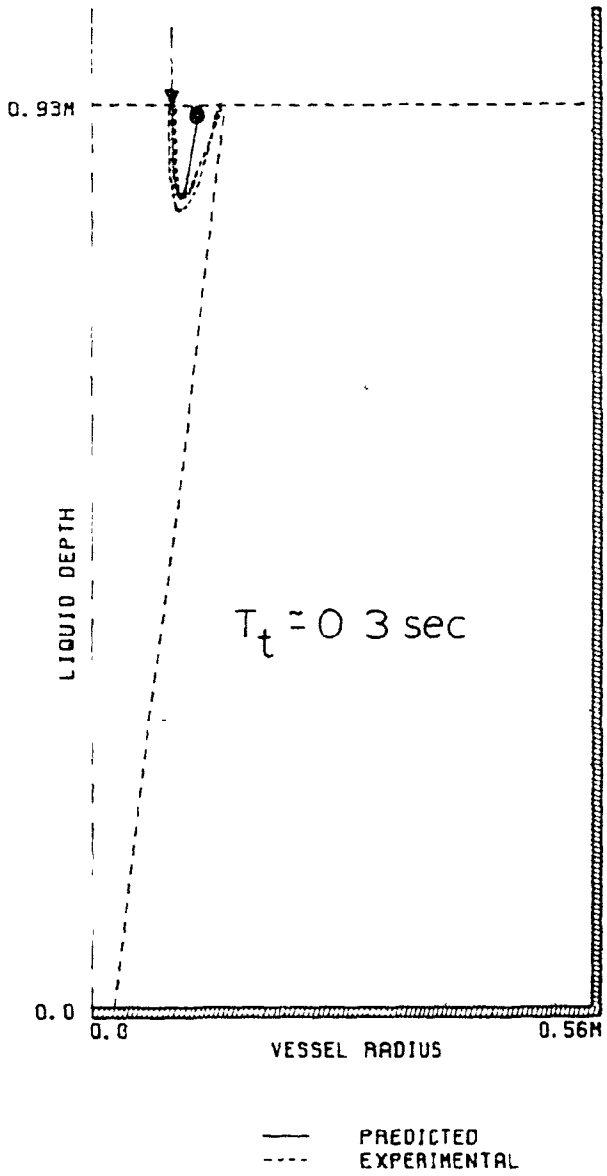

Figure 2.12 Predicted and experimental trajectory of a buoyant sphere (Sp. gr. = 0.4) during water model simulation of conventional gas stirring for a particle entry velocity of 3.83 m/sec.

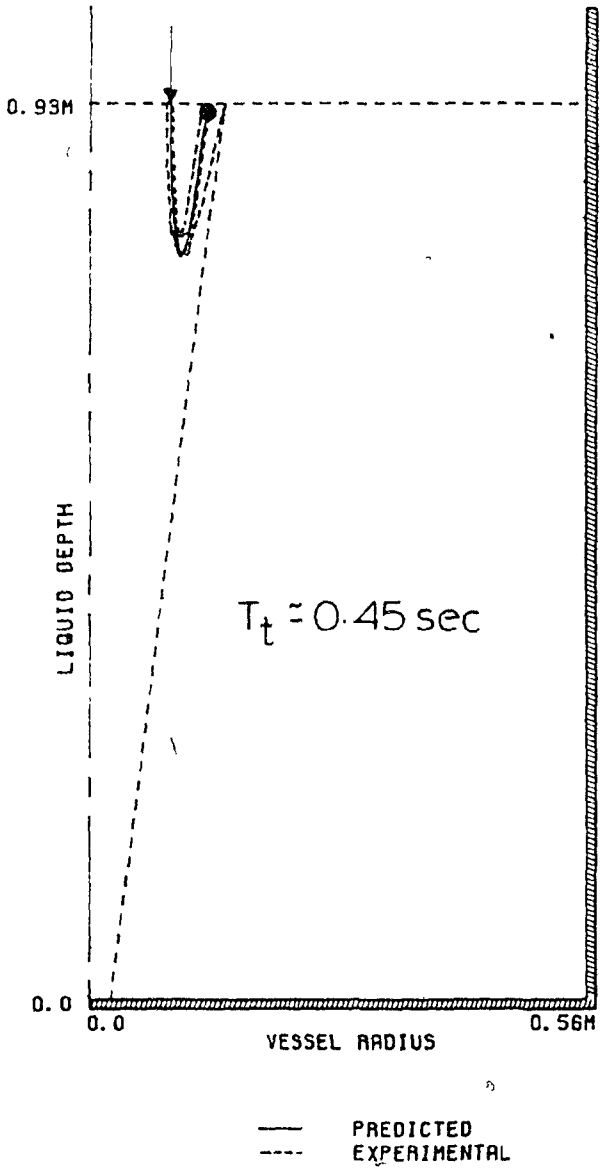

Figure 2.13 Predicted and experimental trajectory of a buoyant sphere (Sp. gr. = 0.6) during water model simulation of conventional gas stirring for a particle entry velocity of 3.83 m/sec.

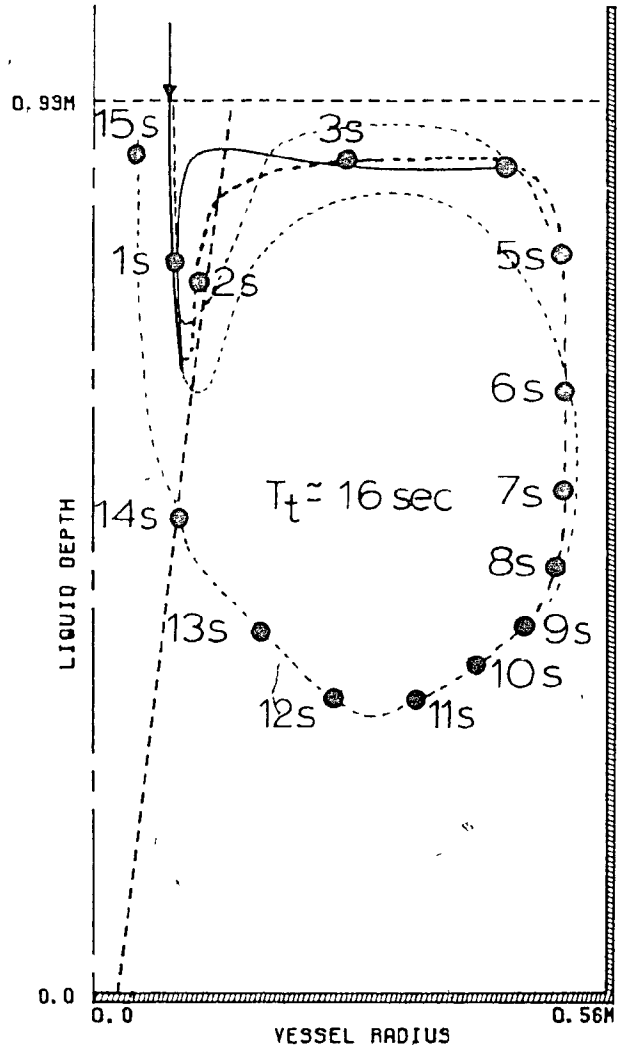

Figure 2.14 Predicted and experimental trajectory of a buoyant sphere (Sp. gr. = 0.991) during water model simulation of conventional gas stirring for a particle entry velocity of 3.83 m/sec.

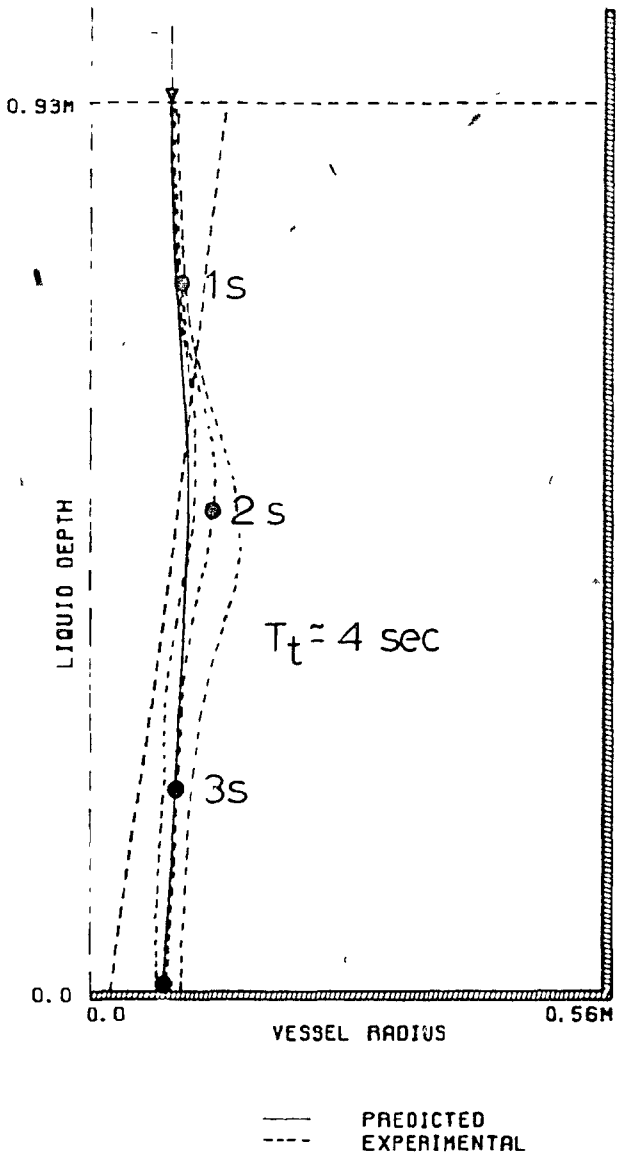

Figure 2.15 Predicted and experimental trajectory of a dense sphere (Sp. gr. = 1.14) during water model simulation of conventional gas stirring for a particle entry velocity of 3.83 m/sec.

was again achieved. These figures however reflect the following features. Extremely buoyant particles (sp. gr. = 0.4 and 0.6) will not penetrate the liquid very much at all, and almost instantaneously resurface. Neutrally buoyant particles (sp. gr. = 0.991), on the other hand will penetrate much deeper and consequently can be expected to undergo subsurface motion for prolonged periods of time. Heavier particles (sp. gr. = 1.14) will, nevertheless, always settle to the bottom of the tank.

C. Industrial Applications

The direct observation of such addition making operations in industrial size vessels, where high temperature (e.g., 1600°C) and visual opacity pose serious experimental problems, would seem impractical based on present day technology. Furthermore, the hydrodynamic and thermal phenomena taking place in such steel processing units are extremely complex and interrelated (e.g., the chilling of a steel shell around the solid addition, partial melting of the encased alloy, heat convection and buoyancy effects etc.). Nonetheless a basic understanding of the fluid dynamic aspects of such addition making operations can be developed by extrapolating the present mathematical model beyond its experimentally validated limits of vessel size, particle size and density, liquid etc., to predict alloy trajectories in full scale vessels.

Furthermore, as mentioned previously, model experiments on particles' trajectories provide only semi-quantitative results

in most cases. Therefore, predictions of particles' trajectories for a full scale system based on such mathematical model improves the quantitative information on expected trajectories. Since there was no experimental data on flow fields available for this application, the predicted flow fields established in an industrial size 150 ton ladle were used.

As a typical example of the model's capabilities in this respect, predicted trajectories of four spherical additions (85 mm diameter) (Al, FeSi, FeMn and FeNb) in a 150 ton ladle during C.A.S. operation have been illustrated in Fig. 2.16. As seen the general appearance of these trajectories is quite similar to those presented in Figs. 2.8 to 2.11, indicating the effectiveness of the model study program and also the computer predictions.

Predicted trajectories of spherical additions during conventional gas injection into a 150 ton steel processing ladle is shown in Fig. 2.17. Once again, very similar trajectories to those observed in the water model (Figs. 2.12 to 2.15) are readily apparent.

Although the formation of a steel shell around the solid additions would change its apparent density (11), and the dynamic nature of multiparticle addition may be slightly different from single particle addition (5), it is clear that buoyant additions such as aluminium and ferrosilicon, would proceed to melt within the central slag free region under inert atmosphere.

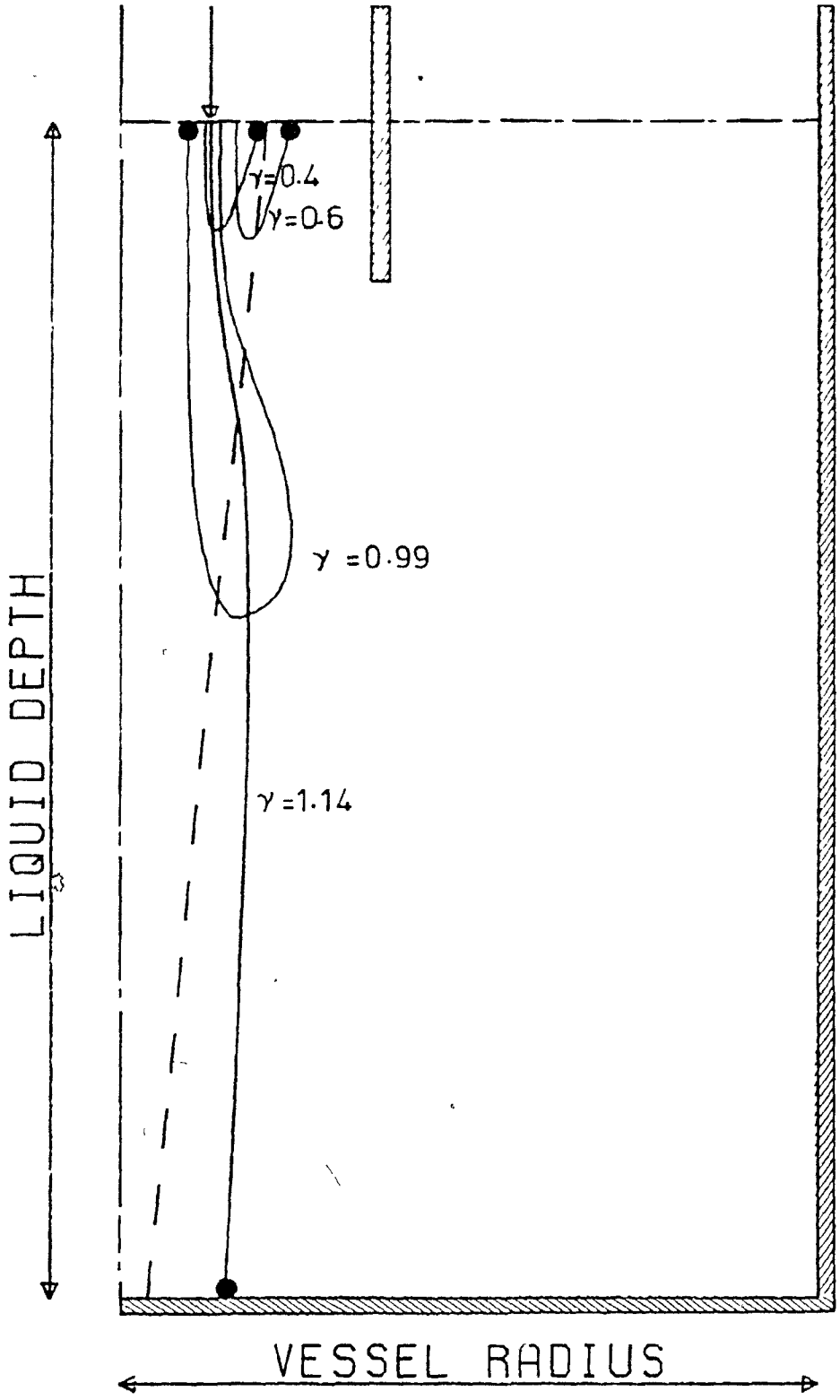

Figure 2.16 Predicted trajectories of spherical alloy additions (Table 2.3) to a 150 ton ladle during the C.A.S. alloy addition procedure (Q = 0.0188 m^3/s).

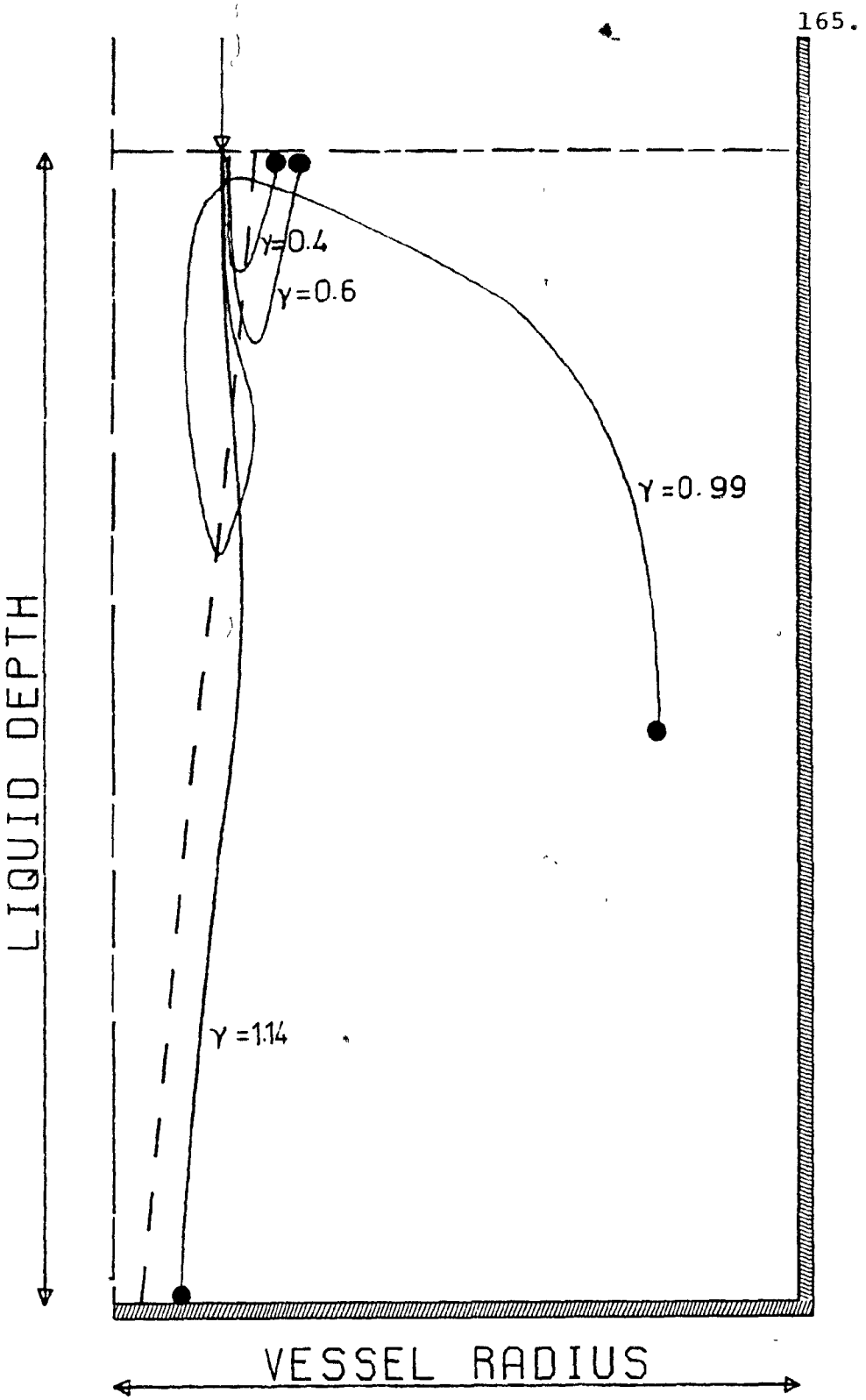

Figure 2.17 Predicted trajectories of spherical alloy additions (Table 2.3) to a 150 ton ladle during conventional gas injection procedures (Q = 0.0188 m^3/s).

Thus on the basis of information provided in Part I and Part III, it can be concluded that such additions would melt and be dispersed homogeneously into the bulk of the liquid, before having any chance to react with the slag.

Ferromanganese (density = 6980 kg/m^3), on the other hand, may undergo subsurface melting, or may fall out of the primary recirculating loop into the bulk and then gradually float up to the slag metal interface. If the alloys' content is released from within the steel shell in the vicinity of the slag metal interface, it is clear that a portion will react with any oxidising slag present. Heavier additions, such as ferroniobium, will settle to the bottom and only then gradually melt and be dispersed. However, since the bottom part of the ladles' contents is relatively quiescent, such additions will experience considerably longer ladle mixing times.

The trajectories of spherical additions shown in Figs. 2.16 and 2.17, clearly demonstrate the effectiveness of the C.A.S. method over any conventional gas injection procedure, as a technique for introducing buoyant additions. As seen from Fig. 2.17, aluminium and ferrosilicon dropped into a gas stirred steel bath would immediately float up to the slag metal interface. In view of their affinity for oxygen, being strong deoxidisers in steel, both would typically be largely consumed by any oxidising slag, rather than being dispersed into the bulk of liquid steel.

CONCLUSIONS

The motions of spherical shaped particles in gas stirred ladles have been investigated. It has been shown that gas-liquid dispersions can cause some reduction in drag during the particle's motion through an upwelling gas-liquid mixture. Based on Newton's law of motion for such a system, the trajectories of spherical particles of different densities were predicted and compared with those derived from water model experiments. Very reasonable agreement between measurements and predictions was achieved.

Trajectories of spherical particles of various densities ($d_p \sim 85$ mm) were also predicted for an industrial size 150 ton ladle, and their technological significance discussed.

LIST OF SYMBOLS

A_t	Cross sectional area of the column, m^2
C_A	Added mass coefficient
C_D	Drag coefficient
$C_{D,S}$	Standard drag coefficient
$C_{D,Gas}$	Drag coefficient measured in a gas-liquid dispersion
C_H	Coefficient in the Basset history integral term
d_p	Diameter of particle, (= $2R_p$), m
$d_{p,m}$	Diameter of particle in the model, m
$d_{p,f.s}$	Diameter of particle in the full scale system, m
F_A	Added mass force, Newton
F_B	Buoyancy force, Newton
F_D	Drag force, Newton
F_g	Gravity force, Newton
g	Acceleration due to gravity, m/sec^2
$H_{f,m}$	Height of fall in the model, m
$H_{f,f.s}$	Height of fall in the full scale system, m
M_S	Mass of sphere, kg
M_A	Apparent or added mass, kg
Q_g	Volumetric flow-rate of gas, m^3/sec
Q_l	Volumetric flow-rate of liquid, m^3/sec
r	Radial coordinate, m
r_{entry}	Entry point of the particle on the radial axis, m
U_p	Velocity of particle, m
u_p	Velocity of particle in the vertical direction, m/s

U_r Relative velocity between particle and fluid, m

U_l Liquid velocity, m/sec

U_{mix} Gas-liquid mixture velocity, m/sec

U_{ol} Superficial velocity of liquid, m/sec

U_{og} Superficial velocity of gas, m/sec

U_B Rise velocity of a single bubble in a quiescent liquid, m/sec

U_f Fluid velocity, m/sec

U_{entry} Vertical entry velocity of the particle, m/sec

$U_{entry,m}$ Vertical entry velocity of the particle in the model, m/sec

V_{entry} Horizontal entry velocity of particle, m/sec

v_ρ Velocity of particle in the horizontal direction, m/s

v_p Horizontal velocity of particle, m/sec

t Time, sec

T_t Total time, to settle to the bottom or to resurface, sec

X Distance, m

z The axial or the vertical direction, m

ρ Density, kg/m^3

ρ_ℓ Liquid density, kg/m^3

ρ_{mix} Gas-liquid mixture density, kg/m^3

ρ_p Particle density, kg/m^3

ρ_G Gas density, kg/m^3

λ Geometrical scaling factor, $(= L_m/L_{f.s})$

α Volume fraction of gas in the plume

ν Particle-liquid density ratio

μ_ℓ , μ Dynamic viscosity of the liquid, kg/(m-s)

REFERENCES

1. K. Takashima, K. Arima, T. Shozi and H. Mori: 'Method for Treatment of Molten Steel in a Ladle' - U.S. Patent, No. 3971655, 1976.

2. C.L. Trout, D.L. Paterson and S.M. Hughes: AISE Conference Proceeding, Pittsburg, Pennsylvania, 1983.

3. R.J. Brodkey: "The Phenomena of Fluid Motions", Addison-Wisley, Reading, Massachusetts, 1967.

4. R.I.L. Guthrie, R. Clift and H. Henein: Metall. Trans., Vol. 6B, pp. 321-329, 1975.

5. M. Tanaka: Ph.D. Thesis, Department of Mining and Metallurgy, McGill University, August 1979.

6. A. May: NAVSEA Hydroballastics Advisory Committee Technical Report 75-2, SEAHAC/TR75-2, 1975.

7. Y. Sahai and R.I.L. Guthrie: Metall. Trans., Vol. 13B, pp. 193-202, 1982.

8. C.E. Lapple and D.E. Shepherd: Ind. Engg. Chem., Vol. 32, pp. 605, 1940.

9. C. Colman and W.H. Gauvin: Journal A.I. Ch.E., Vol. 15, pp. 184-189, 1969.

10. Hsiao Tse-Chiang, T. Lehner and B. Kjellberg: Scandinavian Journal of Metallurgy, Vol. 9, pp. 105-110, 1980.

11. R.I.L. Guthrie: Electric Furnace Proceedings, pp. 30-40, 1977.

LIST OF FIGURES

Figure 2.10 Predicted and experimental trajectory of a buoyant sphere (ρ_p = 991 Kg/m^3) during water model simulation of the C.A.S. method of alloy addition (U_{entry} = 2.0 m/sec).

Figure 2.11 Predicted and experimental trajectory of a dense sphere (ρ_p = 1140 Kg/m^3) during water model simulation of the C.A.S. method of alloy addition (U_{entry} = 2.0 m/sec).

Figure 2.12 Predicted and experimental trajectory of a buoyant sphere (Sp. gr. = 0.4) during water model simulation of conventional gas stirring for a particle entry velocity of 3.83 m/sec.

Figure 2.13 Predicted and experimental trajectory of a buoyant sphere (Sp. gr. = 0.6) during water model simulation of conventional gas stirring for a particle entry velocity of 3.83 m/sec.

Figure 2.14 Predicted and experimental trajectory of a buoyant sphere (Sp. gr. = 0.991) during water model simulation of conventional gas stirring for a particle entry velocity of 3.83 m/sec.

Figure 2.15 Predicted and experimental trajectory of a dense sphere (Sp. gr. = 1.14) during water model simulation of conventional gas stirring for a particle entry velocity of 3.83 m/sec.

Figure 2.16 Predicted trajectories of spherical alloy additions (Table 2.3) to a 150 ton ladle during the C.A.S. alloy addition procedure (Q = 0.0188 m^3/s).

Figure 2.17 Predicted trajectories of spherical alloy additions (Table 2.3) to a 150 ton ladle during conventional gas injection procedures (Q = 0.0188 m^3/s).

LIST OF TABLES

PART III

LIQUID MIXING IN LADLE METALLURGY OPERATIONS

ABSTRACT

The mixing of liquids in ladles, agitated by a centrally rising bubble plume, has been analysed both theoretically and experimentally. It is shown that mixing is a combination of both convection and diffusion and that neither can be disregarded in gas stirred systems. However, for predicting mixing times in such gas injection operations, one can use a simplified empirical correlation based on diffusive mixing in which $T_m \propto \dot{\varepsilon}_m^{-1/3} \; L^{-1} \; R^{5/3}$, where T_m is the mixing time, $\dot{\varepsilon}_m$ is the specific energy input rate, R is the vessel radius and L is the liquid depth.

The rate of liquid mixing in C.A.S. operation has also been analysed both theoretically and experimentally. It is shown that mixing times are considerably longer and less sensitive to gas flow rates than those deriving from conventional ladle stirring practices. The relative performance characteristics of the algebraic model versus the k - ε model of turbulence is also discussed.

INTRODUCTION

The intrinsic efficiencies of many chemical processing operations carried out in present day steelmaking ladles are intricately related to the nature of fluid flow and mixing. An inexpensive method for promoting mixing in such liquid metal holding vessels is by gas injection through a porous plug, submerged lance, or nozzle. The gas, rising as a plume to the surface through liquid steel, induces a recirculatory flow of fluid, which in addition to controlling the rate of dispersion and homogenisation of additions, may aid inclusion agglomeration and float-out. In the absence of such bath agitation, chemical/thermal and/or particulate inhomogeneities can originate. This, in turn, sometimes induces unacceptable variabilities in the final product.

In the chemical and metallurgical processing industries, mixing is usually expressed in terms of a mixing time needed to achieve a given homeogeneity. Commonly appearing factors for evaluating the mixing time, or the degree of mixing, are the mixing power density, $\dot{\varepsilon}_v$, (i.e., the rate of energy input per unit volume) and the specific energy input rate, $\dot{\varepsilon}_m$ (i.e., the rate of energy input per unit mass). In order to estimate the degree of liquid metal mixing in such refining vessels, several investigators (1,2,3) have recently addressed the problem, and explicit empirical mixing time relationships of the

type $T_m = k \dot{\varepsilon}_v^{-n}$ have been proposed for axisymmetrically agitated gas stirred melts.

Nonetheless, one can adopt a more fundamental approach, and address the phenomenon of liquid mixing from a purely theoretical view point through consideration of the relevant partial differential equations describing such phenomena. In a recirculating flow system such as the one under consideration, the dispersion of a tracer added within the vessel is expected to be governed by the combined phenomena of convection and turbulent diffusion. Consequently, the usual approach would be to solve the unsteady, convection + diffusion equation, with an appropriate set of boundary conditions. Needless to say, such solutions require prior specification of flow and turbulence characteristics within the system as a starting point.

This latter approach was adopted by Szekely and coworkers (3) who, through numerical solution of governing differential equations (i.e., the equations of continuity, motion and turbulence together with mass conservation), predicted mixing times in pilot scale and industrial size argon stirred ladles. Furthermore, mixing times thus calculated were found to be in good agreement with experimentally measured mixing times. Nevertheless, it is to be stressed here that this approach, while very attractive, entails a major computational task and can be justified only for problems which require detailed information about the nature and structure of the flow.

In the present author's efforts to predict rates of homogenisation of alloy additions in various axisymmetric gas injection procedures, a two stage approach is adopted for describing mixing. In the first part, the fundamental equations are solved to give the time - dependant concentration fields. In the second part, these fields are then used to formulate and tune an empirical model for predicting mixing times. This can be justified since recirculatory flow fields in these systems have already been predicted with reasonable degrees of certainty. Consequently, on the basis of experiments conducted in reduced scale water models, and detailed theoretical analysis of the governing differential equations, the resulting macroscopic model for predicting liquid mixing during central gas injection into ladles provide an effective yet simple, way for predicting mixing times in larger size steel processing vessels.

THEORY

A. Mathematical Formulation

The differential model of addition dispersion

In the presence of a velocity field U, the conservation of m_i is expressed as:

$$\frac{\partial}{\partial t}(\rho m_i) + \text{div}\,|(\rho U m_i) + J_i| = R_i \qquad (3.1)$$

Here, $\frac{\partial}{\partial t}(\rho m_i)$ denotes the rate of change of mass of the chemical species i per unit volume (m_i being the mass fraction of the species i, defined as the ratio of the mass of the species i contained in a given volume to the total mass of the mixture contained in the same volume). The quantity $\rho u m_i$ is the convective flux of the species 'i' while J_i denotes its diffusive flux. Diffusive fluxes are normally caused by gradients in m_i, and can be expressed as $J_i = -\Gamma \text{ grad } (m_i)$, where Γ is an effective exchange coefficient ($=\rho D_e$). The quantity R_i on the right hand side represents the rate of generation, (if any), of the chemical species 'i' per unit volume.

For a two-dimensional situation with no generation, equation (3.1) can be written in terms of cylindrical polar coordinates as

$$\frac{\partial}{\partial t}(\rho m_i) + \frac{\partial}{\partial z}(\rho u m_i) + \frac{1}{r}\frac{\partial}{\partial r}(\rho r v m_i) = \frac{\partial}{\partial z}\left(\Gamma \frac{\partial m_i}{\partial z}\right) + \frac{1}{r}\frac{\partial}{\partial r}\left(r\Gamma \frac{\partial m_i}{\partial r}\right) \qquad (3.2)$$

Assuming that the eddy diffusivity, D_e (= Γ/ρ), and the eddy kinematic viscosity ν_t (= μ_e/ρ) are numerically equal, since they both derive from the phenomenon of turbulent fluctuations, then the effective exchange coefficient can either be approximated from an effective viscosity formula proposed by Sahai and Guthrie (4) or from a more advanced two equation turbulence model (5). Because of the coupling of equation (3.2) with the flow and turbulence models, it is assumed that the distribution of flow and turbulence parameters within the system is known.

The boundary conditions

The boundary conditions required for the solution of equation (3.2) has to express the physical constrains that all the bounding surfaces (viz., walls, free surface and symmetry axis) are impervious to the additions. In a mathematical sense this corresponds to a zero concentration gradient at all the bounding surfaces i.e.,

(i) at the axis of symmetry, $\frac{\partial m_i}{\partial r} = 0$

(ii) at the free surface of liquid, $\frac{\partial m_i}{\partial z} = 0$ and

(iii) at the sidewalls and bottom surface, $\frac{\partial m_i}{\partial r}\Big|_{r=R} = 0$ and $\frac{\partial m_i}{\partial z}\Big|_{z=0} = 0$

In addition to this the initial condition employed for equation (3.2) was

(iv) at $t = 0$, $m_i\ (I,J) = m_i^o$

where the array (I,J) denotes the region of tracer addition.

It was further assumed that the initial concentration m_i^o applied over the control-volume associated with grid region (I,J).

The algebraic models of addition dispersion

Since the given flow-fields satisfy continuity, equation (3.2) which is a statement of conservation of mass, can also be written in the form:

$$\frac{\partial m_i}{\partial t} + U \cdot \text{div } m_i = D_e \text{ div (grad } m_i) \qquad (3.3)$$

Now, if we assume that the dispersion of the tracer added to the system is predominantly governed by fluid convection, then equation (3.3) simplifies to

$$\frac{\partial m_i}{\partial t} = - U \cdot \text{div } m_i \qquad (3.4)$$

Alternatively, supposing the dispersion of tracer to be dominated by turbulent diffusion, equation (3.3) simplifies to:

$$\frac{\partial m_i}{\partial t} = D_e \text{ div (grad } m_i) \qquad (3.5)$$

Based on the theoretical arguments provided by Asai et al. (2), equations (3.4) and (3.5) can be further simplified to yield to the following relationship (2):

$$T_m \propto \frac{L_c}{\bar{U}} \tag{3.6}$$

for mixing predominantly controlled by fluid convection, and

$$T_m \propto \frac{L_c^2}{D_e} \tag{3.7}$$

for mixing dominated by turbulent diffusion.

Representing the characteristic velocity of the system by the average speed of liquid recirculation, $\bar{U}$, one can adopt the empirical relationship proposed by Sahai and Guthrie (6), for such bubble driven systems; i.e.,

$$\frac{\bar{U}}{U_p} (R^{1/3}) = \text{Constant} \tag{3.8}$$

Replacing the average plume velocity U_p, by the following relationship (see Part I)

$$U_p = K \frac{(\beta Q)^{1/3} \cdot L^{1/4}}{R^{1/3}} \tag{3.9}$$

one obtains the mean speed of liquid recirculation, $\bar{U}$, in terms of the operating variables, L, R, β and Q

$$\bar{U} \propto \frac{(\beta Q)^{1/3} \cdot L^{1/4}}{R^{2/3}} \tag{3.10}$$

Furthermore, denoting the characteristic length of the system, L_c, by the radius of the vessel, and then substituting $\bar{U}$ in equation (3.6) from equation (3.10), an explicit expression for mixing time as a function of vessel geometry, lance depth and gas flow rate results:

$$T_m \propto \frac{R^{5/3}}{(\beta Q)^{1/3} \cdot L^{1/4}} \qquad (3.11)$$

The turbulence kinematic viscosity, though strictly spatially dependant, can be conveniently represented as an average effective viscosity (4), according to

$$\nu_t = CL \left\{\frac{(1-\alpha) g \beta Q}{D}\right\}^{1/3} \qquad (3.12)$$

As the value of the eddy diffusivity, D_e, can be regarded as being as large as the eddy kinematic viscosity, D_e is readily deduced from equation (3.12) as

$$D_e \propto \frac{|\beta Q(1-\alpha)|^{1/3} \cdot L}{R^{1/3}} \qquad (3.13)$$

Substitution of D_e from equation (3.13) into equation (3.7), leads to an explicit relationship for mixing time in terms of operating variables; i.e.,

$$T_m \propto \frac{R^{7/3}}{|\beta Q(1-\alpha)|^{1/3} \cdot L} \qquad (3.14)$$

Consequently, for the two possible limiting situations of convective and diffusive mixing, mixing times for tracers added to gas agitated refining vessels (e.g., ladles) can be represented as:

$$\text{(i)} \quad T_m = C_1 \frac{R^{5/3}}{(\beta Q)^{1/3} \cdot L^{1/4}} \qquad (3.15)$$

for dispersion dominated by bulk circulation phenomena and

$$\text{(ii)} \quad T_m = C_2 \frac{R^{7/3}}{(\beta Q)^{1/3} \cdot L} \qquad (3.16)$$

for dispersion dominated by turbulent diffusion phenomena. Expecting gases to occupy 1 to 10 pct. of the upwelling gas-liquid mixture, $(1-\alpha)^{1/3}$ has been set equal to unity for the sake of convenience. However, one must now address the question as to which of these two transport mechanisms dominates liquid mixing in such systems. Also, once the principal transport mechanism has been identified, the constant C_1 or C_2 must be determined, so that mixing time can be stated explicitly in terms of L, R, β, Q and the constants of proportionality, C_1, and C_2, appearing in equations (3.15) and (3.16) respectively.

B. Calculation Procedure

Numerical procedure

The flow fields and the effective viscosity fields calculated in Part I of the thesis were used to solve the mass conservation equation (i.e., equation (3.2)). The transient term in the mass conservation equation was approximated by a fully implicit marching integration procedure, while for the representation of the total flux (i.e., convection + diffusion), a hybrid differencing scheme (7) was adapted. Equation (3.2) though a linear differential equation, was solved iteratively using a line by line solution scheme. A convergence criterion was set so that the absolute sum of residuals of m_i fell below 10^{-6}. About 12 to 16 iterations were required to satisfy this criterion.

EXPERIMENTAL WORK

Measurement of Mixing Times by Conductivity Measurement Technique

Mixing times were measured in two different cylindrical tanks, in which water was agitated by air, injected through a central vertical lance. Fig. 3.1(a) give an outline of the experimental set-up used for measuring mixing times. There a conductivity cell, made from a pair of platinised stainless steel electrodes recorded changes in the local concentration of a pulse tracer addition of 1N hydrochloric acid. This was made to the bath at point T in Fig. 3.1(a). The change in local ion concentration around the cell was measured through changes in the waters electrical conductivity, and recorded via a stripchart recorder. The recording of the tracer response was carried out until the concentration was considered to have attained the homogeneous concentration value. The analogue response curves (i.e., millivolt against time) thus obtained were used to evaluate mixing times. These are defined in the present context as the time required to allow the monitoring point concentration to continuously fall within a 5 pct. deviation band of the well mixed/homogeneous value. At least four measurements were made for each operating condition. It was found that maximum deviation in measured mixing times for each operating condition amounted to no more than 10 pct. (see Fig. 3.12). However, for the sake of convenience, an average mixing time was determined for each operation condi-

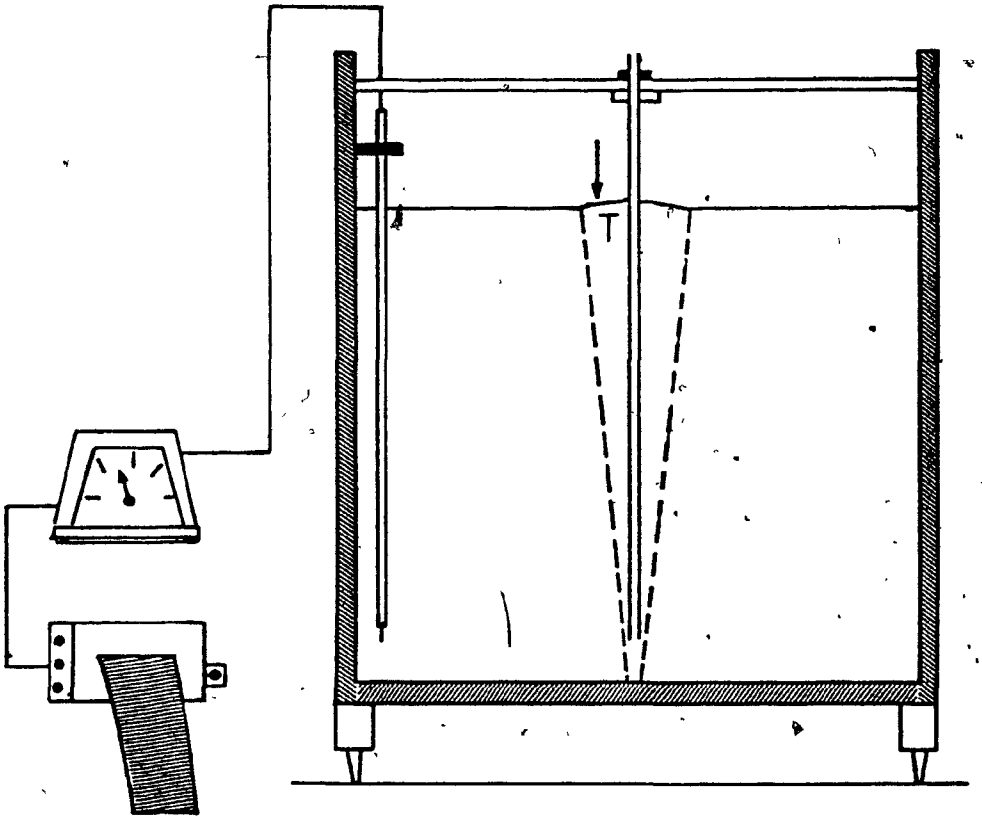

Figure 3.1(a) Schematic of the experimental set-up for measuring mixing times.

Figure 3.1(b) The electrode assembly

tion, and a linear regression analysis was carried out to make a straight line fit to the averaged points in Figs. 3.2, 3.3, 3.4 etc..

In addition to these measurements, the effect of a) monitoring point location, b) tracer addition sites, c) different types of electrodes and d) cell width (i.e., distance of separation between the electrodes) on mixing times were studied. The types of electrodes used and the cell width had practically no effect on measured mixing times. However, monitoring point and tracer addition location were found to be quite sensitive to measured mixing times. It was found that measurements made with the combination of tracer addition and monitoring point location of the type shown in Fig. 3.1(a) closely correspond to, and could be interpreted as the bulk mixing time. The implication of the term 'bulk mixing time' is discussed in the next section.

Although the tracer addition sites were essentially the same for all experiments (point T in Fig. 3.1(a)), a somewhat different location for the probe (i.e., point C in Fig. 3.9, which is different to that indicated in Fig. 3.1(a)) was used for measuring mixing times in the C.A.S. configuration. This is elaborated on in the text.

RESULTS AND DISCUSSION

A. Conventional Ladle Stirring

Mechanisms of addition mixing and an empirical model for mixing

Figure 3.2 shows the change in experimental mixing times as a function of $R^{7/3}/|\beta Q)^{1/3}L|$ and $R^{5/3}/|(\beta Q)^{1/3}\ L^{1/4}|$ respectively for a wide range of operating conditions and vessel geometry. As seen in Fig. 3.2(a) all the experimental data there can be described by a single straight line passing through the origin. There is practically zero scatter, while in Fig. 3.2(b), the scatter in data sets relative to the mean straight line happens to be significantly larger.

These figures suggest that experimentally observed mixing times can be described accurately via equation (3.16), and that mixing in such systems may be primarily related to eddy diffusion, rather than melt circulation, phenomena.

To test this hypothesis further, the governing differential equation (viz., equation (3.2)) for material mixing was re-solved numerically, by (i) retaining eddy diffusion terms and eliminating convection terms, i.e.,

$$\frac{\partial}{\partial t}\ (\rho m_i) = \frac{\partial}{\partial z}\ (\Gamma\ \frac{\partial m_i}{\partial z}) + \frac{1}{r}\ \frac{\partial}{\partial r}\ (r\Gamma\ \frac{\partial m_i}{\partial r}) \qquad (3.17)$$

and by (ii) retaining convection terms and eliminating eddy diffusion terms; i.e.,

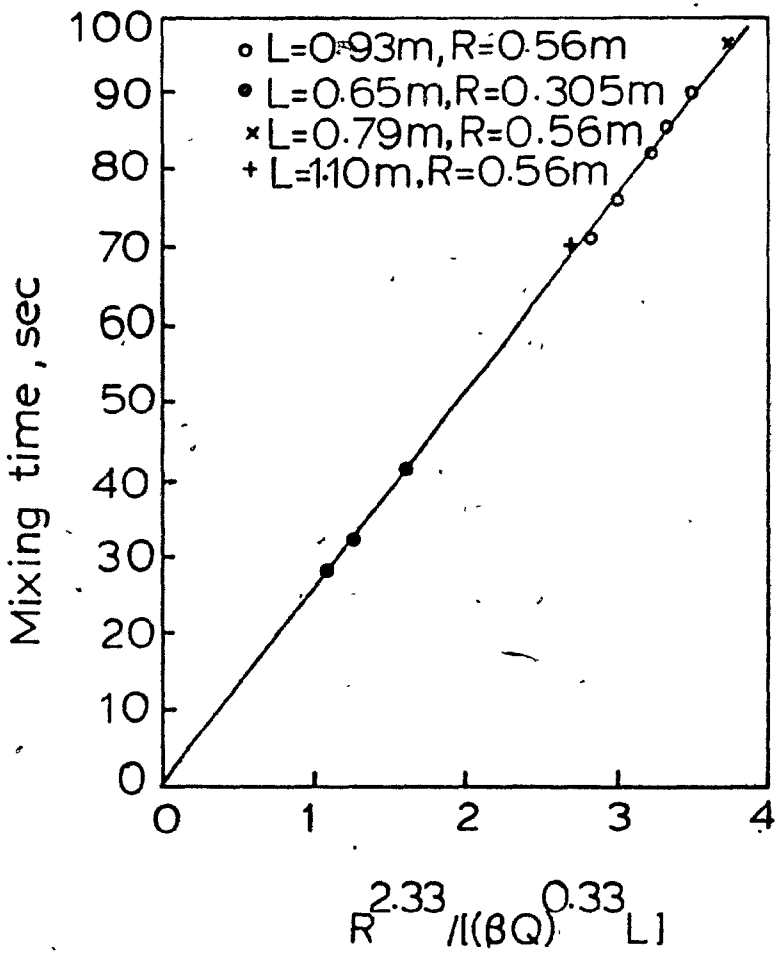

Figure 3.2(a) The dependence of mixing times T_m as a function of $R^{7/3}/|(\beta Q)^{1/3}.L|$ for various vessel geometries and gas flow rates.

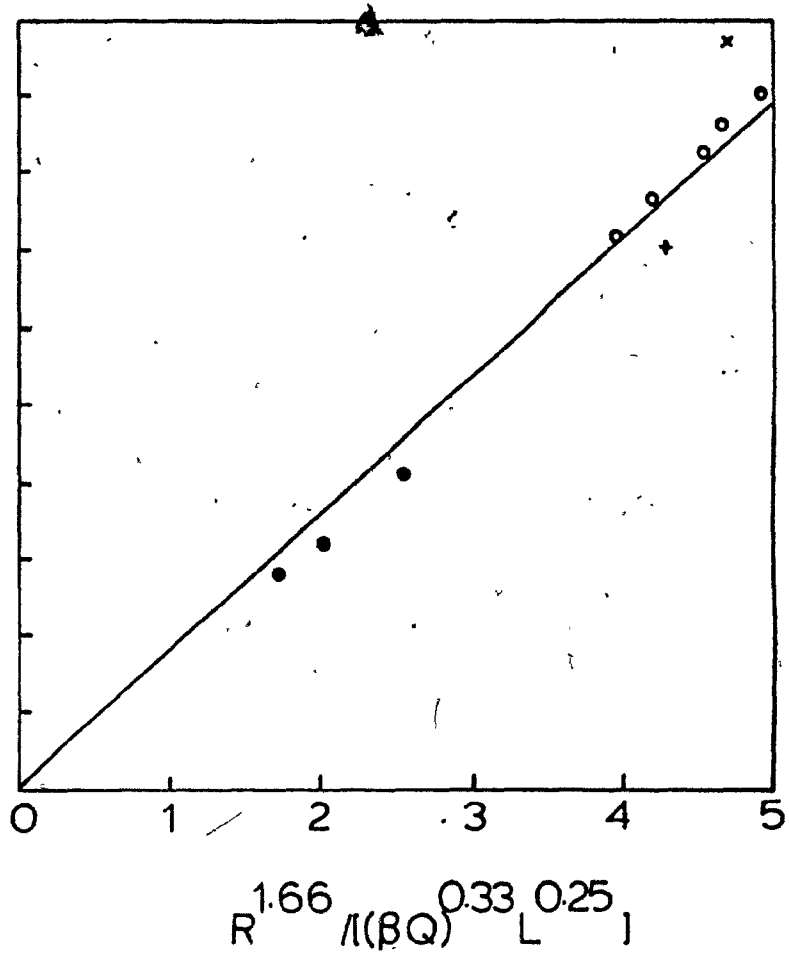

Figure 3.2(b) The dependence of mixing times T_m as a function of $R^{5/3}/|(\beta Q)^{1/3}.L^{1/4}|$ for various vessel geometries and gas flow rates.

$$\frac{\partial}{\partial t}(\rho m_i) + \frac{\partial}{\partial z}(\rho u m_i) + \frac{1}{r}\frac{\partial}{\partial r}(\rho r v m_i) = 0 \qquad (3.18)$$

Corresponding predictions for T_m for one of the two vessels studied (L = 0.93 m, R = 0.56 m), are illustrated in Figs. 3.3(a) and 3.3(b). As seen neither of these two equations (equations (3.17) and (3.18)) produce predictions which are close to experimental mixing time observations. Indeed solutions based on equations (3.17) and (3.18) predict mixing times that are both about an order of magnitude greater than those measured, whereas mixing time predictions incorporating both diffusion and convection (equation 3.2) produce quite realistic estimates, as seen from the same figures (i.e., Figs. 3.3(a) and 3.3(b)).

Consequently, although measured mixing times for a wide range of operating conditions and vessel geometry fall on a line

$$T_m \propto \frac{R^{7/3}}{(\beta Q)^{1/3} \cdot L} \qquad (3.19)$$

mixing times cannot be characterised solely in terms of either the two transport mechanisms. Previous investigators (1,2) have attempted to characterise mixing phenomena in terms of bulk convection and/or eddy diffusion mechanisms, while the present study clearly shows that mixing in such gas stirred

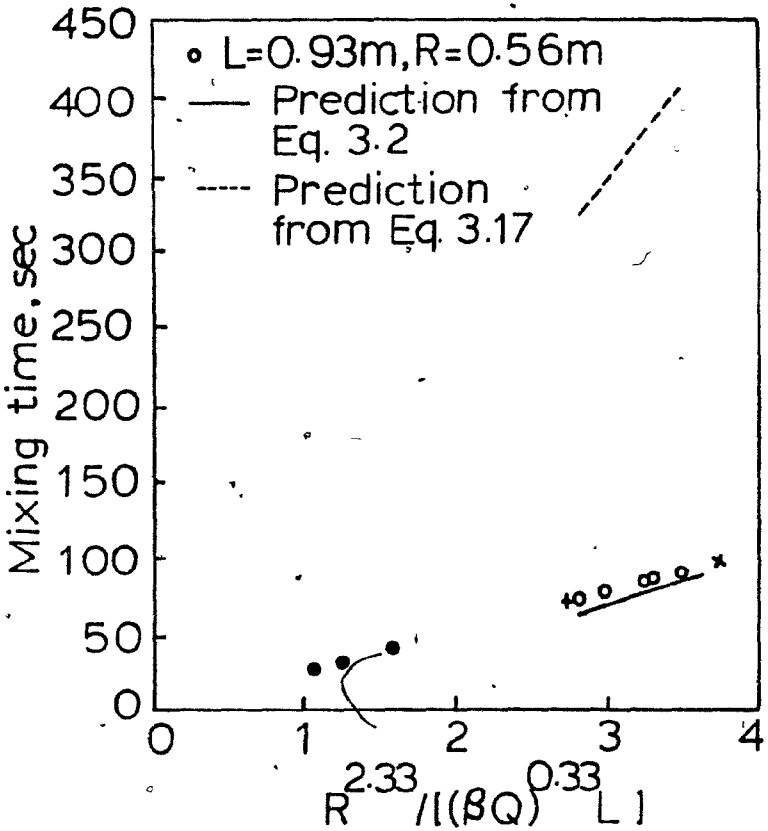

Figure 3.3(a) Mixing times predicted from equation (3.2) and equation (3.17) for the large water model (L = 0.93 m, R = 0.56 m) and their comparison with experimental mixing times.

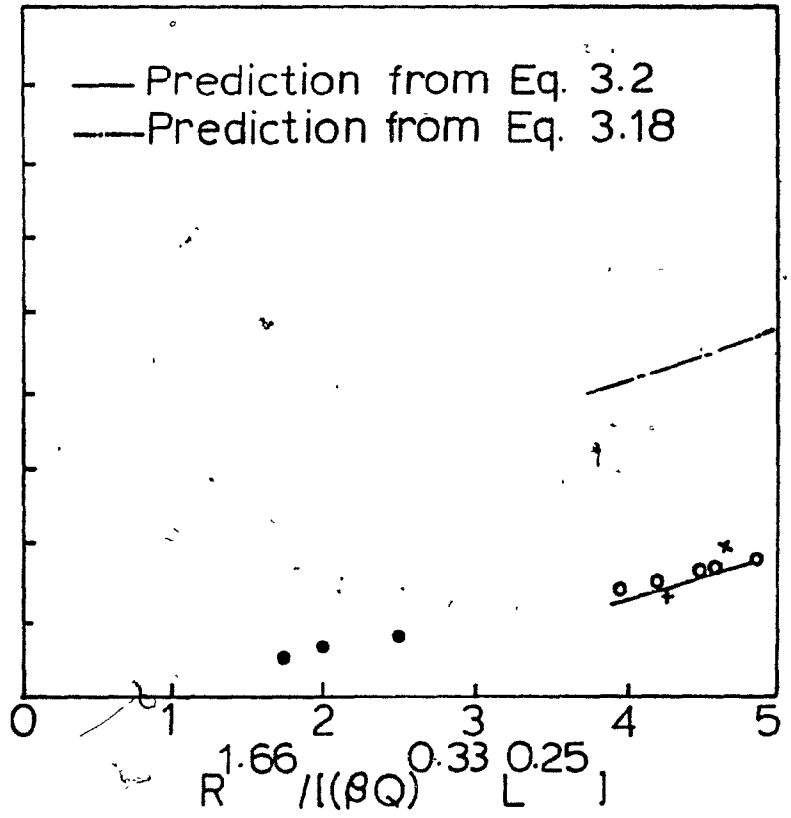

Figure 3.3(b) Mixing times predicted from equation (3.2) and equation (3.18) for the large water model (L = 0.93 m, R = 0.56 m) and their comparison with experimental mixing times.

systems are governed by the combined phenomena of convection and turbulent diffusion.

Experimentally measured mixing times, at a gas flow rate of 6.67×10^{-4} m^3/s (e.g., 40 lits/min) are illustrated in Fig. 3.4, as a function of liquid depth,L. There the relationship appears to be $T_m \propto L^{-0.96}$. One can again note the rather fortuituous similarity between the experimental exponent of L (=0.96) and that suggested by equation (3.16).

Based on their extensive experimental measurements in different sized vessels, Asai et al (2) suggested an empirical correlation $T_m \propto \dot{\varepsilon}_m^{-1/3} L^{-1} R^{4/3}$ for estimating mixing times in such gas injection systems. By manipulating equation (3.16) one can produce the practically equivalent relationship, i.e., $T_m \propto \dot{\varepsilon}_m^{-1/3} L^{-1} R^{5/3}$.

Equation (3.16) can be tuned to describe experimental observations fairly accurately and has a form equivalent to empirical correlation proposed by previous investigators (2), for estimating mixing times in axisymmetric bubble driven system. Consequently, mixing times in cylindrical tanks agitated by a centrally rising bubble plume, can be adequately described via the following <u>empirical</u> correlation

$$T_m = C_2 \frac{R^{7/3}}{(\beta Q)^{1/3} \cdot L} \qquad (3.20)$$

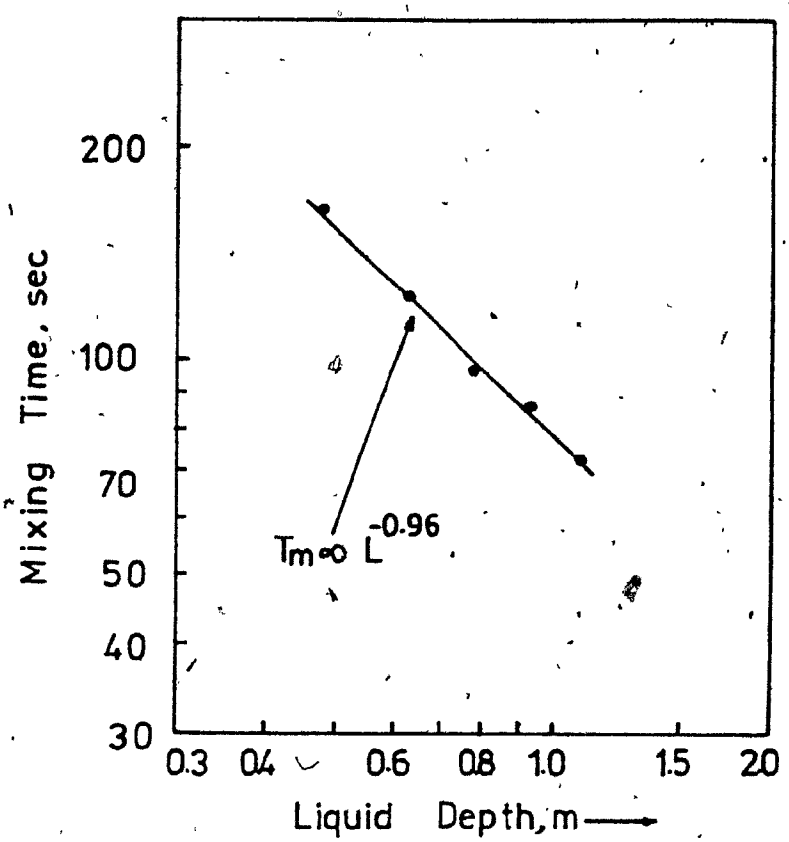

Figure 3.4 Experimentally measured mixing times as a function of liquid depth L ($Q = 6.67 \times 10^{-4}$ m^3/s, $\beta = 0.94$, $R = 0.56$).

or

$$T_m = C_2' \frac{R^{5/3}}{\dot{\varepsilon}_m^{1/3} \cdot L} \qquad (3.21)$$

C_2, the empirical constant in equation (3.20) can now be directly deduced from Fig. 3.2(a) (i.e., $C_2 = T_m$, where, $\frac{R^{7/3}}{(\beta Q)^{1/3} \cdot L} = 1$) and C_2 is found to be 25.4. Consequently, with $C_2 = 25.4$, mixing times in such ladle refining operations can be explicitly represented via the following relationship:

$$T_m = 25.4 \frac{R^{7/3}}{(\beta Q)^{1/3} \cdot L} \qquad (3.22)$$

However, it is instructive to note here that equation (3.22) is applicable only for central gas injection into cylindrical tanks, and only in the high gas flow regime (greater than 30 lits/min of flow in Fig. 3.6). Furthermore, the numerical value of C_2 will generally reflect a degree of bulk mixing only up to 95 pct. mark. Evidently, C_2 would assume a higher value if $(R^{7/3}/|(\beta Q)^{1/3} L)|$ in Fig. 3.2(a) were to be compared against 99.9 pct. (say) mixing times.

In estimating the constant C_2 from Fig. 3.2(a), due care was taken, so that mixing times referred to there represent bulk 95 pct. mixing times. As mentioned previously, the mixing time has been defined as the time taken for the concentration of

tracer at location A (see Fig. 3.5) to fall continuously within 5 pct. of the well mixed values. It is naturally important to justify whether the band width (i.e., 1.0 $\pm$ 0.05) selected is appropriate as a criterion. Fig. 3.5 shows how the normalized concentration ($m_i/m_{i,bulk}$) varies as a function of time for three different regions in the water model ladle. As seen the local rates of mixing in these three regions are quite different, with region A exhibiting the slowest rate of liquid mixing. Consequently, it can be concluded that a measuring probe immersed near region A, is best interpreted as representing the 95 pct. mixing time, rather than 95 pct. mixing times registered at locations B and C.

The effect of gas flow rate on mixing

Experimentally measured mixing times in one of two vessels (L = 0.93 m, R = 0.56 m) as a function of gas flow rate has been illustrated in Fig. 3.6. It is seen that the relationship between T_m and Q is $T_m \propto Q^{-0.48}$ at low gas flow rates followed by a shift to $T_m \propto Q^{-0.34}$ at flows greater than about 5×10^{-4} m^3/s (or 30 lits/min). It is interesting to note that the exponent of Q for the high flow rate regime is practically similar to one suggested by equation (3.16) and (3.17) respectively.

The effect of lance depth on mixing

For central gas injection, experimentally measured mixing times, for various depths of lance submersion, is illustrated in Fig. 3.7. It is at once clear that any increase in the depth

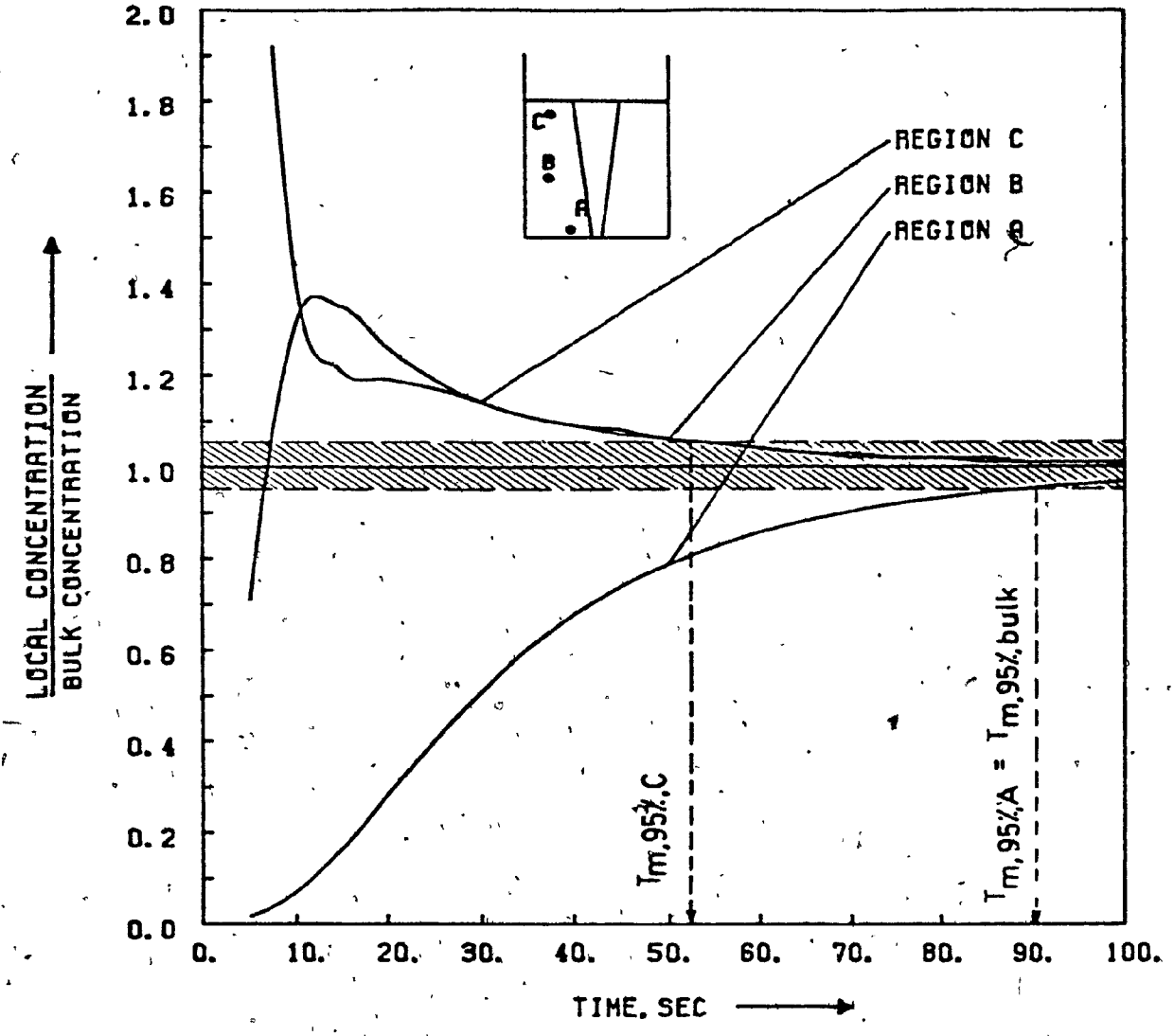

Figure 3.5 Variation in local mixing time for three different regions, A, B and C, in the water model ladle (L = 0.93, R_3 = 0.56 m, β = 0.94 and Q = 6.67 x 10^{-4} m^3/s), showing the criterion for evaluating 95 pct. bulk mixing times for conventional ladle stirring operation.

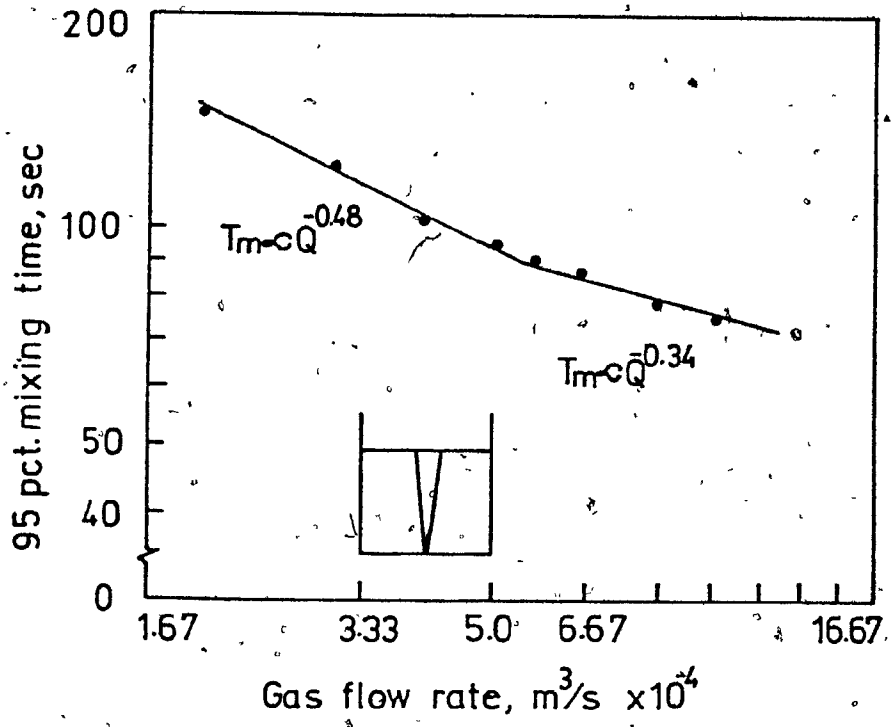

Figure 3.6 Experimentally measured mixing times in the water model ladle (L = 0.93 m, R = 0.56 m) as a function of gas flow rates.

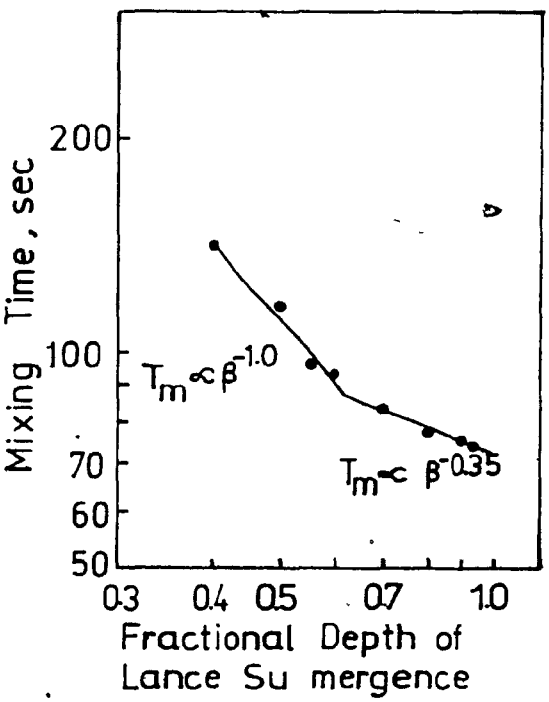

Figure 3.7 Experimentally measured mixing times in the water model ladle (L = 0.93 m, R = 0.56 m), as a function of fractional depth of lance submergence ($Q = 1 \times 10^{-3}$ m^3/s).

of lance submergence enhances mixing considerably. As seen from equations (3.20) and (3.21), the specific input energy rate, $\dot{\epsilon}_m$, is directly proportional to (gas flow rate x lance depth). Consequently the extent of influence of these two parameters on liquid mixing can be readily anticipated. To illustrate this further, Table 3.1 has been included, which shows how the mean speed of liquid recirculation and eddy diffusivity tends to vary with gas flow rate and fractional depth of lance submergence and thus affect the rate of liquid mixing.

B. The C.A.S. Method

Influence of time step size on mathematical model prediction

To compare the predictions from the differential model with experimental measurements, it is necessary that the model predictions be independent of grid distribution. Since a 18 x 15 grid network has already been found to produce practically grid independent results (see Part I), the purpose here is to determine an optimum time step Δt, which will produce results independent of grid configurations in both space and time. The influence of time step upon model performance is illustrated in Fig. 3.8. This shows the variation in dimensionless mass fraction ($m_i/m_{i,\,bulk}$) as a function of time, at a particular location for four different time steps. It is readily seen that reducing the time step below 5 seconds, does not produce any significant change on the nature of model predictions.

Table 3.1 Predicted mean speed of liquid recirculation (m/s) and eddy diffusivity values (m^2/s) as a function of gas flow rate and fractional depth of lance submergence for conventional ladle stirring operations.

Vessel Radius = 0.56 m Liquid Depth = 0.93 m

No	Gas Flow Rate m^3s^{-1}	Fractional Depth of Lance Submergence	Mean Speed of Liquid Recirculation ms^{-1}	Eddy Diffusivity, m^2/s	Mixing times, sec	
					Experimental	Prediction
1	$6.67*10^{-4}$	0.94	0.073	$91.4*10^{-5}$	82	91
2	$8.33*10^{-4}$	0.70	0.0711	$85.8*10^{-5}$	86	97
3	$10.0*10^{-4}$	0.94	0.0807	$103.5*10^{-5}$	71	78

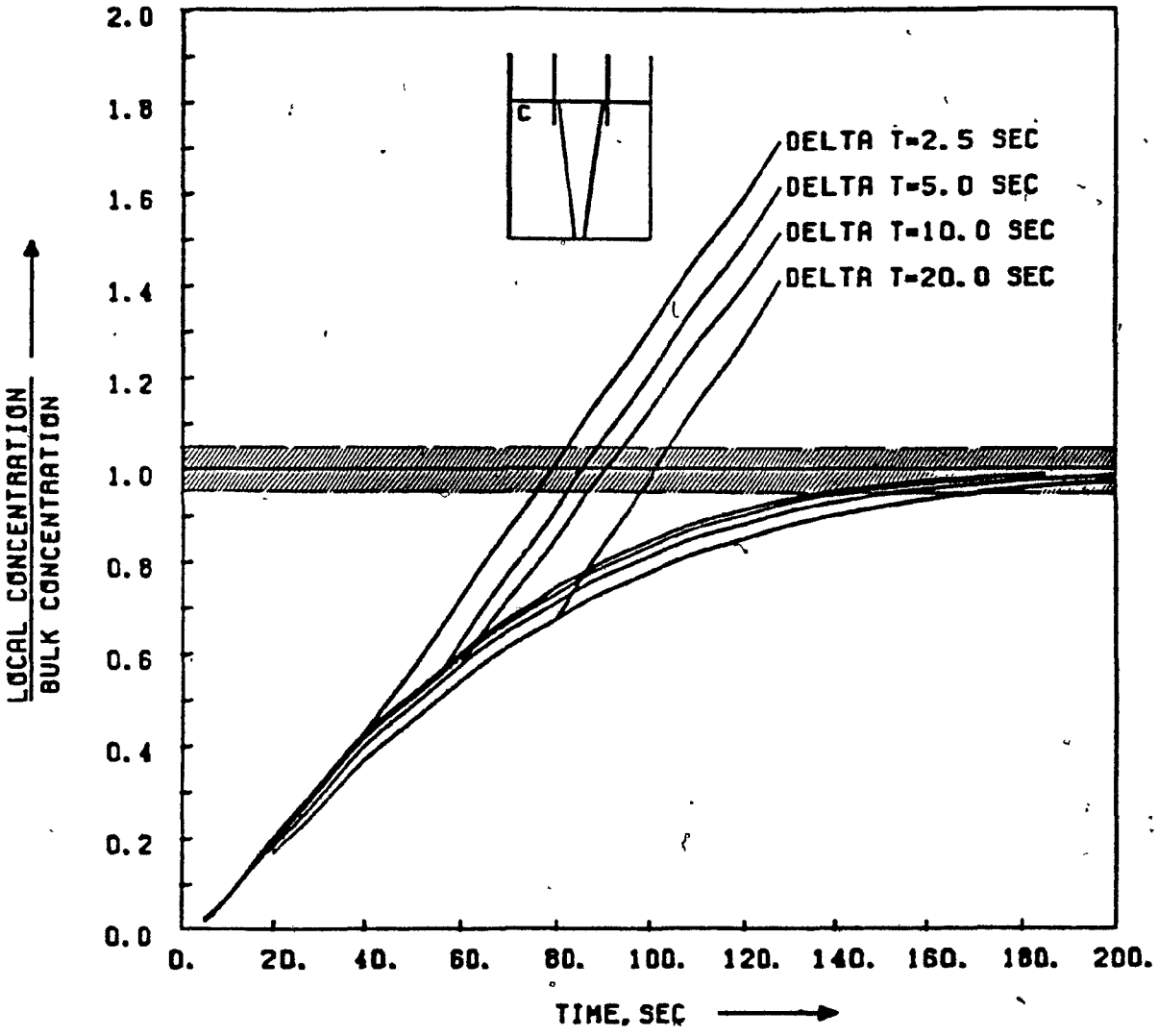

Figure 3.8 Effect of Δt on numerically predicted mixing time curves for an 18 x 15 space grid network, and monitored at location C in Fig. 3.9.

Consequently, Δt = 5 seconds was taken to be an optimum time step, with the 18 x 15 space grid network used, and numerical computations can be expected to be practically grid independent.

Comparison of numerically predicted and experimentally measured mixing times for various operating conditions

Assuming that eddy diffusivity and eddy kinematic viscosity are of identical magnitude, since they both derive from the phenomenon of turbulent fluctuations, 95 pct. mixing times have been predicted, for various operating conditions, and are compared with experimental measurements in Table 3.2. As seen, both 'effective viscosity models' appear to simulate experimental measurements realistically, with the predicted homogenisation time via the modified $k-\varepsilon$ model being somewhat closer to experimental observations. This suggests that $k-\varepsilon$ model can simulate turbulence characteristics within the system somewhat more accurately than the volumetric average effective viscosity formula. This one would normally expect because of the transport type nature of the governing equations in the two equation model.

Criterion for evaluating 95 pct. mixing times

As previously mentioned, the mixing time has been defined as the time taken for the concentration of tracer at location C to fall within 5 pct. of the well mixed value. It is naturally important to justify whether the band width (i.e., 1.0 ± 0.05) selected is appropriate as a criterion. Figure 3.9 shows how

Table 3.2 Comparison of experimental and predicted mixing times for various operating conditions in the 0.30 scale water model during the C.A.S. operations.

Vessel Daimeter = 1.12 m Liquid Depth = 0.93 m

No.	Gas Flow Rate, m^3/s	Fractional Depth of Lance Submergence	Experimental 95 pct. Mixing Time Sec.	Predicted 95 pct. Mixing Time, sec.	
				Bulk Effective Viscosity Formula	k-ε two Equation Turbulence Model
1	6.8×10^{-4}	0.5	250	173	235
2	6.8×10^{-4}	0.7	210	164	195
3	6.8×10^{-4}	0.94	150	120	139

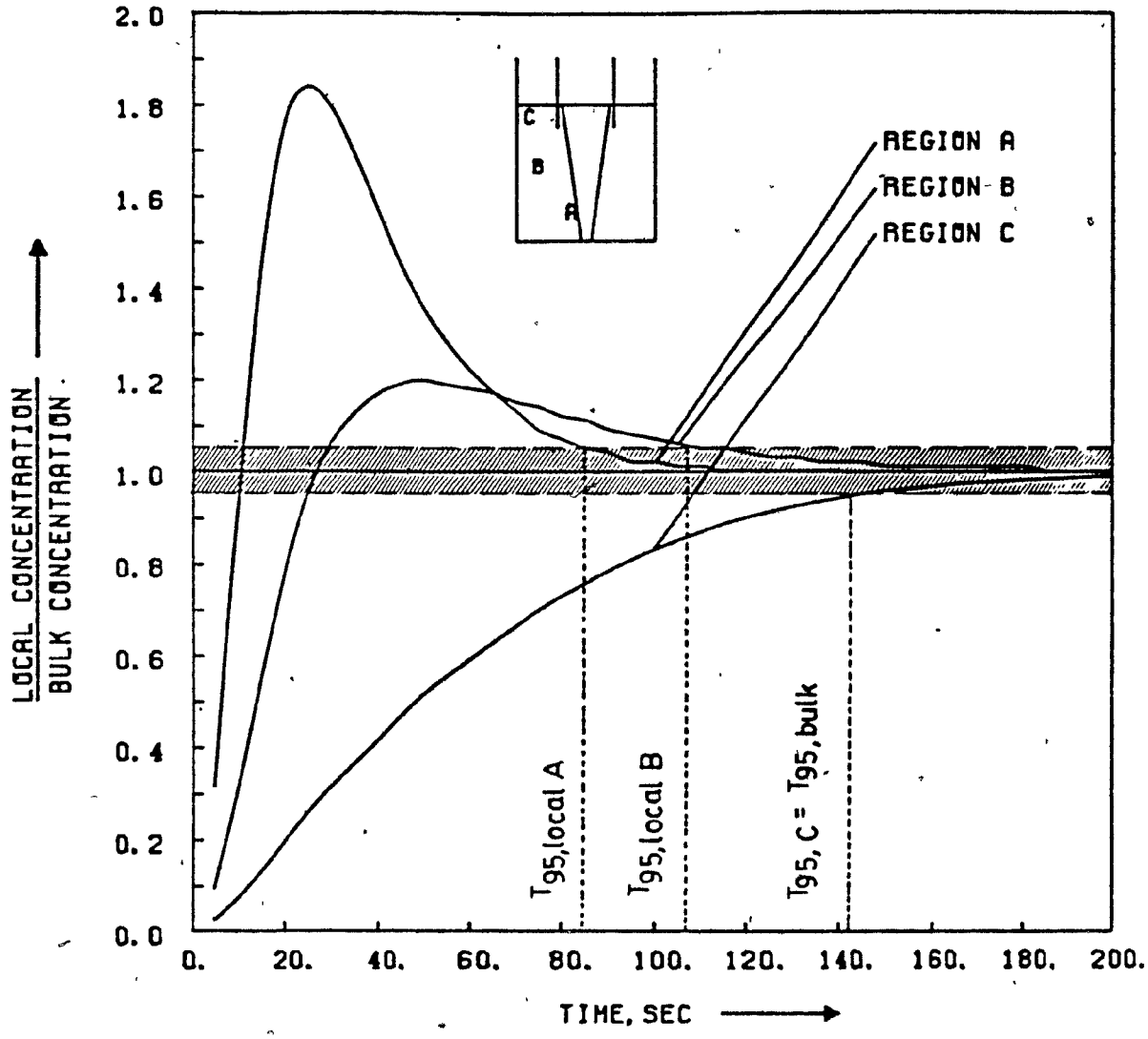

Figure 3.9 Predicted variation of dimensionless mass fraction ($m_i/m_{i,b}$) as a function of time in three different regions of the water model ($Q = 6.80 \times 10^{-4}$ m^3/s, $\beta = 0.94$), showing the criterion for evaluating the 95 pct. bulk mixing time for the C.A.S. procedure.

the normalised concentration ($m_i/m_{i,bulk}$) varies as a function of time for three different regions of the model C.A.S. ladle. As seen, the local rates of mixing in these three regions are quite different, with region C exhibiting the slowest rate of liquid mixing. Consequently, it can be concluded that a measuring probe immersed near region C, is best interpreted as representing the 95 pct. mixing times, rather than the 95 pct. mixing times registered at location A and B (see Fig. 3.9).

Comparison of mixing times between the C.A.S. and conventional central gas injection procedures

Figure 3.10 compares the experimentally measured mixing times for the two different gas stirring operations (viz., conventional central injection and C.A.S.) as a function of gas flow rates. As seen, the rate of liquid mixing in these two systems differ widely, with C.A.S. exhibiting a much poorer rate of addition homogenisation (i.e., about 50 to 60 pct. longer mixing times under the same operating conditions). It is to be mentioned that a similar observation has been made in larger size steel processing ladles at the Gary Works of the U.S. Steel Corporation (8). Of particular interest here is the functional relationship between mixing times and gas flow rates for the C.A.S. system, which has been illustrated on a log-log plot in Fig. 3.11. There it is seen that the relationship between T_m and Q is $T_m \propto Q^{-0.63}$ at low gas flow rates, followed by a shift to $T_m \propto Q^{-0.10}$ at flows greater than about $4 \times 10^4 m^3/s$

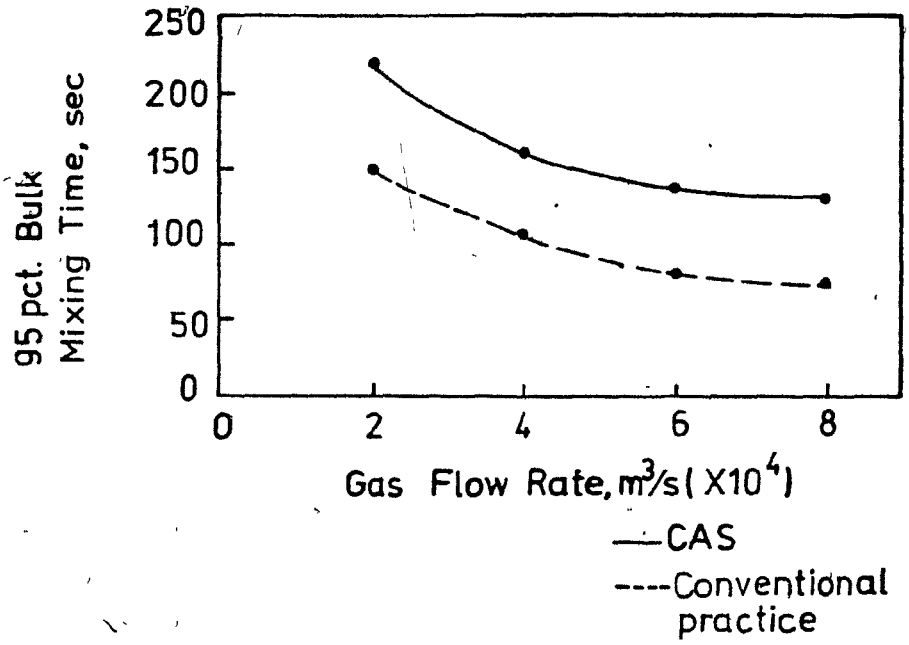

Figure 3.10 Comparison of experimentally measured mixing times as a function of gas flow rates for two gas injection procedures (i.e., conventional central injection and the C.A.S.) in the water model ladle.

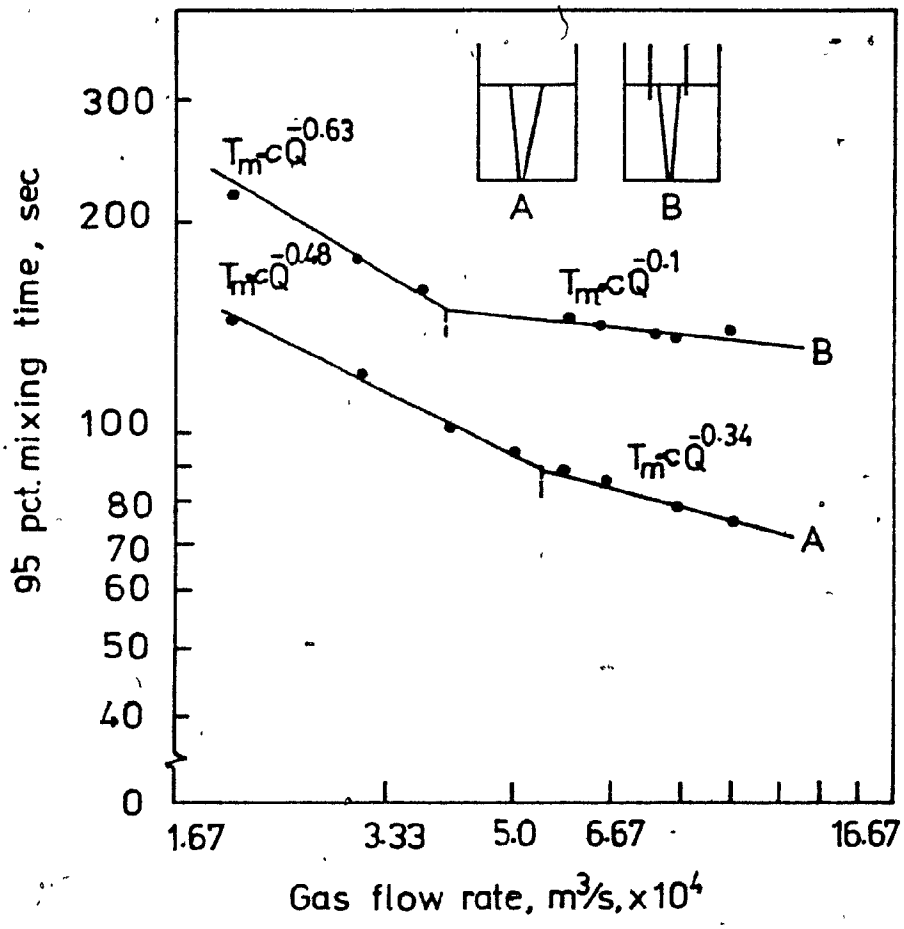

Figure 3.11 Functional relationships between mixing times and gas flow rates on a log-log plot for the two gas injection procedures described in Fig. 3.10.

(or 24 lits/min). It is important to note the index on Q particularly in the high flow rate regime, which is very different from the corresponding experimental exponent of Q (i.e., -0.34) for conventional central injection.

We may now consider the physical phenomena incorporated in the axisymmetric C.A.S. operation. It is evident that placing a cylinder over the eye of the upwelling gas/liquid mixture, may stifle high radial outflows across the free surface and deflect these vertically downwards (Fig. 1.18, Part I). This plunging annular stream of liquid adjacent to the centrally rising gas-liquid plume will tend to increase the rate of turbulence energy dissipation between the plume and adjacent liquid. Evidently, this energy consumption will occur at the expense of energy transfer from the rising plume to the main bulk of recirculating liquid within the ladle. In other words, given the same energy input, and gas flow rate, less of the available energy is utilised in the C.A.S. than that used during normal central injection. This explains why the rate of recirculation of bulk liquid, and rate of liquid mixing were lower in the C.A.S. in comparison to those observed during normal central injection.

In the U.S. Steel operation, argon consumption and processing times are greater as a result (8). Such C.A.S. operations graphically demonstrate that the 'universal relationship' proposed by Nakanishi et al (1) (i.e., $T_m = k\ \dot{\varepsilon}_v^{-0.4}$) is less

universal than recent literature would imply. Obviously vessel shape, baffles, method of energy input, and mode of dissipation, all preclude such generalisation.

Effect of some operating variables on mixing times in the C.A.S. operations

Experimentally measured mixing times for three different depths of lance submersion versus gas flow rate are given in Fig. 3.12. As seen, the depth of lance submergence appears to influence mixing considerably. As previously mentioned, four mixing times were measured for each condition. The variation shown in Fig. 3.12 amounted to not more than 10 pct. (for coincident points, only one point has been marked).

The geometry of the centrally placed cylinder (i.e., its diameter and depth of immersion) over the gas liquid plume can also exert profound effect on the rate of addition dispersion in such a system. As shown in Fig. 3.13, the mixing times appear to increase sharply as the depth of immersion of the central plexiglass cylinder increases. It is important to note that as the depth of immersion increases, more and more of the bulk becomes quiescent and consequently mixing time increases sharply.

C. Industrial Applications

Gas injection into ladles is practised principally to homogenise the bath chemically, to remove particulates, to control temperatures, and to eliminate temperature stratification. A

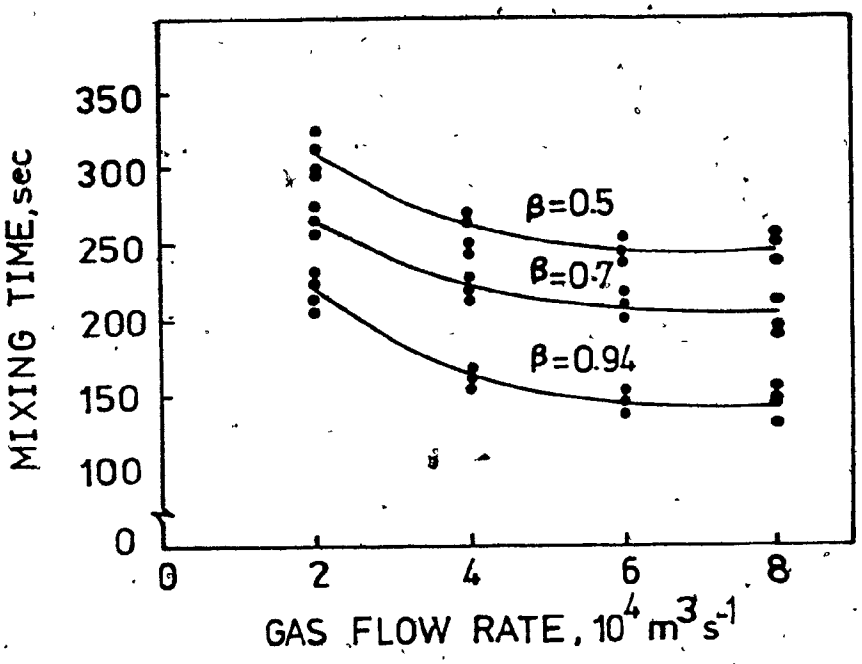

Figure 3.12 Experimentally measured mixing times (sec), as a function of gas flow rate (m^3/s) in the water model for three different depths of lance submergence during the C.A.S. procedure.

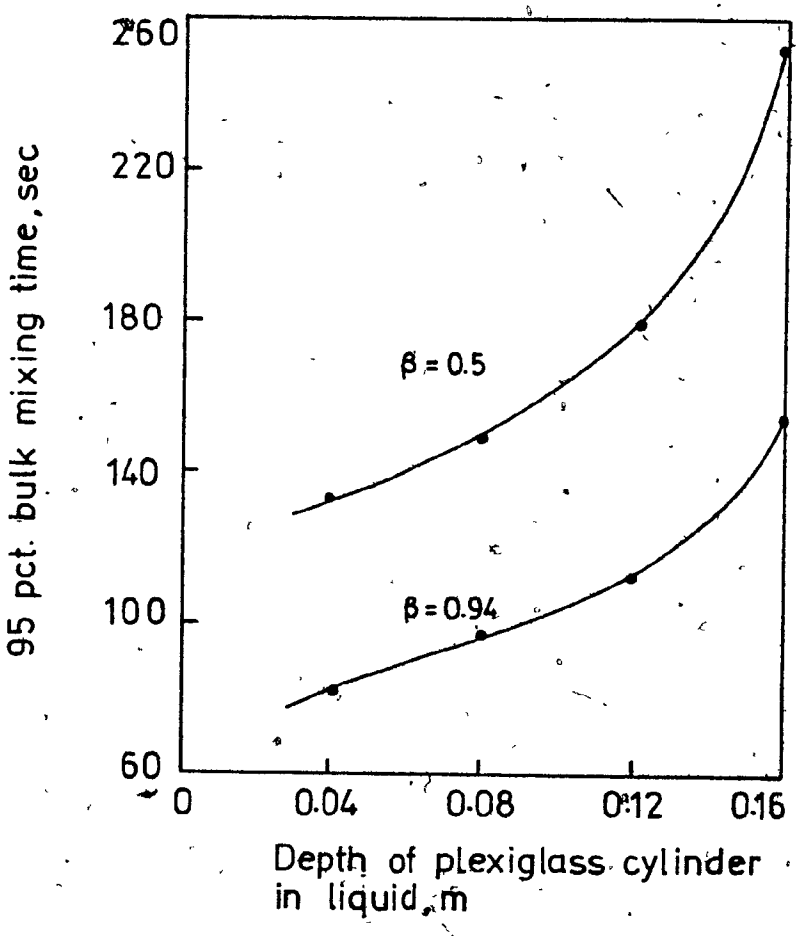

Figure 3.13. Effect of depth of the central plexiglass cylinder on experimentally measured mixing times.

reasonable estimate about homogenisation, or mixing rates, in such industrial operations can be made either,

(i) from direct measurements taken under some typical operating conditions and/or,

(ii) from a theoretical approach of the type outlined in the previous section.

However, high temperatures (e.g., 1600°C) and the visual opacity of liquid metals make such processing units less than convenient case studies. On the other hand numerical modelling, though very promising, involves a certain degree of computational effort and consequently cannot be justified for each individual problem.

Thus, to test the applicability of equation (3.22) to larger size steel processing units, mixing times in a 60 t ladle have been predicted for three different blowing rates. Furthermore, subsequent predictions were made from the more detailed differential model (viz., equation (3.2)). The comparison between the predictions has been illustrated in Table 3.3. Very reasonable agreement between the two are readily apparent.

The applicability of equation (3.22), on the basis of the comparison illustrated in Table 3.3, to industrial size vessels, further enables one to relate the mixing times in the model ladle to those in the full scale system, through the geometrical scaling factor λ, according to

$$T_{m,mod} = T_{m'f.s} * \lambda^{4/3} \qquad (3.23)$$

Table 3.3 Comparison of 95 pct. bulk mixing times predicted from the differential model and equation (3.22) for an industrial size 60 ton ladle

Vessel Radius = 1.225 m Liquid Depth = 1.50 m

No	Gas Flow Rate, $m^3 s^{-1}$	Fractional Depth of Lance Submergence	Predicted 95 pct. Mixing Times, Sec	
			Differential Model, [Equation 3.2]	Equation (3.22)
1	$3.82*10^{-3}$	∿1.0	156	172
2	$7.96*10^{-3}$	∿1.0	111	136
3	$10.62*10^{-3}$	∿1.0	104	119

As a final note, it is to be emphasized that the flow fields in the full scale ladle and the water model are very similar. One can therefore expect that the mechanism of dispersion and mixing of alloy additions will be practically identical. Mixing in a 150 ton ladle during C.A.S. operation at a gas flow rate of 0.0188 m^3 s^{-1}, which is shown in Fig. 3.14 exhibit close similarity with the observations made in the water model study. At this gas flow rate, about 400 seconds blowing is needed to disperse the additions homogeneously in the bath. Also, on the basis of numerical solution of equation (3.2), predictions were made for mixing times in C.A.S. and conventional gas stirring operation in a 150 ton ladle at a blowing rate of 0.0188 m^3/s. Predicted mixing times are approximately 155 seconds and 280 seconds respectively. Of particular importance is however the rates of mixing in the vicinity of the free surface. As shown in Fig. 3.15 the rates of mixing near the free surface are considerably different. This essentially arises because of the surface baffle in the C.A.S.. This sluggish rate of liquid mixing near the free surface in the C.A.S. operation can lead to a minimal transfer of dissolved additions between metal and slag phase, which can help in slowing fading and improving recovery rates of alloy additions such as aluminum.

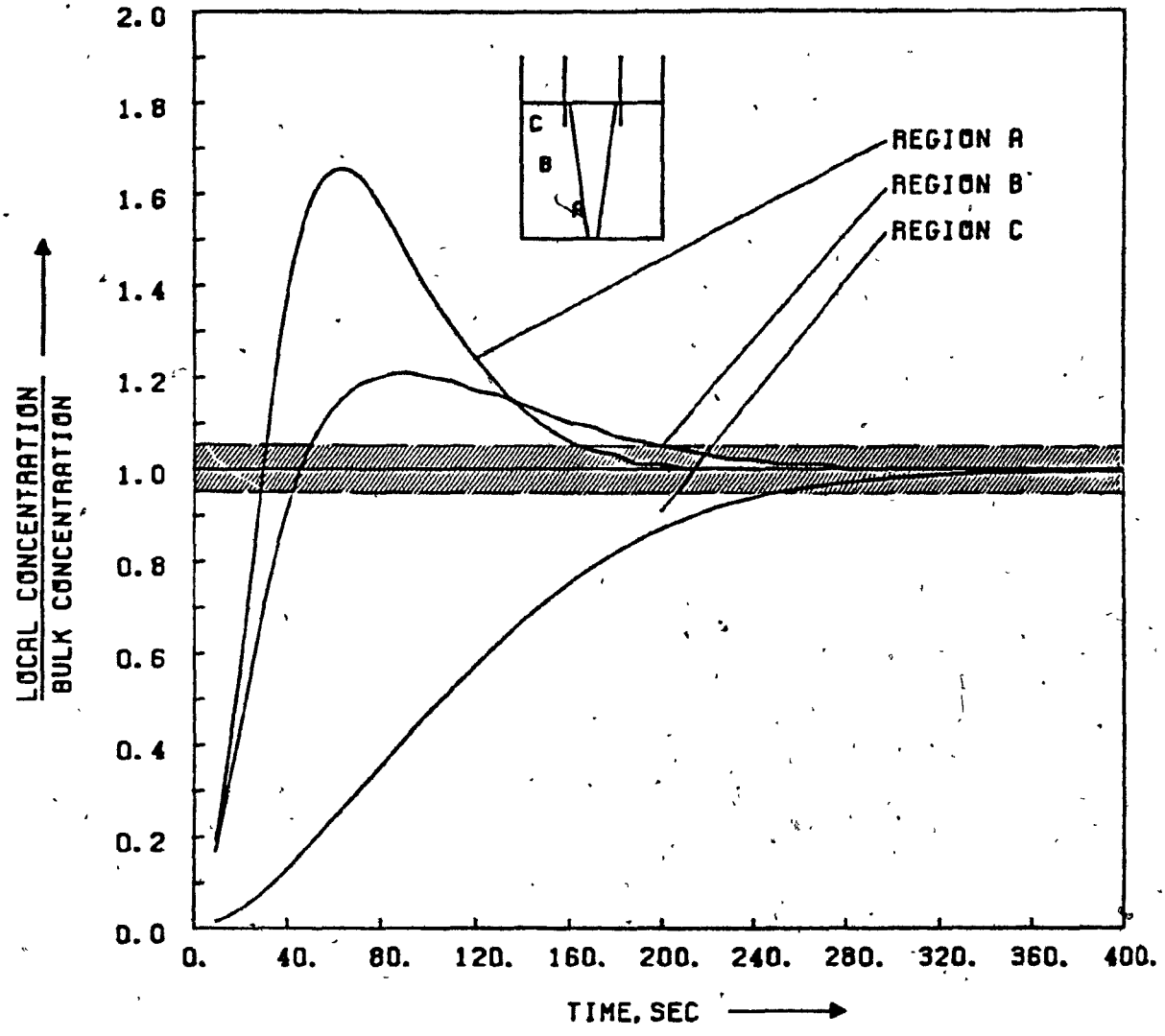

Figure 3.14 Predicted distribution of dimensionless mass fraction ($m_i/m_{i,b}$) as a function of time in three different regions in a 150 ton cylindrical ladle ($Q = 0.0188\ m^3/s$, $\beta = 0.94$), during C.A.S. alloy addition procedure.

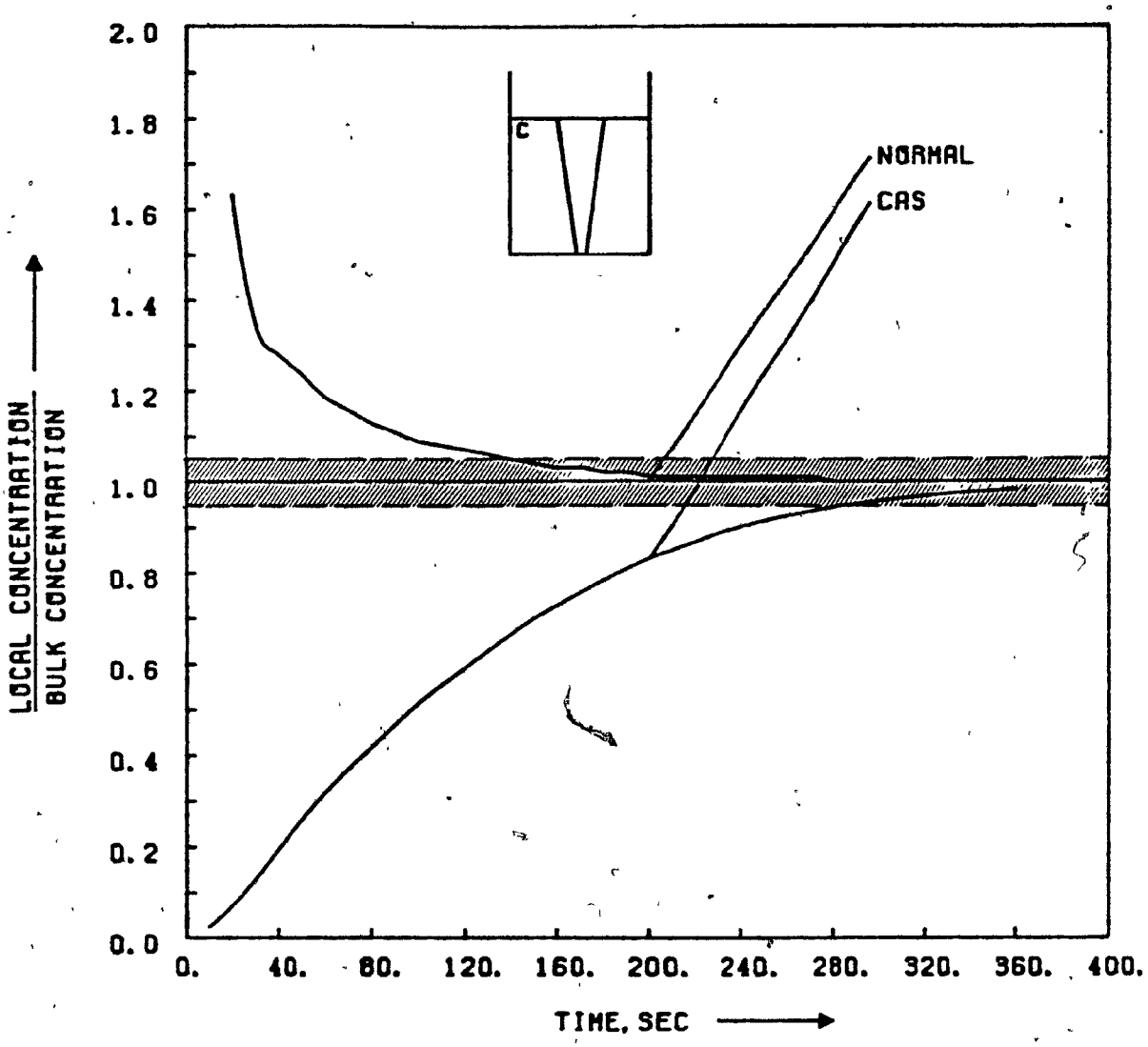

Figure 3.15 Predicted mixing rates in the vicinity of the free surface in a 150 ton industrial ladle at a blowing rate of 0.0188 m^3/s for the two gas injection procedures (i.e., conventional gas injection and C.A.S.).

CONCLUSIONS

Liquid mixing in gas stirred metallurgical melts has been investigated from a theoretical as well as experimental view point. It has been demonstrated that addition dispersion in such gas injection operations is expected to be controlled by a combined mechanism of eddy diffusion and bulk convection. Empirical correlations for estimating mixing times during central injection into cylindrical vessels have been proposed.

Liquid mixing behaviour in the C.A.S. process has been compared with conventional gas injection process. Mixing behaviour in industrial scale vessels have been predicted on the basis of these results, and their technological significance discussed.

Finally, quantitative relationships were developed for estimating alloy dispersion times in industrial C.A.S. operations.

LIST OF SYMBOLS

C_1, C_2	Constants defined by equations (3.15) and (3.16) respectively
D_e	Eddy diffusivity, $m^2 s^{-1}$
g	Acceleration due to gravity, $m\ s^{-2}$
K	Dimensional constant in equation (3.9); has a value 4.19
L	Liquid depth, m
L_c	A characteristic length, m
L_m	Characteristic length of the model, m
$L_{f.s}$	Characteristic length of the full scale system, m
m_i	Mass fraction of species i
m_i^o	A given mass fraction of species i
Q	Gas flowrate, $m^3\ s^{-1}$
R	Vessel radius, m
r	Radial coordinate, m
t	Time, sec
T_m	Mixing time, sec
$T_{m,mod}$	Mixing time in model, sec
$T_{m,f.s}$	Mixing time in full scale system, sec
u	The axial velocity component, $m\ s^{-1}$
U_P	Average plume velocity, $m\ s^{-1}$
$\bar{U}$	Mean speed of liquid recirculation, $m\ s^{-1}$
U	Velocity, $m\ s^{-1}$
v	The radial velocity component, $m\ s^{-1}$
z	Axial coordinate, m

α	Volume fraction of gas in the plume
β	Fractional depth of lance submergence
Γ	Effective exchange coefficient, kg m^{-1} s^{-1}
ρ	Density, kg m^{-3}
λ	Geometric scaling factor (= $L_m/L_{f.s}$)
$\dot{\varepsilon}_v$	Input energy density rate, Watt m^{-3}
$\dot{\varepsilon}_m$	Specific input energy rate, Watt kg^{-1}
μ_e, μ_{eff}	Effective viscosity, kg m^{-1} s^{-1}
ν_t	Turbulent kinematic viscosity, m^2 s^{-1}

REFERENCES

1. K. Nakanishi, T. Fujii and J. Szekely: Ironmaking and Steelmaking, 1975, No. 3, pp. 193-197.

2. S. Asai, T. Okamoto, J.C. He and I. Muchi: Trans. I.S.I.J., 1983, vol. 23, pp. 43-50.

3. J. Szekely, T. Lehner and C.W. Wang: Ironmaking and Steelmaking, 1979, vol. 3, pp. 285-293.

4. Y. Sahai and R.I.L. Guthrie: Metall. Trans. B, 1982, vol. 13, pp. 125-127.

5. B.E. Launder and D.B. Spalding: Computer Methods in Applied Mechanics and Engineering, 1974, vol. 3, pp. 269-289.

6. Y. Sahai and R.I.L. Guthrie: Metal. Trans. B, 1982, vol. 13, pp. 203-211.

7. D.B. Spalding: International Journal of Numerical Methods in Engineering, 1972, vol. 4, pp. 551-559.

8. C.L. Trout, D.L. Paterson and S.M. Hughes: A.I.S.E. Conference Proceeding, Pittsburg, Pennsylvania, 1983.

LIST OF FIGURES

Figure 3.9 Predicted variation of dimensionless mass fraction ($m_i/m_{i,b}$) as a function of time in three different regions of the water model ($Q = 6.80 \times 10^{-4}$ m^3/s, $\beta = 0.94$), showing the criterion for evaluating the 95 pct. bulk mixing time for the C.A.S. procedure.

Figure 3.10 Comparison of experimentally measured mixing times as a function of gas flow rates for two gas injection procedures (i.e., conventional central injection and the C.A.S.) in the water model ladle.

Figure 3.11 Functional relationships between mixing times and gas flow rates on a log-log plot for the two gas injection procedures described in Fig. 3.10.

Figure 3.12 Experimentally measured mixing times (sec), as a function of gas flow rate (m^3/s) in the water model for three different depths of lance submergence during the C.A.S. procedure.

Figure 3.13 Effect of depth of the central plexiglass cylinder on experimentally measured mixing times.

Figure 3.14 Predicted distribution of dimensionless mass fraction ($m_i/m_{i,b}$) as a function of time in three different regions in a 150 ton cylindrical ladle ($Q = 0.0188$ m^3/s, $\beta = 0.94$), during C.A.S. alloy addition procedure.

Figure 3.15 Predicted mixing rates in the vicinity of the free surface in a 150 ton industrial ladle at a blowing rate of 0.0188 m^3/s for the two gas injection procedures (i.e., conventional gas injection and C.A.S.).

LIST OF TABLES

CONCLUSIONS TO THE THESIS

GENERAL CONCLUSIONS

PART I

From the experimental and theoretical studies reported in Part I the following conclusions can be drawn:

(i) The sensitivity of the computation to the choice of grid size and the choice of an average effective viscosity instead of the detailed k - ε model has been verified. It was found that a relative coarse grid and average viscosity would provide a satisfactory answer to the problem of predicting flow fields.

(ii) Bulk flow fields (except in the immediate vicinity of a solid wall) were found to be insensitive to the choice of an effective viscosity model, illustrating that gas stirred systems tend to be dominated by inertial rather than turbulent viscous forces.

(iii) It is also shown that bulk velocity profiles are relatively insensitive to the details of the bubble plume structure.

(iv) Finally, the model is used to predict the effect of a cylinder at the free surface of the ladle, the effect of tapered walls, and extrapolation to large scale ladles.

(v) It has been shown that the placement of a baffle over rising plumes for slag free addition making, causes a strong narrow recirculatory vortex, with a complementary contra-rotating vortex in the main bulk of the liquid.

(vi) Computations based on the standard k - ε two equation turbulence model produced incorrect flow fields for C.A.S. operation. Ad hoc adjustments to two of the five empirical constants were made and realistic flow fields could then be achieved.

(vii) In spite of a number of simplifying assumptions in formulating the problem, it has been demonstrated explicitly that the distribution of flow and turbulence parameters in such systems can now be predicted with reasonable accuracies, and hence full scale predictions can be made with some confidence.

PART II

From the experimental as well as mathematical model studies reported in Part II, the following general conclusions can be drawn:

(i) A gas liquid dispersion can evidently cause some reduction in steady translational drag forces on submerged spheres. Consequently, when additions in gas stirred ladles are introduced over the eye of the bubble plume, they are expected to experience a reduced drag force, than that anticipated for an equivalent homogeneous flow system.

(ii) Buoyant additions (sp. gr = 0.4 & 0.60) will hardly penetrate inside such a bath. On the other hand, neutrally buoyant spheres can undergo prolonged subsurface motion. Denser spherical particles (sp. gr = 1.14) will always settle to the ladle bottom.

(iii) Consequently, additions like aluminium and ferrosilicon will not undergo subsurface melting, whereas ferromanganese has the greatest opportunity to undergo subsurface melting. Denser additions such as ferroniobium will always settle towards the bottom, as they gradually melt or dissolve. Because of a quiescent bath, the melting/dissolution times of dense additions that have settled out can be significantly extended, and mixing considerably delayed.

(iv) Since buoyant additions such as aluminium, ferrosilicon etc. will always float up prior to any melting, it has

been demonstrated that an alloy addition procedure such as the C.A.S. will be an effective way of introducing such buoyant additions from the view point of better recovery and better process control provided control of the atmosphere above the free surface is maintained (i.e., air must be excluded).

PART III

The following general conclusions on the behaviour of liquid mixing in gas stirred ladles can be drawn from Part III:

(i) Mixing cannot be characterised in terms of either bulk convection or eddy diffusion controlled phenomena. Mixing in gas agitated ladles occurs by a combination of these two transport mechanisms.

(ii) Mixing in conventional ladle stirring operations can be adequately described via an empirical model $T_m \propto \dot{\varepsilon}_m^{-1/3} L^{-1} R^{5/3}$. It has been shown that this simple model produces results which are consistent with a more advanced differential model.

(iii) Liquid mixing in the C.A.S. is sluggish and relatively insensitive to gas flow rates. It has been shown that the free surface of liquid in such systems can be expected to be essentially quiescent.

(iv) For an equivalent gas flow rate, mixing in C.A.S. procedure is about 60 pct. slower than in conventional ladle stirring operations.

(v) Because of the quiescent nature of the free surface, the rate of slag-metal reaction in such systems is expected to be slow. Furthermore, because of the presence of the refractory cylinder over the plume, dissolved additions will be dispersed homogeneously into the bulk steel bath prior to reacting with the slag. This will in turn improve the recovery rates of buoyant additions.

CLAIM TO ORIGINALITY

Practically all aspects of this thesis constitute, in the author's opinion, new and distinct contributions to knowledge. The major contributions are:

(i) This is the first detailed hydrodynamic investigation of the C.A.S. method of alloy addition.

(ii) For the first time, the dynamics of two gas injection processes have been compared directly on the basis of hydrodynamics, particle motion and liquid mixing and corresponding process efficiencies explained.

(iii) Much new experimental data in a much larger pilot scale unit than that used by Sahai (ref. 14 Part I) has been carried out using both partly, and wholly, submerged lances.

(iv) The data obtained were used to validate several novel mathematical models developed during the course of this research.

(v) The work contains the first report in the literature that bubbly Newtonian liquids can lead to a reduction in standard drag coefficients on submerged objects.